High Precision X-Ray Spectroscopy of Highly Charged Heavy Ions

Dissertation

zur Erlangung des akademischen Grades
doctor rerum naturalium (Dr. rer. nat.)

vorgelegt dem Rat der Physikalisch-Astronomischen Fakultät
der Friedrich-Schiller-Universität Jena

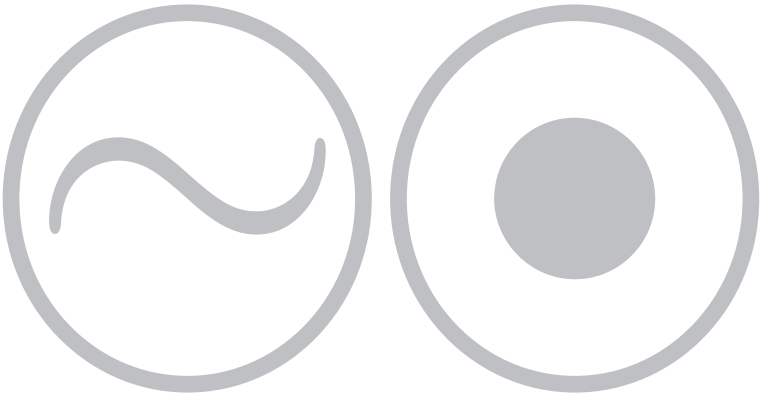

von Dipl.-Phys. **Tobias Gaßner**
geboren am 14. Mai 1986 in Bruchsal

Gutachter:

1. Prof. Dr. Thomas Stöhlker
2. PD Dr. Wolfgang Quint
3. Prof. Dr. Stefan Schippers

Tag der Disputation: 13. Dezember 2016

Abstract

In the present thesis, the advantages of two new and complementary detector concepts for x-ray spectroscopy of highly charged ions over conventional semiconductor detectors have been worked out. These two detectors are the twin crystal spectrometer FOCAL and the metallic magnetic microcalorimeter maXs. Although the maXs microcalorimeter is still under development, first very promising x-ray spectra could be recorded at the ESR storage ring at the GSI Helmholtz Centre for Heavy Ion Research in Darmstadt. With the crystal spectrometer FOCAL, which was fully equipped for the first time, a dedicated beam time at the ESR, aiming for the precise determination of the 1 s Lamb shift of hydrogen-like gold (Au^{78+}), could be conducted. The obtained result for the Lyman-α_1 transition energy is afflicted with a small statistical uncertainty, however, the encountered systematic effects are still posing a challenge to overcome. In the outlook, it will be discussed in detail how the accuracy of a future measurement could be improved, and in which way both detector concepts could support each other optimally.

In der vorliegenden Arbeit werden die Vorteile zweier neuer, sich ergänzende, Detektortypen zur röntgenspektroskopischen Untersuchung von hochgeladenen Schwerionen gegenüber konventionellen Halbleiterdetektoren diskutiert. Bei den Detektoren handelt es sich zum einen um das Zwillings-Kristallspektrometer FOCAL und zum anderen um das metallisch-magnetische Mikrokalorimeter maXs. Obwohl sich das maXs Mikrokalorimeter gegenwärtig noch in der Entwicklung befindet, konnten bereits sehr vielversprechende Röntgenspektren am ESR Speicherring des GSI Helmholtzzentrum für Schwerionenforschung in Darmstadt aufgenommen werden. Weiterhin konnte mit dem erstmals voll ausgebauten Kristallspektrometer FOCAL eine Produktionsstrahlzeit, ebenfalls am ESR, durchgeführt werden, die als Zielsetzung die präzise Bestimmung der 1 s Lamb Verschiebung in wasserstoffähnlichem Gold (Au^{78+}) hatte. Für die Lyman-α_1 Übergangsenergie konnte ein Ergebnis mit kleiner statistischen Unsicherheit erreicht werden, allerdings stellen die während der Analyse untersuchten systematischen Effekte eine noch zu überwindende Herausforderung dar. Im Ausblick wird detailliert dargelegt, wie sich die Genauigkeit in zukünftigen Messungen erhöhen lässt und wie sich die beiden Detektorkonzepte dabei optimal ergänzen können.

Contents

Chapter 1

Introduction

> “The hydrogen atom [is] the simplest and most deeply explored object in the whole universe. If you don’t understand the hydrogen atom you don’t understand anything.”
>
> Freeman Dyson

From the beginning of modern physics, ambitious experiments were conducted to test the most advanced theories available at that time. Often, small discrepancies between prediction and observation led to a literal *quantum leap* in the understanding of nature. One famous example is the fine-structure splitting in the optical spectra of atoms, which could theoretically first be explained by the Dirac equation, to the utmost satisfaction. In the years following the publication of Dirac, experiments confirmed the calculations with greatest precision, until P. Kusch and H.M. Foley published their finding for the anomalous magnetic moment of the electron [Kusc47, Fole48], which deviated slightly from the predictions of Dirac. Almost at the same time, W.E. Lamb and R.C. Retherford [Lamb47] discovered a discrepancy for the energy levels in the hydrogen atom, which was from then on known as the *Lamb shift*. It is this vivid period of time to which Freeman Dyson’s above quote refers. The findings of Lamb and Retherford triggered a theoretical research campaign, which resulted in the development of quantum electrodynamics (QED) at the end of the 1940s [Dyso49].

In the past 65 years, numerous experiments, aiming for a precise test of QED, have been performed [Kars05], which are basically all in good agreement with theory. Due to this reason, the confidence in quantum electrodynamics became so strong, that it is even used to determine the numerical values of natural constants, such as the fine structure constant α [Hann08], or the electron rest mass m_e [Stur14].

The only way to test QED with hitherto unprecedented precision is to use more elaborate detection techniques, and to test its validity under more extreme conditions. With the advent of powerful particle accelerators it became possible to produce reasonable amounts of heavy hydrogen-like ions, which are ions with only one remaining bound electron. This electron experiences very strong electric fields, which cannot be created by other methods, and are close to the Schwinger limit where spontaneous electron-positron pair creation becomes possible. Measuring the Lamb shift in these systems by means of spectroscopic methods is an ultimate test of QED. Unfortunately, at the moment, even the most accurate experiments are one order of magnitude less precise than the best calculations available [Yero15]. This is mainly due to the limited detector resolution and uncertainties introduced by systematic effects.

In this thesis, two complementary detector types, employing either the wave-like or the particle-like aspect of photons, will be presented, which both have the potential to surpass the restrictions of conventional detectors, which are currently in use for high precision measurements on stored, highly-charged heavy ions.

- ∿ The wave-like aspect of the photon is utilised by the crystal spectrometer FOCAL, measuring the *wavelength* of the characteristic transitions with high precision. In the dedicated Doppler-effect cancelling layout it is best suited for measurements at gas-jet targets at storage rings.

- ⊙ The particle-like aspect of the photon is utilised by the microcalorimeter maXs, measuring the *energy* of the x-ray photons with highest precision. It complements the measurements of FOCAL if installed at the electron cooler of storage rings.

In combination with the low-energy storage ring CRYRING, these two detector concepts will be able to boost the experimental precision by large factors, allowing more stringent tests of quantum electrodynamics in the strong-field regime than ever before.

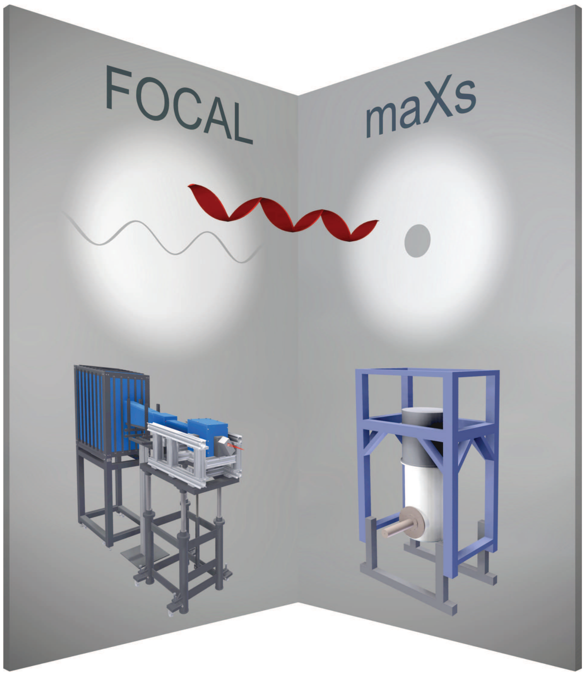

Figure 1.1: One and the same physical object (red) shows different characteristics if investigated with the crystal spectrometer FOCAL (left) or the microcalorimeter maXs (right).

Chapter 2

Physics Motivation and Methodical Foundations

This chapter is divided into four parts. The first part gives a short introduction to the physics of hydrogen-like ions. Besides the relativistic treatment of these fundamental systems, the most prominent contribution of quantum electrodynamics will be discussed. In the second part, the diffraction of x rays in crystals is covered, which is important for the understanding of the principle of a crystal spectrometer like FOCAL. This section is followed by the technique utilised by the metallic magnetic calorimeter maXs. The chapter closes with a short overview of the various experimental methods used so far for the investigation of the atomic structure of highly charged heavy ions.

2.1 The Lamb Shift in Hydrogen-Like Ions

While in the beginning of quantum mechanics the non-relativistic Schrödinger equation was sufficient to describe the spectrum of the hydrogen atom, being consistent with the findings of early spectroscopic investigations, modern calculations include a long list of new contributions, which must be verified by state-of-the-art experiments. Besides the inclusion of relativity, an important contribution of Dirac, other effects described in the framework of quantum electrodynamics also strongly influence the level energies. A further class of corrections is associated with the size and structure of the atomic nucleus, which should not be treated as a point-like object in high precision calculations.

2.1.1 Non-Relativistic Theory

In 1888 Johannes Rydberg presented his famous formula to describe the light emission spectrum of atomic hydrogen

$$\frac{1}{\lambda} = R\left(Z^2\right)\left(\frac{1}{n_1^2} - \frac{1}{n_2^2}\right) \tag{2.1}$$

with λ being the vacuum wavelength of the transition between the two involved states $n_{1,2}$. This completely phenomenological expression was the first equation which made use of *quantised* integer numbers $n_{1,2}$ to describe a physical process, and thus heralding the era of quantum mechanics. Already here, it is interesting to note that the element-dependent Rydberg constant R, which is given by $R = R_\infty / \left(1 + \frac{m_e}{M}\right)$, with the electron mass m_e, the nuclear mass M and the Rydberg constant for infinite heavy nuclei R_∞, takes care of the recoil of the atomic nucleus which will be discussed in detail in section 2.1.4. The quadratic scaling with the nuclear charge Z had been introduced later to obtain valid results for heavier, hydrogen-like (in short, H-like) ions, such as He^{+}, Li^{2+} or, as in the present work, Au^{78+}.

It was perhaps his biggest success when Erwin Schrödinger formulated his equation 2.2 in 1926 [Schr26], being able to reproduce the Rydberg formula, and to put it on the well-grounded foundation of the new mechanics. The equation for a hydrogen-like system is given by

$$-\frac{\hbar^2}{2\,m}\nabla^2\psi + V(\mathbf{r})\,\psi = E_n\,\psi \tag{2.2}$$

with energy levels E_n, the wave function ψ and the (reduced) Planck constant $\hbar$. However, it would be more accurate to mention that this is the equation for a charged quasi-particle with mass m, moving in an external, static Coulomb field $V(\mathbf{r})$. The mass of the quasi-particle is given by the reduced mass of the nucleus-electron system $m = m_e / \left(1 + \frac{m_e}{M}\right)$, which is similar to the expression for the Rydberg constant. The solution for the energy eigenvalues of the Schrödinger equation is given by

$$E_n = -R_y^*\,\frac{Z^2}{n^2} \tag{2.3}$$

which is equivalent to formula 2.1 if energy differences $1/\lambda = \Delta E/hc = (E_2 - E_1)/hc$ and the definition of the Rydberg energy $R_y^* = R\,h\,c$, with the speed of light c, is used. According to solution 2.3 every state with the same principal quantum number n should have the exact same energy, independent of other, possibly existing, internal degrees of freedom. Also in 1926, Uhlenbeck and Goudsmit [Uhle26] postulated the existence of the electron spin, leading to the fine-structure splitting in the spectra of atoms, which had to be introduced into the Schrödinger equation artificially, by additional terms. Another flaw of the Schrödinger equation was the non-relativistic treatment of the wave functions. This can be illustrated when assigning to the electron in the $1\,s$ state a velocity

$$\langle v_{1s}\rangle = Z\,\alpha\,c \tag{2.4}$$

with the fine structure constant $\alpha \approx 1/137$. If the nuclear charge is around $Z = 79$, the velocity of the electron is about 60 % of the speed of light, which is clearly in the relativistic regime. These two shortcomings paved the way for the relativistic Dirac equation, which also includes the spin of the electron in a natural way.

2.1.2 Relativistic Theory

Paul Dirac published his relativistic quantum equation for the electron two years after Schrödinger [Dira28]. For the hydrogen(-like) system it is given in cgs units by

$$\Big(-e\,\varphi(\mathbf{r}) + \beta\,mc^2 + \boldsymbol{\alpha}\cdot(c\,\mathbf{p} + e\,\mathbf{A}(\mathbf{r}))\Big)\,\psi = E\,\psi \tag{2.5}$$

with β ($\boldsymbol{\alpha}$) for the Dirac matrix (vector), φ ($\mathbf{A}$) for the external (vector) potential generated by the nucleus, and $\mathbf{p}$ for the momentum operator [Beth77]. This equation can be solved analytically, with the solution

$$E_{nj} = \frac{mc^2}{\sqrt{1 + \frac{(\alpha Z)^2}{\left[n-(j+1/2)+\sqrt{(j+1/2)^2-(\alpha Z)^2}\right]^2}}} \tag{2.6}$$

which depends, in addition to n, on the total angular momentum j, in contrast to the solution 2.3 of the Schrödinger equation [Beth77]. This j dependence removes the degeneracy of some states with the same principal quantum number n, *e.g.* the $2\,p_{1/2}$ and the $2\,p_{3/2}$ states, which is known as the fine-structure splitting. However, states with the same n and j should have the exact same energy, *e.g.* the $2\,s_{1/2}$ and the $2\,p_{1/2}$ states. It was the famous experiment by Willis Lamb and Robert Retherford in 1947 [Lamb47], where they showed that the $2\,s_{1/2}$ state lies energetically slightly above the $2\,p_{1/2}$ state. This energy difference was from then on called the *Lamb shift*. Historically, only this difference is called the Lamb shift, however, nowadays every difference between the experimental result and the Dirac value is called Lamb shift and a prefix mentioning the related state is added. In this work, the precise determination of the $1\,s$ Lamb shift in hydrogen-like gold ${}^{197}_{79}\mathrm{Au}^{78+}$ is envisaged.

The Lamb shift can be calculated by taking two extensions of the Dirac equation into account. The first extension consists of quantum electrodynamical corrections, where the interaction of the electron with the quantum vacuum is treated. The second extension takes several effects of the nucleus, *e.g.* the finite size and the relativistic recoil, into account. These corrections are described in detail in the next two sections.

2.1.3 Quantum Electrodynamics

Quantum electrodynamics (QED) describes the interaction of charged particles via the exchange of *virtual* photons [Dyso49, Mohr98, Beye99]. A particle is called virtual, if it cannot be measured, but only its influence on a physical system, which suggests its temporary existence. Quantum electrodynamics contains the complete classical electrodynamics but extents it by the interaction of a charged particle with its own radiation field (self-energy) and its interaction with the so-called quantum vacuum (vacuum polarisation). Since QED contributions are assumed to be small corrections to the total binding energy, they can be treated within the framework of a perturbative series expansion in the coupling constant of the electromagnetic field, which is the well-known fine structure constant α. Similar to other series expansions in physics, such as the dipole approximation as a first-order approximation to the transition moment operator, the lowest-order terms contribute the most. The order of the considered correction is equal to the number of involved virtual photons. In the next two sections, the QED contributions with only one participating virtual photon will be examined, before treating higher-order terms.

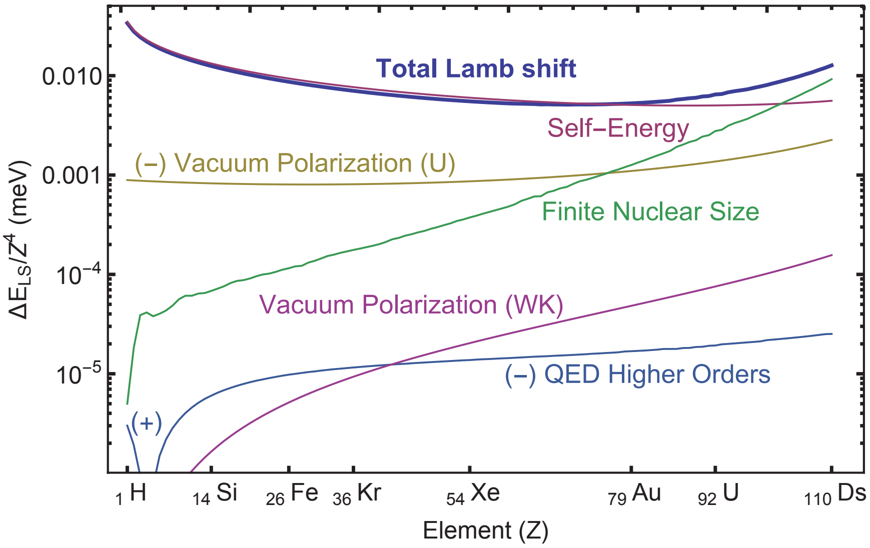

Figure 2.1: Individual contributions to the 1 s Lamb shift for H-like ions in the element range from hydrogen ($Z = 1$) up to darmstadtium ($Z = 110$). The ordinate is logarithmic and divided by Z^4, to separate out the strong scaling with the nuclear charge.

Self-Energy

The largest contribution of the QED part to the Lamb shift is given by the *self-energy* (SE) effect, which was first calculated for the hydrogen atom by Hans Bethe [Beth47], in the same year as Lamb and Retherford published their experimental result. It can be pictured with the help of a Feynman diagram 2.2, where a bound electron (double line) emits and re-absorbs a virtual photon (wavy line). Due to the re-absorption of the emitted photon, the energy is conserved at time scales which are given by the Heisenberg uncertainty principle, however, the trajectory of the particle gets distorted which leads to a weaker binding. Bethe also derived the scaling $\Delta E_{SE} \propto Z^4$ of this effect, which illustrates why it is desirable to examine heavy elements with a high nuclear charge Z. While this effect was experimentally very hard to detect in the hydrogen atom, it has a major influence on the binding energies in heavy elements.

Vacuum Polarisation

The *vacuum-polarisation* (VP) effect is displayed in the Feynman diagram 2.3. It describes the interaction between the bound electron and a virtual electron–positron

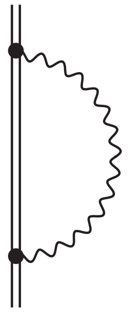

Figure 2.2: First order Feynman diagram of the self-energy effect (SE). The double line represents the electron (propagator), which is bound to the atomic nucleus. The wavy line illustrates the emission and re-absorption of a virtual photon. The black dots are called vertices and indicate where the electron couples to the electromagnetic field.

pair (double circle), in the Coulomb field of the nucleus, via the exchange of a virtual photon. This effect was first calculated by Edwin A. Uehling in 1935 [Uehl35] which pre-dates the discovery of Lamb and Retherford by twelve years. In 1956 Eyvind H. Wichmann and Norman M. Kroll [Wich56] added further corrections to the derivations of Uehling to obtain correct results in the regime of very strong Coulomb fields. The Uehling part shows the same Z^4 scaling as the self-energy part, whereas the Wichmann–Kroll corrections scale at least with Z^6 [Yero15]. For all elements in the periodic table the contribution of the vacuum polarisation is smaller than that of the self-energy and leads to a stronger binding. This fact lead Bethe to refuse Uehlings results in his publication [Beth47] (quote: "*Uehling* [...] *found that this effect also is much too small and has, in addition, the wrong sign.*").

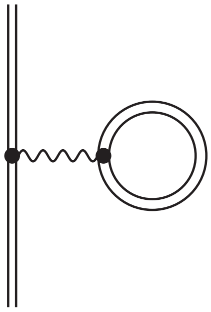

Figure 2.3: First order Feynman diagram of the vacuum-polarisation effect (VP). The double circle represents virtual electron-positron pair, coupling to the real electron via a virtual photon, in the central Coulomb field of the nucleus.

Higher-Order Corrections

As already mentioned, QED is treated in a perturbative framework. By taking higher-order contributions into account, better agreement with experimental results can be expected. This assumption is supported by several Lamb shift experiments (a survey can be found in [Yero15]), by high-precision measurements on the anomalous magnetic moment of the electron compared with tenth-order QED calculations [Kino14, Hann08], and by measurements of the hyperfine splitting of hydrogen-like ions [Ullm15]. However, in 1952, Freeman Dyson showed [Dyso52] that the power series expansion ansatz of QED will not converge, and hence no mathematical limit can be defined. Therefore, more precise experiments are needed to identify the validity region of QED.

Higher-order terms can be represented by arbitrary combinations of the Feynman diagrams 2.2 and 2.3. Some second-order diagrams are shown in figure 2.4. Since these terms contribute in the second order in α, it can be supposed that their influence is roughly 137 times weaker, which is supported by accurate calculations (see table 2.1). While higher-order contributions decrease the binding energy for low Z ions until Z = 4 (beryllium) it leads to a stronger binding for the remaining elements of the periodic table (see graph 2.1). Higher-order calculations on heavy hydrogen-like ions are only performed to second order since contributions due to the structure of the nucleus limit the theoretical precision, as will be shown in the next section.

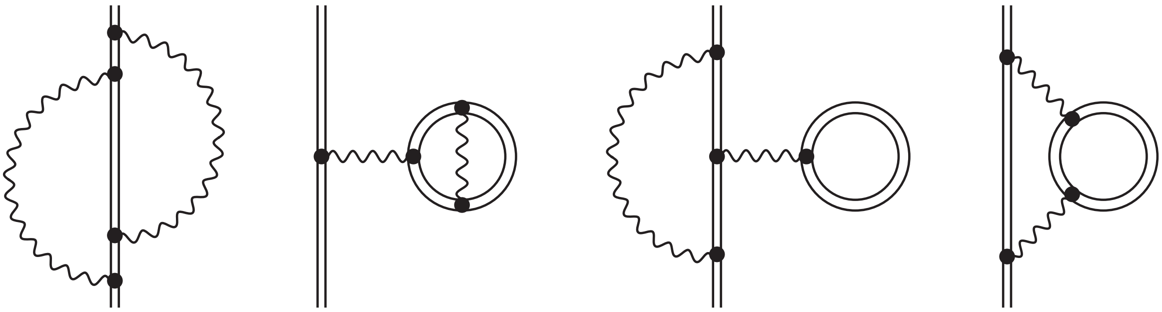

(a) SESE (b) VPVP (c) SEVP (d) S(VP)E

Figure 2.4: Some second-order Feynman diagrams where two virtual photons are being exchanged.

2.1.4 Nuclear Structure Effects

The influence of the nucleus on the transition wavelength has already been considered in the Rydberg formula 2.1, by using the element-depended Rydberg constant R. The correction includes only the nuclear recoil by utilising the reduced mass m. The leading-order relativistic recoil correction is given by

$$E_{recoil} = \frac{(m_e c^2)^2 - (m_e c^2 + E_{nj})^2}{2\,Mc^2} - \left[m - m_e + \frac{m_e^2}{M}\right] c^2\,\frac{(Z\alpha)^2}{2\,n^2} \tag{2.7}$$

with the nuclear mass M, the principal quantum number n and the Dirac energy eigenvalue E_{nj} [Yero15]. Further corrections to this analytic expression, which is important for very light ions, are calculated numerically. The recoil corrections only play a major role for light ions. For the heaviest elements it is almost negligible due to the huge nucleus to electron mass ratio ($M_{\mathrm{Au}}/m_e = 358\,970.10(2)$, [Wang12]).

As already mentioned in section 2.1.1, the existence of the nucleus is only included in the reduced mass of a quasi-particle moving in an external Coulomb field. This Coulomb field has been considered to be produced by a point-like charge, which is obviously not a proper assumption for heavy ions, due to their substantial spatial extension. The part of the electron wave function located inside the nucleus does not experience the full nuclear charge, which results in a weaker binding. An often used charge density function for heavy ions is a spherical symmetric Fermi distribution

$$\rho_F(r) = \frac{\rho_0}{1 + e^{(r-r_0)/a}} \tag{2.8}$$

with half density radius r_0, skin thickness parameter a, and the total charge normalisation constant ρ_0, chosen such that the volume integral of $\rho_F(r)$ is equal to the nuclear charge $Z\,e$ [Beye99]. In nuclear data tables normally the root mean square radius r_{RMS} is given instead of r_0, which can be transformed by the approximate formula

$$r_0 \approx \sqrt{\frac{5}{3} r_{\text{RMS}}^2 - \frac{7}{3} a^2 \pi^2} \tag{2.9}$$

which yields good results for sufficiently small values of a. The RMS radius for gold is given by $r_{\text{RMS}}^{\text{Au}} = 5.4371(38)\,\text{fm}$ [Ange13], and $a = 0.52\,\text{fm}$ has been chosen [Yero15]. With the charge distribution 2.8 the modified Coulomb potential can be calculated, and be used as an input parameter for the Dirac equation, which now has to be solved numerically. The energy shift due to this modified Coulomb potential is called the *finite nuclear size* (FNS) contribution. For hydrogen-like gold, it is the second-largest contribution to the 1s Lamb shift, after the self-energy. However, the finite nuclear size scales strongly with Z, making it the dominant contribution for $Z \gtrsim 100$, as shown in graph 2.1.

In the evaluation of the finite nuclear size effect, the charge distribution has been assumed spatially extended but steady in its shape. However, if an electron is interacting with the nucleus, also the charge distribution in the nucleus is affected, leading to a modified Coulomb field, which is called *nuclear polarisation* [Plun95, Nefi96]. The distortion acts back on the electron motion, and hence changes the level energy. These calculations are demanding since basically the whole nuclear structure has to be taken into account. Therefore, a 100 % uncertainty is attributed to these estimations [Yero15].

2.1.5 The Total Lamb Shift

The total value for the Lamb shift is composed of all of the above-mentioned contributions. To obtain a simple formula describing the complex behaviour of the Lamb shift, all known analytic dependencies, such as the already mentioned Z^4 scaling, are separated out and a slow-varying function $F(Z\alpha)$, containing all the sophisticated physics, is introduced

$$\Delta E_{LS} = m_e c^2 \, \frac{\alpha}{\pi} \, \frac{(Z\alpha)^4}{n^3} \, F(Z\alpha) \tag{2.10}$$

The function $F(Z\alpha)$ is provided by pre-calculated tables [John85, Yero15] for all elements up to $Z = 110$ (darmstadtium) with uncertainties basically limited due to higher-order QED contributions and the lack of knowledge of the nuclear size (the RMS radius). In table 2.1 the individual contributions to the 1s Lamb shift of hydrogen-like gold are listed.

Effect	Contribution (eV)
Dirac Energy	$-93\,459.863$
First-Order QED	
Self-Energy (SE)	$+196.687(2)$
Vacuum-Polarisation (VP)	
Uehling	$-41.996(2)$
Wichmann-Kroll	$+1.7939(2)$
Second-Order QED	
SESE	$-0.6716(43)$
SEVP	$+0.41(13)$
VPVP	$-0.39(11)$
Nuclear Contributions	
Finite Nuclear Size (FNS)	$+49.14(11)$
Nuclear Recoil	$+0.3313(14)$
Nuclear Polarisation	$-0.049(49)$
Total Lamb Shift	$205.2(2)$
Total Binding Energy	$-93\,254.6(2)$

Table 2.1: Individual theoretical contributions to the 1 s Lamb shift in hydrogen-like gold Au^{78+} [Yero15].

Table 2.2 compiles the binding energies, Lamb shifts and energy separations to the $1\,s_{1/2}$ state for the lowest lying states with $n \leq 3$ in hydrogen-like gold Au^{78+}.

State	Binding Energy (eV)	Lamb shift (eV)	Energy to 1s (eV)	Reference
$1\,s_{1/2}$	$-93\,254.6(2)$	$205.2(2)$	–	[Yero15]
$2\,s_{1/2}$	$-23\,889.62(3)$	$35.43(3)$	$69\,365.0(2)$	[Yero15]
$2\,p_{1/2}$	$-23\,922.149(5)$	$2.904(5)$	$69\,332.5(2)$	[Yero15]
$2\,p_{3/2}$	$-21\,684.201(5)$	$4.349(5)$	$71\,570.4(2)$	[Yero15]
$3\,s_{1/2}$	$-10\,364.2$	10.6	$82\,890.4$	[Desc75]
$3\,p_{1/2}$	$-10\,373.7$	1.2	$82\,880.9$	[Desc75]
$3\,p_{3/2}$	$-9\,706.9$	1.5	$83\,547.7$	[Desc75]
$3\,d_{3/2}$	$-9\,708.5$	-0.1	$83\,546.1$	[Desc75]
$3\,d_{5/2}$	$-9\,523.2$	0.3	$83\,731.4$	[Desc75]

Table 2.2: Summary of the theoretical binding energies, Lamb shifts and energy separations to the 1 s state in hydrogen-like gold Au^{78+}. The values for the $n \leq 2$ states have been taken from [Yero15], while the other values have been calculated with a relativistic multiconfiguration Dirac-Fock program [Desc75, Tras15].

2.2 The Diffraction of X Rays in Crystals

Crystal spectrometers are known for their exceedingly high resolving power in the x-ray and γ-ray regime. The core element of each spectrometer is the crystal, which disperses a polychromatic x-ray beam into monochromatic rays, leaving the crystal under different angles, according to the Bragg equation. In this section, the basics of the theory of x-ray diffraction in crystals is treated and the practical applications of these findings for the construction of a spectrometer are given.

2.2.1 The Bragg Equation

The diffraction of light in the optical regime is well known ever since Thomas Young conducted his famous double-slit experiment at the beginning of the nineteenth century [Youn02]. He demonstrated that light behaves like waves which can interfere and thus form the observed diffraction pattern. He was also able to derive the correct wavelengths λ for the different colours of light, which span a few hundreds of nanometres in range [Youn02]. This method of using optical gratings to determine the wavelength of light became very important, and is still in use (see *e.g.* [Rei15]). To generate an interference pattern, the slit spacing of the double slit has to be of the same order of magnitude as the wavelength of the light. While in the visible regime, *i.e.* $300\,\mathrm{nm} < \lambda < 800\,\mathrm{nm}$, optical gratings can still be machined, this is impossible for hard x rays with wavelengths in the range of a few picometres ($10^{-12}\,\mathrm{m}$), which is comparable to the size of atoms. In 1912, Max von Laue was the first to observe the diffraction of x rays on the atomic planes in crystals [Laue13]. These crystals act as natural gratings, with lattice constants of the required magnitude. One year later, W.L. Bragg and W.H. Bragg gave the first quantitative description of the diffraction process by considering that the path difference of x rays, diffracted on subsequent lattice planes in the crystal, should be equal to a integer multiple n of the wavelength λ to interfere constructively [Brag13].

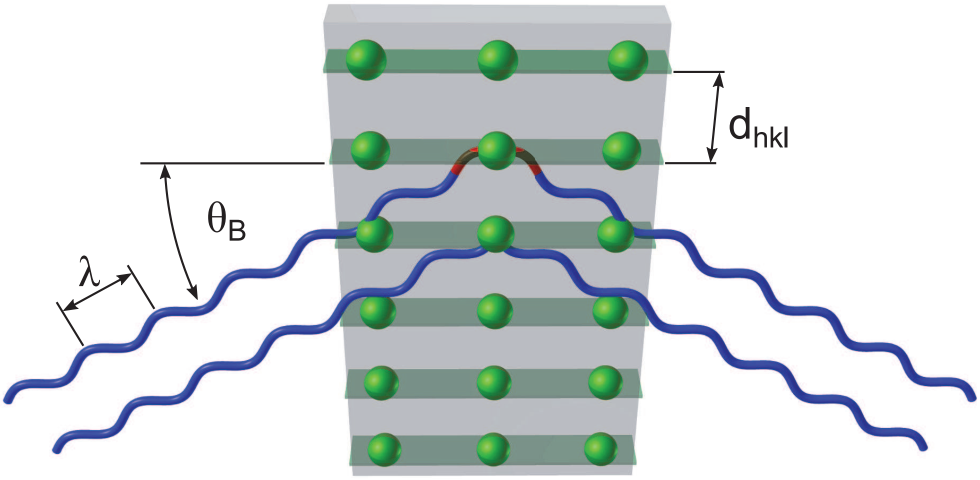

Figure 2.5: Illustration of the diffraction of x rays according to Bragg's law. The x-ray waves are scattered at two successive atomic lattice planes (green), leading to an incidence angle dependent path difference of the rays (red). If the path difference is equal to an integer multiple of the wavelength λ, constructive interference occurs. The according incident angle is referred to as Bragg angle θ_B.

Figure 2.5 depicts the situation in the so-called *Laue mode*, where the incident x-ray beam traverses the crystal and is then scattered on the lattice planes oriented perpendicular to the crystal surface. This is in contrast to the *Bragg mode*, where the x rays being diffracted on lattice planes parallel to the surface, and leave the crystal on the same side as they entered. The path difference depends on the lattice spacing d_{hkl} and the incident angle θ. By applying basic trigonometry, the Bragg equation

$$n\,\lambda = 2\,d_{hkl}\,\sin(\theta_B) \tag{2.11}$$

is obtained. θ_B is called the Bragg angle, and defines that angle θ which fulfils the Bragg equation. This equation is an important finding since it shows that the wavelength of x rays can be measured, by scanning the angle θ for reflexes, if the lattice spacing d_{hkl} is known, or vice versa. Although the Bragg equation predicts the direction θ_B for constructive interference of the waves correctly, it makes no prediction about the scattered intensity. Even if 100 % scattering is assumed (which is true for a thick, non-absorbing crystal in Bragg mode) the integrated intensity is zero since the Bragg equation is only satisfied exactly for the Bragg angle, and gives zero intensity for all other angles. To resolve this issue and to obtain finite scattering intensities the geometrical theory of x-ray diffraction has been developed.

2.2.2 The Geometrical Theory of X-Ray Diffraction

The geometrical theory of x-ray diffraction (sometimes also called *kinematical theory*) describes the diffracted *intensity* of a thin, non-absorbing crystal, and was the first generalisation of the Bragg theory. The x rays are scattered by the atomic electrons making up the crystal, therefore, the scattered intensity is linked to the coherent scattering cross section of a free electron, namely the Thomson cross section σ_T, and a function f correcting for the binding of the multiple atomic electrons. The atom scattering cross section σ_A is given by

$$\sigma_A = \sigma_T\,|f|^2 = \frac{8\pi}{3}\,r_e^2\,|f|^2 \tag{2.12}$$

with the classical electron radius r_e, and the function f, called the *complex atomic scattering factor*, depending on the wavelength and the direction of the scattered x rays [Attw99]. It can be calculated within a quantum-mechanical treatment of the scattering off atoms. The results can be found in tables [Waas95, Henk93] and are implemented in many modern computer codes like XOP [Rio11]. To obtain the total intensity scattered by a crystal, not just the single-atom contribution, given by σ_A, but also its crystalline structure has to be considered. This is done by introducing the *structure factor* F_{hkl}

$$F_{hkl} = \sum_j f_j\, e^{2\pi i\,(x_j h + y_j k + z_j l)} \tag{2.13}$$

which sums over all atoms j in the unit cell at the position $r_j = (x_j, y_j, z_j)^T$, in units of the unit cell dimension [Auth01]. The Laue indices h, k and l define a set of equivalent lattice planes on which the scattering occurs. The lattice spacing d_{hkl} for a cubic crystal is linked to the lattice constant a (the unit cell dimension) and the Laue indices via

$$d_{hkl} = \frac{a}{\sqrt{h^2 + k^2 + l^2}} \tag{2.14}$$

After having the material, and structure-related dependencies defined, the actual ansatz for the geometrical theory can be formulated. It is assumed that a small, non-absorbing crystal block with thickness t is entirely irradiated by an x-ray wave field with an intensity I_0. Each scattering centre (atom) experiences the same field strength, interactions of the wave field with other atoms prior to the current observed atom are neglected. The intensity of the diffracted radiation I_D in the direction θ is obtained by adding up the amplitudes of the scattered waves for each individual scattering centre, which will differ in phase due to varying path lengths. By conducting the summation, the following result for the reflectivity R is obtained

$$R(\Delta\theta) = \frac{I_D}{I_0} = \frac{{r_e}^2 \lambda^2 \left(1 + \cos^2\left(2\,\theta_B\right)\right)}{2\sin^2\left(\theta_B\right)}\, n^2 \left|F_{\mathrm{hkl}}\right|^2 \left[\frac{\sin\left(2\pi\, t\, \cos\left(\theta_B\right) \Delta\theta/\lambda\right)}{2\pi\, d_{hkl} \cos\left(\theta_B\right) \Delta\theta/\lambda}\right]^2 \tag{2.15}$$

with the deviation from the Bragg angle $\Delta\theta = \theta - \theta_B$, and the scattering centre density n, which is given by the number of atoms per surface area [Auth01]. The function $R(\Delta\theta)$, defining the reflectivity of a crystal in dependence of the angle, is called *rocking curve*, and is shown in figure 2.6 (labelled with “Thin Crystal”).

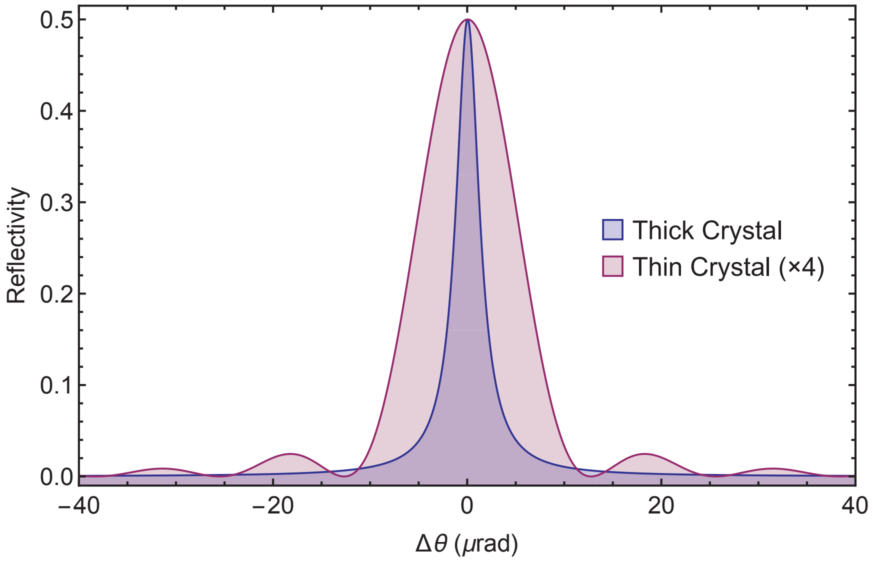

Figure 2.6: Blue: Rocking curve for a thick crystal, calculated with the program XOP, which utilises the dynamical theory of x-ray diffraction. Red: Rocking curve for a thin crystal, calculated with the geometrical theory. The intensity of this curve has been multiplied by a factor 4, for the sake of better comparability.

From formula 2.15 it can be shown [Auth01] that the height and the width of the central peak ($\Delta\theta = 0$) scales like $R(0) \propto \lambda^2 t^2$ and FWHM $\propto \lambda/t$, respectively. Hence, the total reflectivity (*i.e.* the integral of $R(\Delta\theta)$ over the whole $\Delta\theta$ range) scales like

$$R_{int} \propto \lambda^3 \, t \tag{2.16}$$

2.2.3 The Dynamical Theory of X-Ray Diffraction

While the geometrical theory of x-ray diffraction was the first model able to predict scattering intensities and peak widths, its limitations are obvious. From the scaling law 2.16 it follows that the integrated reflectivity would exceed all limits for an infinitely thick crystal, which is a clear violation of the conservation of energy. The scaling behaviour for the height and the width of the peak also suggest that it would resemble a delta distribution $\delta(\Delta\theta)$ with an infinitesimal width for a thick crystal, which is non-physical. Effects like photoelectric absorption and incoherent scattering (Compton scattering) are also neglected. The conservation of energy is violated, since the effect of *extinction* is not regarded. Extinction describes the decrease of the intensity I_P of the incident (primary) beam in favour of an increasing intensity I_D of the diffracted beam, while traversing the crystal. From figure 2.5 it becomes also clear that multiple Bragg reflections inside a crystal are possible, since a wave which is diffracted, could fulfil the Bragg condition at subsequent traversed lattice planes. The combination of multiple scattering and extinction makes it possible to deduce the true maximum reflectivity in a thick, non-absorbing crystal, without solving any equations. For the Laue case, the incident beam has the total intensity $I_P = 100\,\%\; I_0$ at the entrance surface of the crystal, while the diffracted beam I_D has zero. After having traversed a few lattice planes, a small fraction of I_P has gone to the diffracted beam I_D. This procedure continues in this manner for the next lattice planes, but, in addition, also the scattering from the diffracted beam back to the original beam increases due to multiple Bragg reflections. For a thick crystal ($t \to \infty$), a steady state will be reached, where $I_P = I_D = 50\,\%\; I_0$, since then the scattering into the opposite beam is exactly counterbalanced. In a similar way, it can be shown that, for the Bragg case (also in the thick, non-absorbing limit) follows $I_P = 0\,\%\; I_0$, $I_D = 100\,\%\; I_0$, meaning that all the incident intensity from the incident beam is transferred to that of the diffracted beam.

All above-mentioned shortcomings led to the development of the *dynamical theory* of x-ray diffraction. To start with a correct model, the macroscopic Maxwell equations are used. By combining them, the following expression for the electric displacement field $\mathbf{D}$ is obtained

$$\nabla \times [\nabla \times (1 - \chi_e)\mathbf{D}] = -\frac{1}{c^2}\frac{\partial^2 \mathbf{D}}{\partial t^2} \tag{2.17}$$

with the electric susceptibility χ_e [Zach67]. In order to solve this equation, the periodicity of the crystal, and, hence, of χ_e is used. For perfect crystals, with an arbitrary thickness t and non-vanishing absorptions, this can be done analytically, which is shown in standard literature [Zach67, Auth01] or summarised in publications

[Batt64, Rio15]. The solutions for the Bragg and Laue cases are quite lengthy and complicated, making it hard to gain deeper insight by simply listing them. Therefore, just the result for the reflectivity $R(y)$ for a thick, non-absorbing crystal in Laue configuration is given

$$R(y) = \frac{1}{2}\frac{1}{1+y^2} \tag{2.18}$$

with the Zachariansen y variable, which is basically proportional to the deviation from the Bragg angle $y \propto \Delta\theta$ [Zach67]. The reflectivity $R(y)$ has a Lorentzian shape as shown in figure 2.6, where it is labelled with “Thick Crystal”. As already mentioned, the curve has a peak value of $R(0) = 50\,\%$ and the width does not depend on the thickness in the thick, non-absorbing crystal limit. Therefore, no increase of the integrated reflectivity can be expected if a certain crystal thickness is exceeded, and it even drops if absorption is taken into account. These findings set an upper limit for the maximum integrated reflectivity of a perfect flat crystal that cannot be surpassed.

2.2.4 The Reflectivity of Cylindrically Bent Crystals

The theory discussed in the previous sections is valid only for perfect, unstrained crystals. However, many studies addressed the transmission and diffraction of x rays from elastically deformed crystals in the middle of the past century [Hunt58, Borr59, Hild59]. The deformation was obtained by applying a temperature gradient or mechanical stress to the crystals. If a symmetric Laue crystal, where the lattice planes are oriented perpendicular to the crystal surface (figure 2.7 (a)), is bent cylindrically, the rocking curve does not differ from the unstrained case. This seems surprising at first, since the lattice planes are not parallel anymore, and would converge on a fanning point F, which coincides with the centre C of the bending cylinder with radius R (figure 2.7 (b)). This apparent contradiction can be resolved by considering that also the inclinations of the lattice planes change from plane to plane over of the crystal, which exactly counterbalances the beforehand mentioned effect. However, if the lattice planes are asymmetric, *i.e.* they exhibit an angle χ (not to be confused with the electric susceptibility χ_e) deviating from the perpendicular case (figure 2.7 (c)), the effects do not counterbalance each other anymore. This is due to the non-flat lattice planes (figure 2.7 (d)), which curve the x-ray path in the same direction as the lattice planes [Hild59]. Also the fanning point F and the bending centre C of the crystal deviate from each other by the asymmetry angle χ.

Within the dynamical theory of x-ray diffraction it is not possible to calculate the rocking curve of a bent crystal, since the periodicity in the electric susceptibility is no longer given, which was an important requirement to solve equation 2.17 [Auth01]. Therefore, P. Penning and D. Polder developed an approximate method, which assumes that the solution of the dynamical theory still holds locally in a small crystal volume and changes due to the bending very slowly within the crystal [Penn61, Rio15].

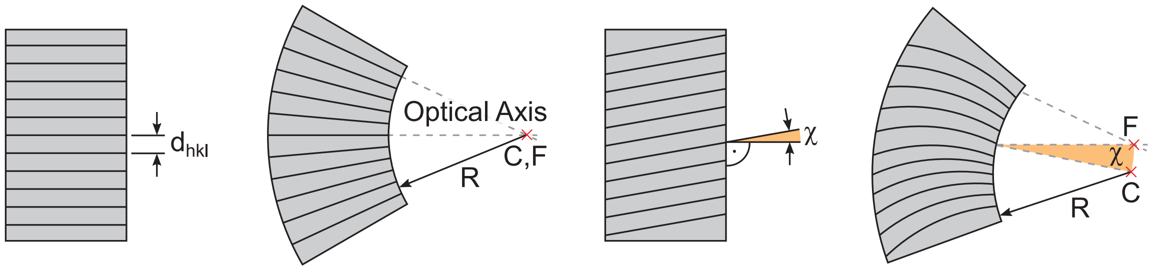

(a) Flat crystal (b) Bent crystal (c) Flat asymmetric crystal (d) Bent asymmetric crystal

Figure 2.7: Various single crystal configurations. The crystals (a)–(c) exhibit a rocking curve as shown in figure 2.6, while the bent asymmetric crystal (d) shows a broadening of the rocking curve as depicted in figure 2.8.

The model gives reasonable results for weakly deformed crystals, and is implemented in modern crystal optics codes like XOP [Rio97, Rio11]. Figure 2.8 shows the rocking curves for a bent crystal with varying asymmetry angles χ, according to the model of Penning and Polder.

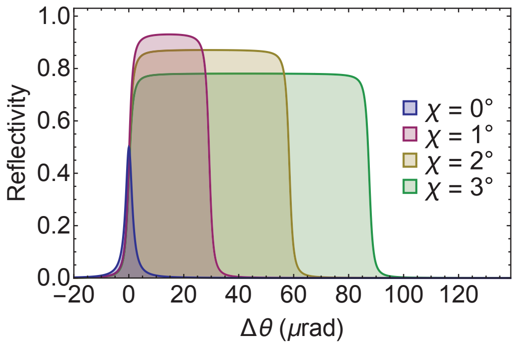

Figure 2.8: Rocking curves for different asymmetry angles χ. For a symmetric crystal cut ($\chi = 0°$) the profile does not differ from the unstrained case (figure 2.6), whereas it gets broader with increasing asymmetry angle.

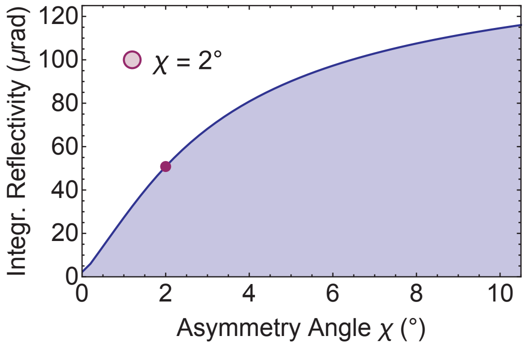

Figure 2.9: Dependence of the integrated reflectivity of a cylindrically bent crystal on the asymmetry angle χ. The curve was calculated for a silicon (220) crystal with a bending radius of $R = 2\,\mathrm{m}$.

As already mentioned, the curve for $\chi = 0°$ is the same as for a flat crystal (see figure 2.6). But with increasing χ, the width and the maximum reflectivity, and, hence, the integrated reflectivity, rises. This can be explained by the curved ray path, which then satisfies the Bragg condition within a wider angle interval. Figure 2.9 shows the steep increase of the integrated reflectivity as a function of asymmetry angle, which can be used to enhance the efficiency of crystal spectrometer.

2.2.5 The Flat Crystal Spectrometer

In the previous sections, the theoretical foundation of x-ray diffraction in crystals has been set. Now, these findings are used to construct a reliable apparatus capable to determine the wavelength of hard x-ray radiation with very high precision. Such a device is called a *crystal spectrometer*, since it uses a crystal to disperse the radiation to be measured [Blok65]. A very basic design for such an apparatus can be seen in figure 2.10.

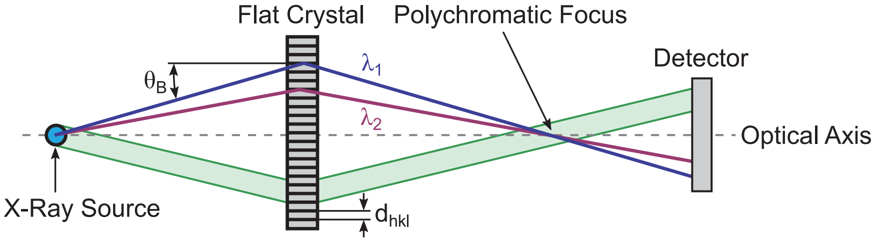

Figure 2.10: Crystal spectrometer with a Laue crystal. The x-ray source on the left emits radiation that is diffracted by the flat crystal. X rays with different wavelength (red and blue lines) hit the detector at different distances z_d from the optical axis. The image of an extended source on the detector screen appears blurred (green band).

It consists of an x-ray source on the left, which emits radiation in all directions and at two different wavelengths $\lambda_{1,2}$. A part of it, depicted as red and blue lines, hits the flat crystal and is reflected if the Bragg condition 2.11 is satisfied. The crystal is operated in the Laue configuration, since it is penetrated by the radiation. From Bragg's law follows that $\lambda_1 > \lambda_2$ since the Bragg angle θ_B of the λ_1 radiation is greater than that of λ_2. The radiation converges to a so-called *polychromatic focus* where all the diffracted radiation passes through, independent of its wavelength. The existence of such a focal point can be understood when considering the flat crystal as a stack of horizontal mirrors, mapping the source radiation from the left hand side onto the same position on the right hand side of the crystal. After passing through the polychromatic focus, the radiation diverges again. By putting some kind of radiation-sensitive screen, or a position-sensitive detector, at some arbitrary distance d_{PD} behind the polychromatic focus, the spacing z_d between the optical axis and the radiation impinging location can be measured. It is linked to the wavelength λ by the following formula

$$\lambda = 2\, d_{hkl} \frac{z_d}{\sqrt{d_{PD}^2 + z_d^2}} \tag{2.19}$$

By utilising this formula, the wavelength of radiation can, in principle, be determined, if all the other parameters are known. In the deduction made so far, a point-like source was assumed. If the influence of an extended source is taken into account, which has to be done in a real-world scenario, it is not convenient to use such an apparatus. This is illustrated by the green band in figure 2.10, which indicates the ray path of monochromatic radiation emitted by a source with a finite size. The detector will record a rather blurred band instead of a narrow line, making it hard to determine the line centre very precisely. Due to this, such spectrometers are rarely used in reality and devices with a focusing characteristic have been developed.

2.2.6 The Focusing Crystal Spectrometer

In 1932, Yvette Cauchois introduced a design for a Laue-type spectrometer with focusing properties [Cauc32, Cauc33]. The main difference to the spectrometer discussed in the previous section, is the usage of a cylindrically bent crystal. In figure 2.11 a similar layout to Cauchois' proposal is shown.

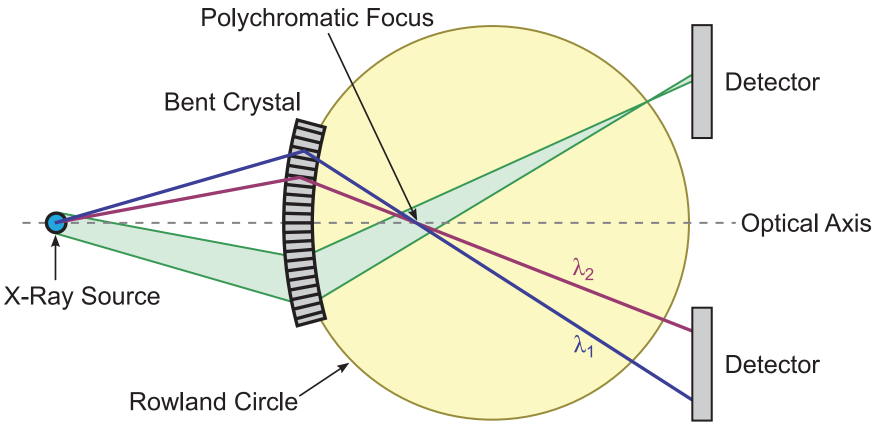

Figure 2.11: Layout of a focusing spectrometer with a bent crystal in Laue configuration. Similar to figure 2.10, x rays with different wavelengths hit the detector at different distances z_d form the optical axis, but, in addition, a focusing of an extended source on the Rowland circle can be observed.

Due to the bend, the polychromatic focus is shifted closer to the crystal. The focusing of the radiation emitted by an extended source is optimal only on the edge of the focal circle, which fixes the location of the position sensitive detector onto its boarder. The focal circle (drawn in yellow) is also called *Rowland circle*, its radius r is exactly half of the crystal bending radius R.

$$R = 2\,r \tag{2.20}$$

The Rowland circle touches the bent crystal tangentially at its concave side, and intersects the optical axis at the diametrically opposed point, which also coincides with the centre of curvature and the fanning point of the bent crystal, *i.e.* the points C and F in figure 2.7 (b). For the focusing spectrometer, the wavelength λ of the radiation is linked to the distance from the optical axis z_d via

$$\lambda = \frac{2\,d_{hkl}}{R}\,z_d \tag{2.21}$$

and its absolute value can be determined if all the other quantities are known. This would require that all parameters in formula 2.21 are known with very high precision. The lattice spacing is well known for various materials and crystallographic directions (hkl). For example, the (220) spacing in silicon is [Mohr16]

$$d_{220} = 192.015\,571\,4(32) \times 10^{-12}\,\mathrm{m} \tag{2.22}$$

As will be shown in section 5.2.1 for the measurement of the curvature radius R, and in section 5.1.5 for the determination of the line position z_d, such an approach is not feasible since the required precision is by far not achievable. Therefore, a focusing spectrometer is normally used as a *wavelength comparator*, where only the relative distance Δz between a known calibration line (*e.g.* λ_1 in figure 2.11) and an unknown transition (*e.g.* λ_2 in figure 2.11), and the spectrometer dispersion $D = d\lambda/dz_d$ are considered

$$\lambda_2 = \lambda_1 + D\,\Delta z \tag{2.23}$$

The dispersion D is obtained experimentally by calibration measurements, as will be explained in section 5.1.3. To minimise the influence of the uncertainty linked with an experimental determination of the dispersion, it is desirable to use a calibration transition which has a similar wavelength as the unknown transition, if its wavelength is roughly known or predicted by theoretical calculations ($\lambda_1 \approx \lambda_2 \Rightarrow \Delta z \approx 0$).

Crystal spectrometers can measure wavelength with the highest resolution among all competing approaches. However, the efficiency of such instruments is comparably low, and compromises between resolution and efficiency have to be made. This trade-off of resolution versus efficiency is covered in section 4.1.1 and especially in graph 4.5 for the FOCAL spectrometer, which will be treated in the course of this work.

2.3 Magnetic Microcalorimeters for X-Ray Spectroscopy

In this section, a rather new method to measure the energy of x-ray photons is presented, which is complementary to the crystal spectrometer. While a crystal spectrometer is used to measures the diffraction angle, and hence the photon wavelength, a *microcalorimeter* utilises the temperature rise of an absorber, after being hit by an x-ray photon, to conclude on its energy. Microcalorimeters are categorised in different groups, according to the technique used to measure the induced temperature change. In this work, the micro-calorimeter arrays for high-resolution x-ray spectroscopy maXs are treated, which base on the so-called metallic magnetic calorimeter technology, being developed in a close collaboration with the research group of Prof. Christian Enss from the Kirchhoff-Institut für Physik in Heidelberg [Enss16].

2.3.1 Principle of a Metallic Magnetic Microcalorimeter

The principle of the microcalorimeter is shown in figure 2.12. An x-ray photon with a certain energy E_γ hits the absorber and transfers its energy via the photo effect to an electron in the material. After about $10^{-13}\,s$, this high-energy electron has lost

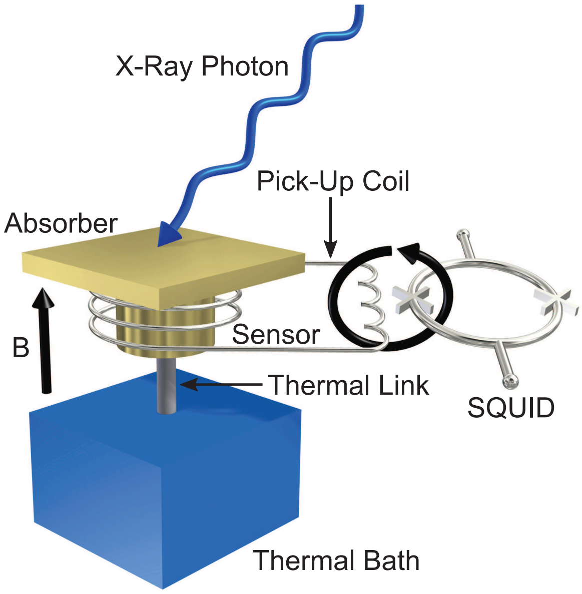

Figure 2.12: An x-ray photon hits the absorber of a metallic magnetic calorimeter and increases its temperature. The paramagnetic sensor is in good thermal contact to the absorber and changes its magnetisation as a result of the temperature change. To keep the magnetic flux through the superconducting pick-up coil constant, a mirror current is induced which is inductively coupled to a SQUID magnetometer. The SQUID reads out the magnetisation change, and converts it to a voltage, which is then measured.

almost all its energy due to electron-electron scattering [Enss00a], and the absorber temperature rises according to

$$\Delta T = \frac{E_\gamma}{C_{tot}} \tag{2.24}$$

with C_{tot} being the total heat capacity of the absorber. Due to the calorimetric measurement principle, not only photons, but all particles which transfer their energy to the absorber can be measured. In this work, photons are the only relevant particles, therefore, the further discussion is restricted to them. Since the photon energy is given by the physical effect to be observed, with typical values around $E_\gamma \approx 60\,\text{keV} \approx 10^{-15}\,\text{cal}$, a comparably low heat capacity C_{tot} has to be used in order to generate a detectable temperature change ΔT. The heat capacity C of a conductor is given by

$$C = V\left(\gamma T + \beta T^3\right) \tag{2.25}$$

with the volume V at a temperature T. The parameters γ and β are material-dependent constants. A low heat capacity is obtained if the calorimeter is operated at *cryogenic temperatures* ($T \ll 1\,\text{K}$), and if the volume of the absorber is *microscopically small* (*e.g.* $V \approx 250 \times 250 \times 5\,\mu\text{m}^3$). Therefore, it is called microcalorimeter. Different material classes can be used for the absorber. If the heat capacity should be optimised, a dielectric material would be preferable, because then $\gamma = 0$ in equation 2.25. On the other hand, electrons in the conduction band of a conducting material lead to a much faster distribution of the heat, and thermal equilibrium is reached earlier, resulting in a faster detector response. Also from photon stopping-power considerations, a metal would be desirable, since the cross section of the photoelectric effect scales approximately like $\sigma \propto Z^4$ with the atomic number Z of the material. Typical absorbers are made of gold and operate at a temperature $T_{op} \leq 50\,\mathrm{mK}$, with heat capacities around $1\,\mathrm{pJ/K}$, resulting in a temperature change of $\Delta T \approx 10\,\mu\mathrm{K}$, if a $60\,\mathrm{keV}$ photon has been absorbed [Pies12b]. Through the weak thermal link with conductance G, the temperature of the absorber relaxes with the time constant

$$\tau_1 = \frac{C}{G} \tag{2.26}$$

to the temperature of the thermal bath, which is kept at the operating temperature by means of a commercial $^3\mathrm{He}/^4\mathrm{He}$ dilution refrigerator [Blue16]. This ensures stable operation conditions for the next photons to be registered.

2.3.2 The Paramagnetic Temperature Sensor

The temperature rise ΔT of the absorber is measured by a thermometer for which different technical realisations exist. Early results were achieved with *thermistors*, where the temperature dependent resistance was measured to infer the temperature change. *Transition edge sensors* have similar properties although the used material is operated in the normal conducting – superconducting transition temperature, where the change of resistance is up to two orders of magnitude higher. A survey of the different thermometer types can be found in [Enss05]. In this work, the principle of a *metallic magnetic calorimeter* will be treated [Pies12a].

The metallic temperature sensor consists of gold, doped with a few hundred ppm of the rare earth metal erbium (Au:Er). The erbium atoms occupy regular atomic sites in the gold lattice and supply three electrons each to the conduction band of the alloy. The whole sensor is in good thermal contact with the absorber and is superimposed by an external magnetic field B (see figure 2.12). The magnetic behaviour of the sensor material is completely determined by the Er^{3+} ions, making it a paramagnetic substance [Flei05]. At cryogenic temperatures ($T < 100\,\mathrm{mK}$) the ground state of the Er^{3+} ions is well characterised by a two-level system with a quasi-spin $\tilde{S} = 1/2$ and a Landé factor $\tilde{g} = 34/5 = 6.8$ [Flei05]. Due to the magnetic field, the degeneracy of the ground state is removed, and exhibits a Zeeman splitting of the energy

$$\varepsilon = \tilde{g}\,\mu_B\,B \tag{2.27}$$

with the Bohr magneton μ_B. This Zeeman system is another possibility to store (heat) energy and is linked to the heat capacity C_Z. Together with the heat capacity of the conduction-band electrons C_e, it is the main contributor to the total heat capacity of the sensor-absorber unit, which is given by the sum

$$C_{tot} = C_Z + C_e + C_{ph} \tag{2.28}$$

with the additional heat capacity of the phonons C_{ph}, which is negligible compared to the other contributions. Due to the good coupling of the conduction-band electrons to the quasi-spin of the erbium ions, the heat is transported to the Zeeman system very fast generating an almost instantaneous response. If the thermal link between the electrons and the spins is denoted by the conductance G_Z, the characteristic time scale is given by $\tau_0 = C_Z/G_Z$. To the spin system a certain temperature-dependent magnetisation

$$M(T) = \frac{\tilde{g}\,\mu_B}{2}\,\frac{N}{V}\,\tanh\frac{\varepsilon}{2\,k_B T} \tag{2.29}$$

is linked, with the magnetic ion number per volume N/V and the Boltzmann constant k_B [Pies12b]. For high temperatures it shows the typical Curie behaviour $M \propto 1/T$, whereas it saturates for very low temperatures to $M = \tilde{g}\,\mu_B\,N/2V$. It is this temperature-dependent magnetisation which is used to monitor the temperature rise of the x-ray absorber. For this purpose the paramagnetic sensor is enclosed by a superconducting pick-up coil (see figure 2.12), which ensures that the included magnetic flux Φ is constant at all times. If the temperature of the sensor changes due to the absorption of an x-ray photon, also its magnetisation changes. This changes the local magnetic flux through the sensor. Since the magnetic flux has to be conserved, an image current ΔI in the pick-up coil is induced to compensate for the magnetisation change. The image current generates a time-dependent magnetic field, which is inductively coupled to a superconducting quantum interference device (SQUID) [Drun96]. The SQUID is a very sensitive magnetometer converting magnetic flux to a voltage signal. This signal is further amplified by subsequent electronics, as will be shown in the next paragraph.

2.3.3 The SQUID Magnetometer

A more realistic schematic of the calorimeter realisation is shown in figure 2.13. The meander-shaped pick-up coil is covered by two (gold coloured) paramagnetic sensors, from now on called pixel. A persistent current I_0 in the coil generates the magnetic field responsible for the Zeeman splitting of the Er^{3+} ground state. In the steady state, when no x-ray photon has hit a pixel, the current to the SQUID coil is zero, $\Delta I = 0$.

If one of the pixels is hit, the compensation current ΔI flows only through the meander-shaped part of that pixel and the SQUID coil, which induces a flux change in the SQUID. Both pixels produce equivalently strong signals, but with an opposing sign, making it possible to distinguish between the pixels, due to the polarity of the signal. The usage of two pixels in the so-called gradiometric configuration cancels small drifts of the thermal bath temperature due to the opposing polarity of the signals, making the system more robust. The SQUID itself is basically a superconducting ring through which a constant electric current I_b is driven. At two positions

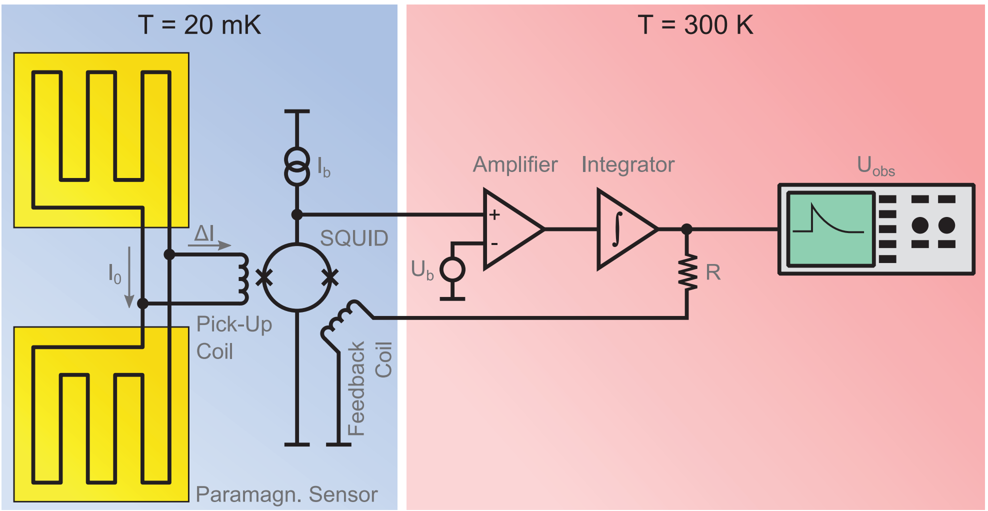

Figure 2.13: Schematic of the actual wiring of two pixels (in gold) in a gradiometric configuration. The first SQUID amplification stage at cryogenic temperatures is further amplified by conventional electronics at room temperature. The voltage signal is coupled back to the original SQUID by a feedback coil to operate it at a stable working point. The signal is read out by a digital oscilloscope and the pulses are stored on a computer for later analysis.

the ring is interrupted by a thin non-conducting layer, acting as Josephson junctions [Drun96]. Through the non-conducting Josephson junctions the magnetic field lines can enter the inside of the ring, and thereby change the included magnetic flux of the SQUID. The current I_b, in the form of Cooper pairs, may tunnel through the Josephson junctions, if the layer is thin enough and the current is smaller than a certain critical current $I_b < I_c$ [Enss00b]. If the current through the SQUID is higher than the critical current $I_b > I_c$, a voltage drop U_{SQUID} across the Josephson junctions can be measured. The voltage is a non-linear and periodic function of the magnetic flux inside the ring with a periodicity of the magnetic flux quantum

$$\Phi_0 = \frac{h}{2\,e} \tag{2.30}$$

The ‘2’ in the denominator indicates that the current is carried by *two* electrons, namely the Cooper pairs. To linearise the voltage $U_{SQUID}(\Phi)$, the signal is amplified and inversely fed back to the SQUID by means of a feedback coil. This procedure ensures that the SQUID is operated at a stable working point, which is ideally chosen in such a way, that it exhibits the maximum sensitivity of the SQUID. This voltage signal is also monitored by a digital oscilloscope, which digitises the signal traces and stores it for later analysis.

2.3.4 Energy Resolution of a Metallic Magnetic Microcalorimeter

The energy resolution of a metallic magnetic calorimeter is limited by effects such as the noise of the SQUID magnetometer. Here, only the physical rather than the technical limitations of the resolution will be discussed. The dominant physical contribution to the resolution is given by the thermodynamic fluctuation of heat between the main heat capacity subsystems, namely the electron and the Zeeman system, and the thermal bath. Heat is exchanged via thermal links characterised by their thermal conductance G with typical time constants $\tau_i = C_i/G_i$. The characteristic constant τ_1 for the relaxation time to the temperature of the thermal bath is given by equation 2.26, and the constant for the Zeeman system is denoted by τ_0. With this definition, the physical resolution is given by [Flei05]

$$\Delta E_{FWHM} = 2.36\sqrt{8\,k_B\,C_{tot}}\;T\left(\frac{\tau_0}{\tau_1}\right)^{1/4} \tag{2.31}$$

Due to the linear dependence on the temperature T, it becomes clear once more that low operating temperatures are preferable. Also, the ratio τ_0/τ_1 can be tuned to arbitrary values since τ_1 is the thermal coupling between the bath and the absorber, which can be increased by reducing the thermal conductance. If the relaxation time is chosen too long, the count rate of the calorimeter will be significantly reduced, since a new photon can be measured at the earliest when the temperature of the absorber has reached the temperature of the thermal bath. Otherwise a degradation in resolution has to be considered due to pile-up.

To operate the calorimeter in the hard x-ray regime, it is necessary to have an absorber with a sufficiently high photon stopping power. Since the gold used for the absorber is already a high-Z material, the only knob to be tuned is the thickness. However, a thick absorber is linked to a high total heat capacity C_{tot}, which has a negative influence on the energy resolution. In this sense, a similar compromise between resolution and efficiency has to be made, as in section 4.1.1 for the crystal spectrometer.

Another preferable feature of a detector would be to cover a large solid angle to increase the efficiency of the system. If the area of the absorber would be increased, this would also increase the heat capacity, as discussed above. However, an alternative approach to increase the covered area is to use many small pixels instead of one large pixel. The downside of this strategy is the huge number of SQUIDs and electronics necessary to read out such multi-pixel systems. A modern method aiming to avoid this, is to use an rf-multiplexed readout strategy, where many or all pixels are monitored simultaneously by only one SQUID [Kemp14].

With $C_{tot} = 1\,\mathrm{pJ/K}$ and $T = 50\,\mathrm{mK}$, and typical values for the characteristic times $\tau_0 = 1\,\mu\mathrm{s}$ and $\tau_1 = 1\,\mathrm{ms}$, an energy resolution of $\Delta E_{FWHM} \approx 1.5\,\mathrm{eV}$ can be estimated. Experimental values of $\Delta E_{FWHM} = 1.6\,\mathrm{eV}$ at $5.9\,\mathrm{keV}$ primary photon energy have been reported [Kaza14].

2.4 Further Spectroscopic Methods

Besides the two detector concepts for x-ray spectroscopy introduced in the previous two sections, a vast amount of different methods aiming for a precise determination of the atomic structure of heavy highly charged ions has been invented. Not all of these measure the photons which are emitted by the ions, but utilise other observables. In the following, several other successful and precise spectroscopic methods will be briefly discussed.

Semiconductor Detectors

Accelerator-based experiments, measuring the characteristic transition energies with the help of semiconductor detectors, are among the first techniques used to systematically investigate the properties of multiply charged ions. While in the beginning of the 1970s, beam-foil spectroscopy predominated [Bash76], with the advent of ion storage rings, semiconductor detectors have also been used there as the primary x-ray detection systems. Semiconductor detectors possess many preferable features, such as a high detection efficiency $> 80\,\%$ in the hard x-ray regime, a large solid angle coverage, and a good long-term stability. Therefore, they have extensively been used for Lamb shift measurements in highly charged heavy ions. The red data points in figure 2.14 exemplarily show the results for the 1s Lamb shift in hydrogen-like uranium U^{91+} [Stoh93, Beye95a, Beye95b, Stoh00, Gumb05], which could be obtained with semiconductor detectors at the ESR storage ring (for more details concerning the ESR storage ring, see section 3.4). For the sake of completeness, the ochre coloured data points have been obtained with competing methods [Bria90, Lupt94].

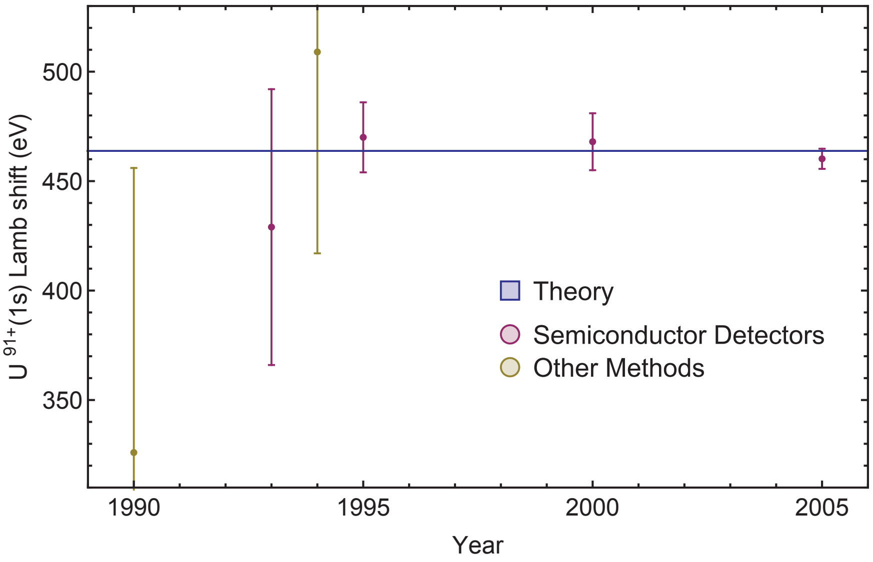

Figure 2.14: Measured values of the 1s Lamb shift in hydrogen-like uranium U^{91+} over the years. The red data points have been obtained with semiconductor detectors [Stoh93, Beye95a, Beye95b, Stoh00, Gumb05], while the ochre coloured ones stem from other methods [Bria90, Lupt94]. The blue line is the prediction from the most recent theory [Yero15].

The experimental findings, achieved with the semiconductor detectors, are in good agreement with the theoretical prediction, represented by the blue horizontal line [Yero15]. The most precise result $E_{\text{1s-LS}}^{\text{U}^{91+}} = 460.2(4.6)\,\text{eV}$ has been obtained by Alexandre Gumberidze *et al.*, in 2005, where about 3 eV of the total uncertainty were due to the limited resolution of the semiconductor detector, and the associated line profile fitting procedure [Gumb05]. Since modern semiconductor detectors have reached their theoretical limit in terms of energy resolution [Fano47], no further improvement can be expected for the future. Therefore, a change to other detection technologies, exhibiting higher resolving powers, has to be conducted. With the crystal spectrometer FOCAL and the microcalorimeter maXs, two possible candidates capable to inherit the semiconductor detectors are presented in this work.

Fluorescence Spectroscopy

The most natural approach to perform high-precision x-ray spectroscopy would be to apply the techniques used in the optical regime, where outstanding relative uncertainties in the order of 4.5×10^{-15} have been reported [Matv13]. A standard experiment assembly consists of a reservoir of a few, or just one, atoms or ions, being at rest, and a frequency-tunable laser beam illuminating them. While changing the well-controlled wavelength of the laser, the intensity of the fluorescence signal from the particles is recorded, and a clear and narrow peak in the spectrum can be found, if a resonance has been crossed with the laser. However, when it comes to x rays, the ion reservoir as well as the laser are much more difficult to realise. Instead of having a simple gas cell containing the atoms to be investigated, the ions require a whole accelerator complex, or at least an electron beam ion trap (EBIT, see chapter 3), to produce and store the desired particles in the charge state of interest. Also, high photon flux sources operating in the (soft) x-ray regime became available only recently [Acke07, Emma10], and first photon-induced fluorescence experiments on iron [Bern12] and krypton [Epp15] have been performed. However, these elements are still in the medium-heavy region, and the measured transition energies are lower than 15 keV. The relative uncertainty reached is no major improvement as compared to competing methods, operating in the same energy regime. Therefore, these investigations should be understood as proof-of-principle experiments. In the near future, the powerful European Free Electron Laser XFEL [Alta06] will start its operation, but also there the maximum energy will be below 25 keV, which is at least a factor of three too low to excite Lyman transitions in the heaviest elements.

Dielectronic Recombination

If an ion with at least one remaining electron is hit by a free electron, the free electron can radiatively recombine (RR) with the ion, and a photon is emitted, with an energy equal to the sum of the kinetic and the binding energy. If the kinetic energy of the free electron matches an excitation energy of the bound electron, in addition to the RR, a second, resonant, recombination channel opens, where the energy excess is not released by emitting a photon, but rather by exciting the bound electron. This process is called *dielectronic recombination* (DR), and can be regarded as the time-inversed realisation of the Auger process. By scanning the collision energy, an enhancement in the electron recombination rate can be observed only for specific kinetic electron energies, which can be identified with excitation energies. Such experiments have been conducted at the ESR storage ring, where the electron cooler was used as an electron beam with a well-defined kinetic energy. In this way, the $2\,s_{1/2} - 2\,p_{1/2}$ energy splitting in lithium-like heavy ions could be measured [Bran03].

Resonant Coherent Excitation

If an ion with at least one remaining bound electron is accelerated to a certain velocity and passes through a crystal, it experiences a periodic change of the electric field strength, generated by the traversed atomic lattice planes in the crystal. This periodicity corresponds to an electromagnetic wave with the same frequency. If this velocity-dependent frequency matches a characteristic transition frequency of the ion, the ion can be excited to the according level. Since lattice plane spacings in a crystal are of the order of x-ray wavelengths, and the achievable velocities are near to the speed of light, transitions in very heavy ions can be driven. By applying this technique to the $2\,s_{1/2} \rightarrow 2\,p_{3/2}$ transition in lithium-like uranium, the level separation of 4.5 keV could be excited, and precisely measured [Naka13]. For the future, it is planned to install such an experiment at an ion storage ring, which would increase the precision to the level of crystal spectrometer measurements [Beie93]. The much higher velocities, which will be available at the FAIR facility (see section 3.5), would also allow to excite $1\,s \rightarrow 2\,p$ transitions in heavy elements.

Chapter 3

The Particle Accelerator Complex at the GSI Helmholtz Centre

In the previous chapter, it has been motivated why it is reasonable to investigate the spectra of highly charged heavy ions with the highest precision. Since matter on earth is electrically neutral under normal conditions, it is necessary to prepare the ions in the desired charge state prior to investigation of their properties. One common method to produce highly charged ions is use of an electron beam ion trap (EBIT), which overlaps a high-energetic electron beam with a trapped, and, at the beginning, lowly charged ion cloud. In this technique, the atomic electrons are removed step-by-step by successive electron impact ionisation. However, the total amount of highest charge states is also in a modern EBIT very poor. At the moment, the only method capable to generate feasible numbers of highly charged heavy ions is an ion accelerator, which brings lowly charged ions to high kinetic energies and passes them through a stripping foil, in which the remaining bound electrons get removed from the atomic nucleus. One of the accelerators capable to do this is located at the GSI Helmholtz Centre in Darmstadt, which will be explained in detailed in the following section.

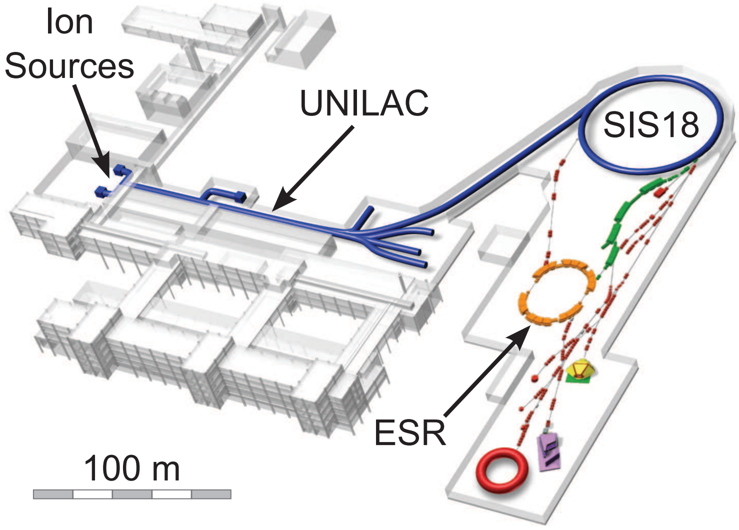

Figure 3.1: Overview of the GSI accelerator complex.

3.1 Ion Source

The task of an ion source is to provide huge amounts of lowly charged ions of interest to the accelerator. These ions are generated from initially neutral atoms, which are supplied to the ion source in the element favoured aggregate state, most commonly gaseous, for elements like krypton or xenon, or solid, like for gold or uranium. Since every element has its own chemical behaviour, there are seven different types of ion sources at GSI to account for that. In this way, almost every element, ranging from hydrogen ($Z = 1$) up to uranium ($Z = 92$), can be offered to the experimenters if required. Up to three ion sources can be operated at the same time, supplying the associated accelerator in turn with different elements. Therefore, three experiments requesting different elements, can run at the same time. If in addition some experiments share the same ion species, the number of beam users is, in principle, just limited by the number of experimental stations available.

In the following, the functionality of the metal vapour vacuum arc (MEVVA) ion source will be described, which provides, amongst other elements, gold ions for the FOCAL experiment. This source consists of an anode and a cathode. The cathode is made of the desired element, and gets heated whereby the metal starts to evaporate. By applying a short high voltage pulse between anode and cathode, an electric arc sparks, and ionises the metal atoms during its way through the gas, turning it into plasma. By this method, not very high charge states can be reached, but in return, quite high numbers of ions can be produced. The ions are extracted by applying an additional electric field, which guides them to the RFQ, the first part of the linear accelerator UNILAC.

3.2 The Linear Accelerator UNILAC

The universal linear accelerator UNILAC and the experimental stations behind it, were the original part of GSI, when it was build in the 1970s. It was mainly used to conduct nuclear-physics experiments, like the generation of new elements, *e.g.* darmstadtium $_{110}$Ds. Nowadays, it is still used for nuclear-physics experiments, but also for material science and as a pre-accelerator for the SIS18 synchrotron. In the near future, when the Facility for Antiproton and Ion Research (FAIR) is running, it will still be used as the pre-accelerator for the whole complex.

The UNILAC consists of three different accelerating sections: The RFQ, followed by the IH and finally the Alvarez tanks. The first section starts right after the ion source, which is a radio frequency quadrupole (RFQ). Its task is to bunch and further accelerate the beam from the source. Bunching transforms the continuous cw beam from the source into a pulsed one, since linear accelerator like the UNILAC, accelerate charged particles by applying a radio-frequency high voltage (rf) on them. Due to a periodically changing polarity of the rf, this would result in a beam, where just a small fraction of the cw current, which is in phase with the rf, is accelerated, the rest would be decelerated and finally lost. The bunched ion beam is then fed into the interdigital-H-mode (IH) accelerating structure, which increases the kinetic ion beam energy from 120 keV/nucleon (hereafter referred to as keV/u) to 1.4 MeV/u. Its design is a long cylindrical microwave cavity, into which a standing wave rf with a frequency of 36 MHz is coupled. In addition, focusing elements and drift tubes, in which the ion bunch can "hide" if the rf has the opposite polarity, are housed. After the IH, a gas-stripper is situated, in which the still very lowly charged ions, *e.g.* 4+ for the design ion uranium, are further ionised (normally up to U^{28+}), which makes the subsequent acceleration in the Alvarez tanks more efficient. The Alvarez is in its design similar to the IH, the main difference is that it operates in a different rf mode (TM_{01} instead of an H-mode), and the focusing elements are build inside the drift tubes. The Alvarez is run at an rf frequency of 108 MHz, and the beam leaving it has a final kinetic energy of 11.4 MeV/u. This beam is now available for the experimenters at the low energy caves X, Y and Z, or can be guided through the transfer channel (TK) to the heavy ion synchrotron SIS18. In the transfer channel, the ions get further ionised by a solid state stripping-foil. The kinetic energy is not yet high enough to provide fully ionised heavy ions, therefore, the usual charge state is 73+ for uranium.

3.3 The Heavy Ion Synchrotron SIS18

The heavy ion synchrotron SIS18 and the subsequent experimental facilities were build in the end of the 1980s, as GSI's first expansion stage, to provide higher beam energies of up to 1 GeV/u at an intensity of 4×10^9 uranium ions per spill [Blas89, Bhne90, Omet06]. Besides the atomic physics division, also the nuclear, particle and biophysics groups are heavily demanding beams for their studies.

For example, the fragment separator (FRS) is used to generate new isotopes of known elements, to investigate their masses, half-lifes, the location of the neutron drip line and other properties. In total over 440 new isotopes could be produced for the first time at GSI [Thoe16]. The masses are determined in the experiment storage ring (ESR, see section 3.4) in either the Schottky- or isochronous mode, with the latter one being fast enough to measure even radioactive fast-decaying isotopes [Litv05, Haus00].

With the Hades experiment, dense nuclear matter can be generated to investigate the properties of in-medium baryons. These research activities aim to map the QCD phase diagram in the direction of high baryon density, which is complementary to the studies done at the ALICE experiment at the LHC.

Most of the work done by the biophysics division is carried out in the M-Cave, where the heavy ion cancer therapy was developed, taking advantage of the fact that charged particles passing through matter release the most of their energy shortly before they stop completely. This *Bragg-peak* called effect is used to conserve healthy tissue, while damaging the cancer cells irreparably. Nowadays, this GSI invention is used in dedicated cancer treatment centres in Heidelberg, Marburg and also some other countries all over the world.

The atomic physics group profits the most from the higher energies of the ions, which is high enough to completely strip off all remaining electrons, even for the heaviest ion species like uranium. The technique applied is again a stripping foil and a subsequent magnetic separator, which splits up the different charge states spatially. Figure 3.2 shows a fluorescent screen picture of a 300 MeV/u U^{73+} beam passing through a 100 mg/cm^2 aluminium stripping foil, after a dipole magnet for charge state separation [Gass12].

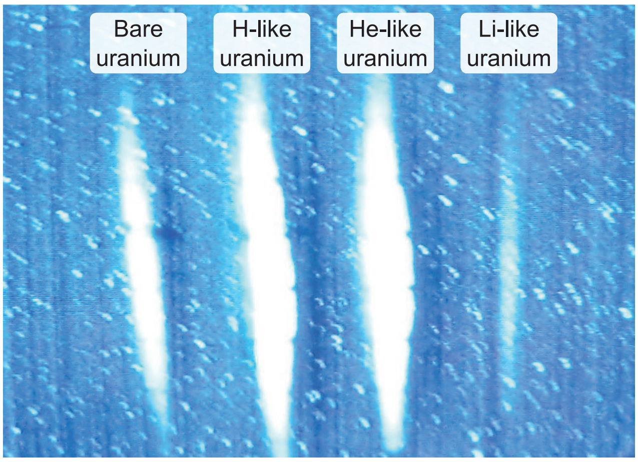

Figure 3.2: Fluorescence screen picture of an originally U^{73+} beam at a kinetic energy of 300 MeV/u after passing through a 100 mg/cm^2 aluminium stripping-foil, and a dipole magnet for charge state separation. The parameters were selected in such a way, to optimise the yield of H-like uranium [Gass12].

For this picture, all parameters were tuned in a way to maximise the yield of H-like uranium, which was in this case about 44 % of the primary beam intensity. By positioning a mechanical slit at the location of the desired charge state, all the unwanted ions can be removed, resulting in clean conditions for the experiment. The expected charge state distribution can be calculated by computer codes, like CHARGE or GLOBAL [Sche98], or by using the rule-of-thumb Bohr criteria, which states that the ion should have at least the velocity of the K-shell electron $v_{ion} \approx v_{1s}$, to be ionised efficiently. Formula 2.4 yields for uranium $v_K \approx 0.67\,c$, which corresponds to an energy of 326 MeV/u, which is compatible with figure 3.2 for a 300 MeV/u beam, where bare uranium could already be observed.

The '18' in the name of SIS18 stands for the maximum magnetic rigidity of the synchrotron, which is defined as the product of the ion beam bending radius of the dipole magnets $\rho = 10\,\text{m}$, and the maximum magnetic field strength $B_{\text{max}} = 1.8\,\text{T}$. By the simple formula

$$B\rho = \frac{m}{q}\gamma\, v \tag{3.1}$$

the maximum velocity v, and, therefore, the energy of a stored ion beam can be calculated, depending only on the mass-to-charge ratio m/q, while the Lorentz-factor γ accounts for relativistic velocities.

The SIS18 has a circumference of 216.72 m, which is established by 24 dipole magnets. Since dipole magnets are just used to force the circulating beam onto a closed orbit, all the other important instruments are installed in the straight sections in between. There is a large number of beam focusing quadrupole and sextupole magnets, two rf-cavities for acceleration, vacuum pumps, beam position monitors, other beam diagnostics and the SIS18 electron cooler, which will be explained in detail in section 3.4.1.

Due to the fast ramping rate of the dipole magnets, of 10 T/s, the whole acceleration is done in less than 100 ms. Typically, a beam below 1 GeV/u is provided through the transfer beam line, which contains the last stripping foil, to the different experimental station mention before. One of the most important machines for the atomic physics division which was also used for the experiments presented in this work is the experiment storage ring ESR.

3.4 The Experiment Storage Ring ESR

The experiment storage ring ESR is a very flexible machine, being used for many atomic- but also nuclear physics experiments. Its main task is to store and cool the ion beam coming from the SIS18, and to provide the experimenters with an infrastructure to enable versatile experimental possibilities. It was built together with the SIS18, and the other experiment station, in the target hall, in the 1990s, as a fully functioning synchrotron, offering the same features as the SIS18, just with half the circumference, and a maximum magnetic rigidity of $B\rho = 10\,\mathrm{Tm}$. Therefore, the maximum beam energy for U^{92+} is 560 MeV/u. The elongated hexagonal shape is established by six dipole magnets, which are connected by four short, and two long straight sections. The short sections are filled with machine equipment similar to the SIS18, whereas the long sections are used by the experimenters to conduct the experiments. These straight sections host the ESR electron cooler and the internal gas-jet target, and can be reconstructed if required by the experiment. Besides the injection from the SIS18, there is also the possibility to extract the beam to other experiments in the target hall, or the HITRAP facility, which is currently under commissioning. It will finally allow to decelerate a large amount of highly charged ions, basically to rest [Herf15]. In the following two sections, the important functions of the ESR will be introduced, in greater detail.

3.4.1 Ion Beam Cooling Methods

To investigate an effect with highest possible precision, it is desirable to have the system to study in well-defined starting conditions before manipulating it. If the system consists of many particles, like an ion beam, it would be preferable that all of them fly in the same direction at the same velocity v_0. This *ensemble of ions* can be

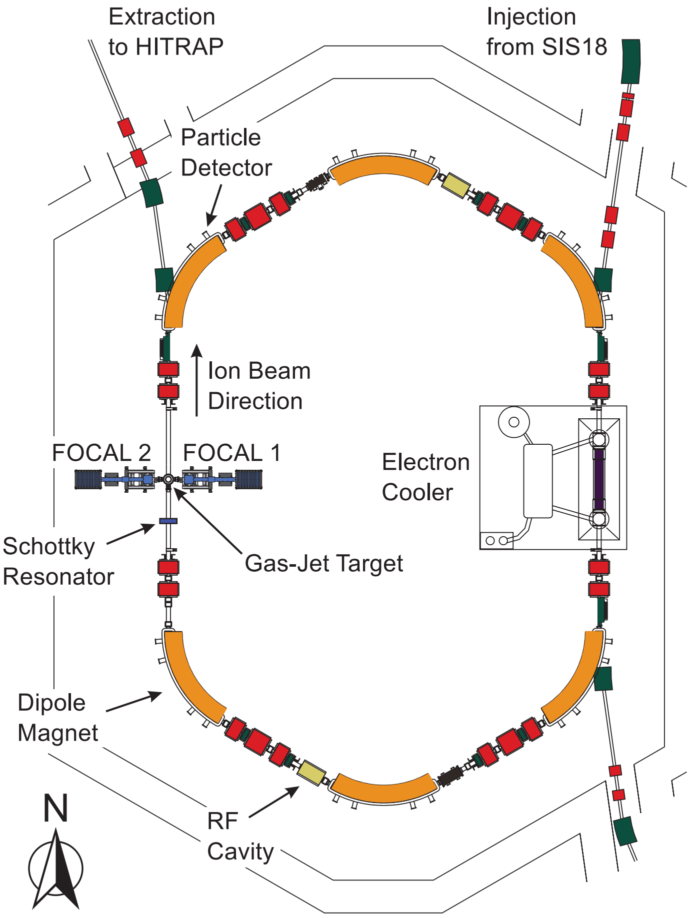

Figure 3.3: Schematic top view of the experiment storage ring ESR. The ions are injected by the SIS18 from the top right beam line. They are forced to circle the ring due to the six dipole magnets (orange), and focused by quadrupole lenses (red). The electron cooler, on the long section on the right, cools the ion beam, while the FOCAL experiment (blue) is conducted at the gas-jet target, on the left straight section. A particle detector, to detect down charged ions, is installed at the top left bending magnet.

characterised by a temperature T which is given by

$$\frac{1}{2} N_{dof}\, k_B\, T = \frac{1}{2} m \left\langle (v - v_0)^2 \right\rangle \tag{3.2}$$

with the Boltzmann constant k_B, the ion mass m and the number of degrees of freedom N_{dof}. For a normal gas at rest, *e.g.* in a gas cell, it is $v_0 = 0$, however for an ion beam moving at relativistic velocities this directed movement has to be subtracted, since just the unordered motion relative to the centre of mass contribute to the temperature. If a monoenergetic beam is desired, the velocity spread and, hence the temperature, has to be reduced, which explains why this procedure is called *ion beam cooling*. Beam cooling is necessary to counteract heating effects, like the beam interaction with a stripping foil or a gas target, and the so called intra-beam scattering, which is caused by the Coulomb interaction amongst charged ions.

To achieve beam cooling, different methods have been developed in the past, three of which are used at the ESR [Fran90]. The first cooling method is called *stochastic cooling* (SC), which records the position deviation of a passing ion from its design trajectory, by means of a pick-up electrode. The signal is amplified and fed to a kicker electrode, which applies a correction on the ion position. Since the pick-up and the kicker electrodes are spatially separated it is of crucial importance that the correction signal is applied to the measured ions and not to different ones. Therefore, a fixed phase relation between these two positions is necessary. In the ESR, this is achieved by an ion beam, having the constant kinetic energy of 400 MeV/u. The SC works always on a large number of ions, which is why some of the misplaced ions get corrected, but also some of the aligned ions get out of place. However, due to the continuous appliance to the circulating beam a net cooling effect can be observed, this is the reason why it is called *stochastic* cooling. The advantage of the stochastic cooling is the short cooling time in the order of about one second. The main disadvantage is the already mentioned fixed working velocity of the beam, which restricts the flexibility for the experimenter.

The second standard cooling technique applied at the ESR is *electron cooling* (EC). For that method, an intense electron beam is accelerated in the electro-static gun of the electron cooler, see figure 3.4. The value of the accelerating voltage defines the velocity of the electrons, which should be chosen such, that it coincides with the mean velocity of the ion beam. The temperature of the fast electron beam is far less than 1 eV, hence it is called *cold*. After acceleration, the electron beam gets bent by a weak magnetic field, which results in an overlapping between the ion and the electron beam. The weak magnetic bending field will almost not influence the ions due their much higher mass-to-charge ratio, according to equation 3.1.

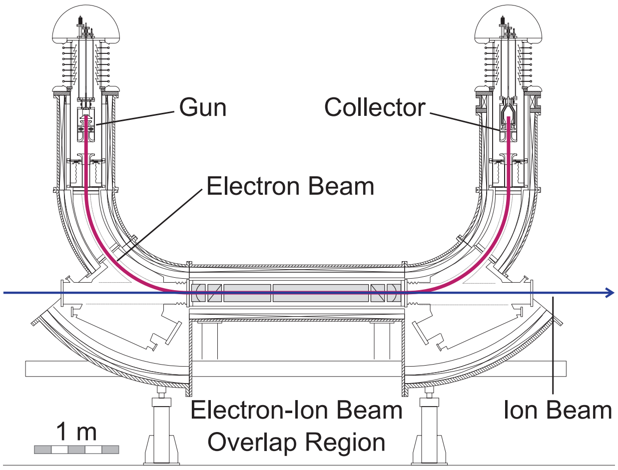

Figure 3.4: Sectional view of the electron cooler. The ion beam passes from the left to the right. The cold electrons are produced in the gun, where they get accelerated by a high voltage. In the overlap region, the ions and electron exchange heat, and in the collector the remaining electrons are dumped.

In the 2.5 m long overlap section, where the two beams can freely co-propagate, heat can be exchanged from the hot ions to the cold electrons. This is understood best in the rest frame of the cold electrons, which have a relative speed $v_{rel} \approx 0$ in respect to each other. Ions which are faster than the electrons lose energy through Coulomb scattering until their speed coincides. Ions which are slower gain energy by the faster passing electrons. Following the interaction region, the electrons are again bent by a magnet and dumped in a collector. A parasitic effect in this cooling method is radiative recombination (RR, [Eich07]), where a free electron recombines to a bound state of an ion, which results in a down-charged ion that is not available for further investigations any more. The total cross section for RR scales like

$$\sigma_{RR} \propto \frac{Z^5}{E_{rel}^{7/2}} \tag{3.3}$$

with Z being the nuclear charge of the ion and E_{rel} the relative kinetic energy between the ion and the electron [Eich07]. For a perfect cooled ion beam, which means vanishing E_{rel}, the cross section goes to infinity and all the ions would be gone. This is understandable, since zero relative speed would result in an infinite long interaction time, which would sooner or later lead to recombination. There are two reasons why even a cold beam is not lost immediately. Firstly, the interaction time per pass is of the order of $10^{-8}\,s$, which is certainly shorter than forever. Secondly, the temperature achieved after long cooling will never reach $E_{rel} = 0$ since the electron beam has a finite temperature, and, in addition, the energy loss of an ion penetrating the electron cloud per unit length scales like

$$\frac{\mathrm{d}E}{\mathrm{d}x} \propto \begin{cases} v_{rel} & \text{slow } v_{rel} \\ v_{rel}^{-2} & \text{fast } v_{rel} \end{cases} \tag{3.4}$$

which makes beam cooling more and more inefficient if slow relative velocities v_{rel} are acquired. Since $\mathrm{d}E/\mathrm{d}x$ has the dimension of a force, it is often referred to as *cooling force*. The lifetime of a U^{92+} beam with permanently running electron cooler is of the order of 100 s, which for the most experiments is much longer than the lifetime due to the interaction with the running internal gas-jet target. In addition, there is also a number of experiments which use the electron cooler as a dedicated electron target, which serves as a truly free-electron target [Beye94, Gumb05] or allows to introduce small relative velocities for dielectronic recombination studies [Bran03]. The main advantage of electron cooling is the great flexibility in the choice of ion beam energy.

Figure 3.5 illustrates the effect of electron cooling with the help of the so-called *Schottky resonator*. The Schottky resonator is capable of Fourier transforming the ion beam current from the time into the frequency domain [Nold11]. The fraction of the ions which is slower than the average ion, can be found at lower (revolution) frequencies, whereas faster ions can be found at higher frequencies. The signal strength scales with the number of ion in the according velocity class. Due to technical reasons the recorded frequency is an integer multiple of the ion beam revolution frequency. Shortly after injection from the SIS18, the uncooled ion beam shows a broad frequency and hence momentum distribution (blue curve in figure 3.5). After several seconds of electron cooling the broad distribution became narrower (red curve in figure 3.5), which can be identified with a cooled ion beam.

The last cooling technique applied at the ESR is *laser cooling*. It is closely related to the well-established laser cooling of neutral atoms [Phil98], but due to the relativistic velocities some additional difficulties arise. To cool a neutral gas at rest, an optical transition with the wavelength λ and a high spontaneous transition rate A_{21} has to be selected. If a laser with a slightly longer wavelength $\lambda_L > \lambda$ is superimposed, only atoms which are heading towards the laser, with the velocity v, are in resonance with the light, due Doppler-shift which shortens the wavelength in the rest frame of the

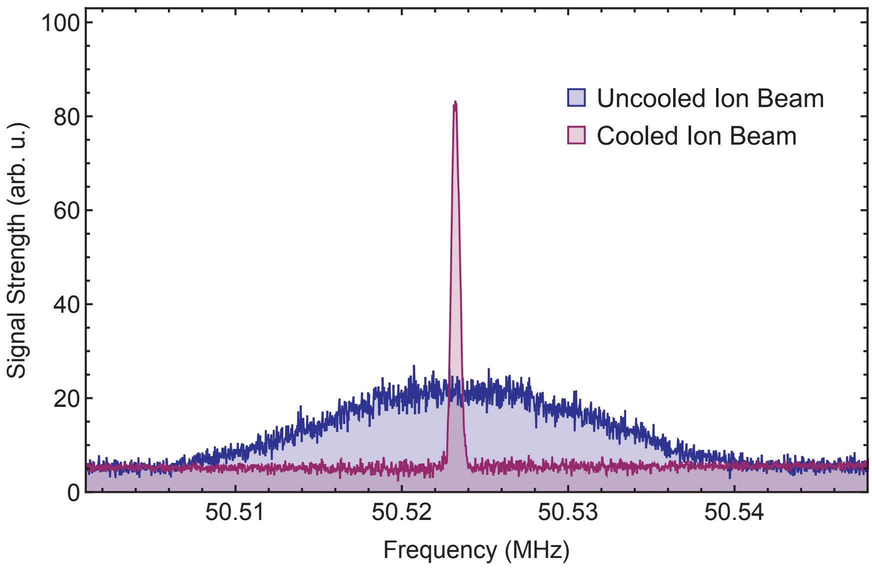

Figure 3.5: Histogram of ions with a certain velocity distribution over an integer multiple of the ion beam revolution frequency. The broad blue distribution corresponds to an uncooled beam right after the injection from the SIS18 whereas the red peaking curve represents the ion beam after several seconds of electron cooling. The picture has been generated with data from [Bran00].

moving atom $\lambda \overset{!}{=} \lambda'_L = \sqrt{(c-v)/(c+v)}\,\lambda_L$. The atom absorbs a photon from the laser and re-emits it in a random direction. After this process, it is again ready to absorb another photon from the laser and to re-emit it again. This forms a cyclic process which happens very often due to the high selected transition rate A_{21}, and, as a consequence, the velocity of the atom is reduced, due to the incorporated momentum $p = h/\lambda$ of the photons. The momentum vectors of the photons point all in the same direction, therefore, the atom is slowed down in this direction. The re-emitting of the photon occurs in a random direction, which averages out after several cycles. The whole procedure continues until the atom has changed its velocity in such a way that it is no longer in resonance with the laser. In a real setup, a mirror is used to reflect the laser, which then counter-propagates its initial direction. This will also force the atoms which move in the opposite direction to be slowed down as well, resulting in a cold gas in one dimension. By utilising three counter-propagating laser beams, which are aligned perpendicular to each other, all three spatial dimensions of the gas are cooled.

Laser cooling at a storage ring is normally done just in one (the longitudinal) direction, and encounters the additional difficulty of relativistic moving ions. Since the laser has to be red-detuned in the rest frame of the moving ion bunch, the laboratory wavelength for the co- and counter-propagating laser beams have to be different, due to the additional Doppler-shift of the fast moving ion beam. For a gas at rest, where a simple mirror to reflect the laser can be used, one rather has to build two dedicated laser systems with quite different wavelength. Often, the wavelength for the counter-propagating laser lies in the infrared, and for the co-propagating beam in the far ultra violet, which makes them difficult to handle. Although these difficulties exist, its feasibility has been demonstrated at the ESR storage ring, and it is planned to install this technique as a permanent infrastructure at the SIS100 synchrotron, at the Facility for Antiproton and Ion Research (FAIR) [Wint15].

3.4.2 The Internal Gas-Jet Target

Many of the experiments performed at the ESR study the (radiative) electron capture (R)EC or x-ray transitions followed by an electron capture/recombination process. One way to provide the electrons to be captured is to use the electron cooler as a target (see previous section), or the dedicated gas-jet target, which is entirely build for this purpose and will be explained in detail in this section [Krme01, Khne09, Petr14].

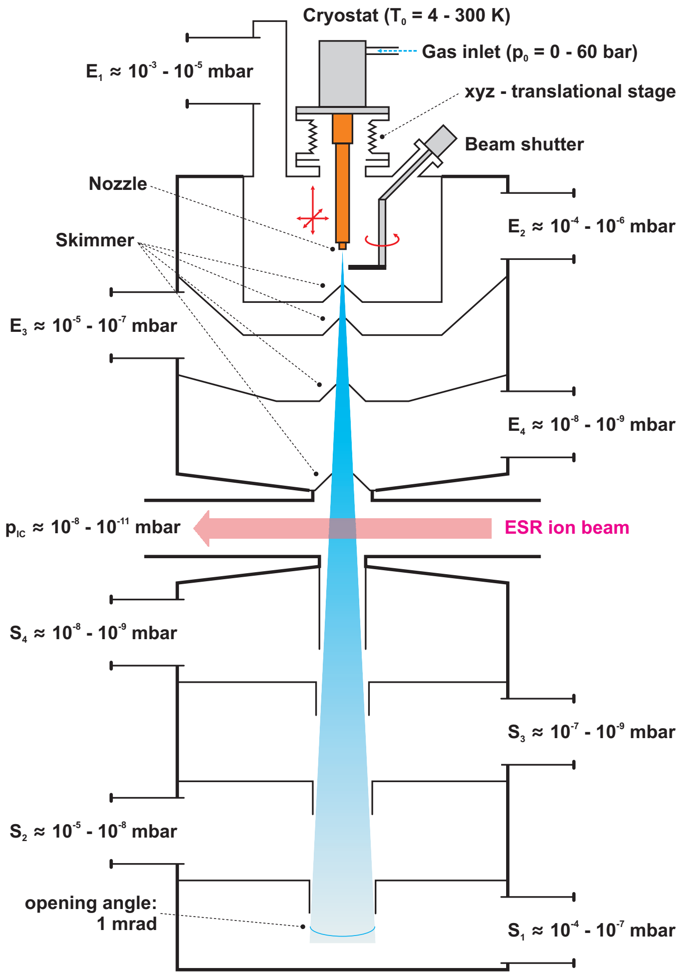

Figure 3.6: Sectional view of the internal ESR gas-jet target. The Laval nozzle is located at the tip of the cryostat and permits a pre-cooling of the target gas, if needed. After leaving the nozzle, the gas expands freely into the vacuum of the inlet chamber, which is divided by several round skimmers in a differential pumping station. In the ESR target chamber, the ion beam overlaps with the gas-jet, where the ions may capture atomic electrons from the target gas. The gas-jet is disposed in the gas dump chamber, which is also a differential pumping station. The picture has been taken from [Petr14].

The main purpose of the gas-jet target is to provide the electrons, bound in the shells of the neutral atoms, to the passing highly charged ions. The greatest challenge is hereby to maintain the ultra-high vacuum (UHV) of around 10^{-10} mbar in the ESR, and, at the same time, generate sufficiently high particle area densities, of the order of 10^{12} particles/cm^2, so that the EC rate becomes significant. Another demand, from the experimenters, is the possibility to use different target gases, since there is not only one gas type which meets all requirements. The design of the current ESR gas target is shown in the side-view figure 3.6. The gas enters the target at the top, with a normal operating pressure of around 20 bar. Depending on the gas type and the desired density, a cryostat is installed to cool the gas, which is often done for H_2 or He gas, but rather rarely for heavy gases like Ar, Kr or Xe. After the cryostat, the gas expands through a trumpet shaped Laval-nozzle into vacuum. The internal heat energy of the gas is thereby almost completely converted to directed kinetic energy of the atoms (or molecules), which gain super-sonic velocities. Since they depart from each other faster than the speed of sound, they cannot scatter with each other. Therefore, they fly on a straight path. The volume, where no sound is propagated, is also called the “zone of silence”. The nozzle is followed by four round skimmers, which shape the gas jet and separate the four differential inlet pumping stations E1 – E4. The pump stations are equipped with a turbo molecular pump each, to maintain the UHV of the ESR. After the last skimmer, the gas jet flies freely through the ESR target chamber, where it may interact with the ion beam and is finally disposed in the gas dump system S1 – S4, which is also a four-stage differential pump station. The target area density can be calculated by measuring the pressure rise in the beam dump system, since the pumping speed and the velocity of the gas jet is known. Within the scope of the evaluation of systematic uncertainties also the properties of the gas-jet target were examined. The results from this investigation can be found in section 5.2.2.

3.5 Outlook for the FAIR Project

Currently, the GSI Helmholtz Centre is extended by additional accelerators, storage rings and experiment caves in the framework of the international Facility for Antiproton and Ion Research project FAIR [FAIR01]. The blue parts in figure 3.7 show the current GSI facility, while the red parts have to be designed and constructed from scratch. FAIR is currently in the civil construction phase, and the first beam is expected for 2018, whereas the complete facility is scheduled to be fully operational in 2022. The main accelerator will be the superconducting SIS100 synchrotron, which uses the SIS18 as a pre-accelerator. With its magnetic rigidity of 100 Tm it will exceed the accelerating capabilities of the SIS18 by a factor of 5.6, and will at the same time offer an unprecedented beam intensity of up to 10^{12} uranium ions per spill [Spil06]. Due to a special linear proton accelerator (p-Linac), it will be possible to accelerate 2×10^{13} protons to a maximum energy of 29 GeV, which is high enough to produce antiprotons at the antiproton separator target [Doli11]. This particle beam can then be collected and cooled in the CR/RESR storage rings, and guided to different stations, where experiments can be conducted. From the atomic physics divisions point of view there will be several experiment stations which are of special interest [Sthl15a, Auma10].

In the APPA cave, fixed-target single-pass experiments at highly relativistic energies can be performed. One example has already been introduced in section 2.4, namely the resonant coherent excitation (RCE) method on highly-charged heavy ions [Naka13]. Another class of experiments are the beam-foil spectroscopic investigations like the lifetime measurement of metastable states [Reus13, Gass12].

The already existing ESR storage ring can store uranium ion beams in the energy range 3 − 560 MeV/u, for higher energies the HESR will be available [Sthl15b]. It has a magnetic rigidity of 50 Tm and can store a U^{92+} beam at kinetic energies up to 4.9 GeV/u. At such high velocities certain experiments will be possible, *e.g.* the test of special relativity in the highly-relativistic regime [Bote14].

For the energy region below the ESR specification, the CRYRING will be available [FAIR11, Lest12, Lest15]. With its lowest stable magnetic rigidity of 0.054 Tm it can decelerate an U^{92+} ion beam below 100 keV/u, which is especially interesting for high-precision experiments, due to the low relativistic Doppler shifts (see also section 6.2). The layout of the CRYRING is very similar to the ESR, it possesses an accelerating/decelerating rf, a gas target station and an electron cooler. Due to its smaller dimensions, the electron cooler is available as a free-electron source for recombination experiments, also for bulky detectors like the microcalorimeter, as will be discussed in section 6.3.

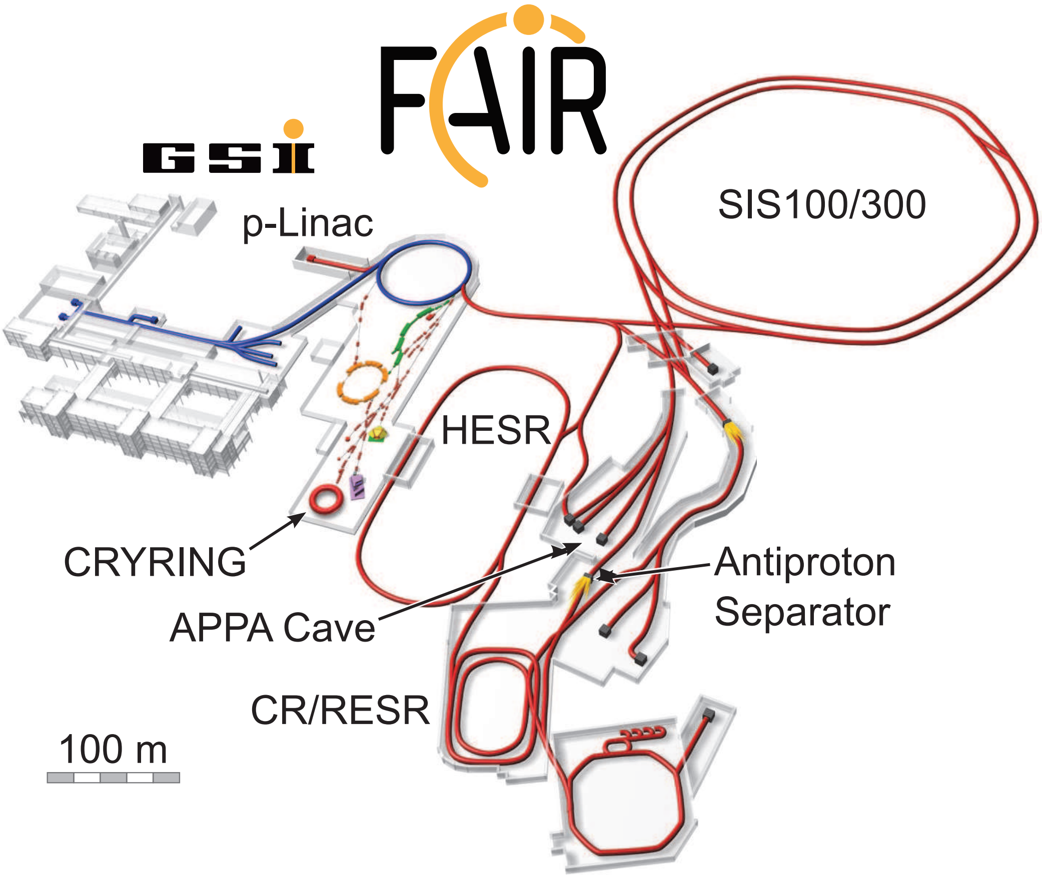

Figure 3.7: Overview of the current GSI Helmholtz Centre (blue), and the future extension of the accelerator complex (red) due to the FAIR project.

Chapter 4

Experiment Assembly and Measurement

The FOCAL experiment is a twin-crystal x-ray spectrometer dedicated to measure the characteristic transitions of highly charged ions circulating in a storage ring with a precision, exceeding that of semiconductor detectors. First design considerations have been made by the head of the FOCAL collaboration, Dr. Heinrich F. Beyer [Beye97a] in 1997, leading to an ongoing development of the instrumentation up to now [Beye15]. FOCAL is the result of a well-balanced trade-off between a high resolving power, which is needed to outperform semiconductor detectors, and the inherently low efficiency of crystal spectrometers, allowing to use such a device on low-luminous x-ray sources like storage rings.

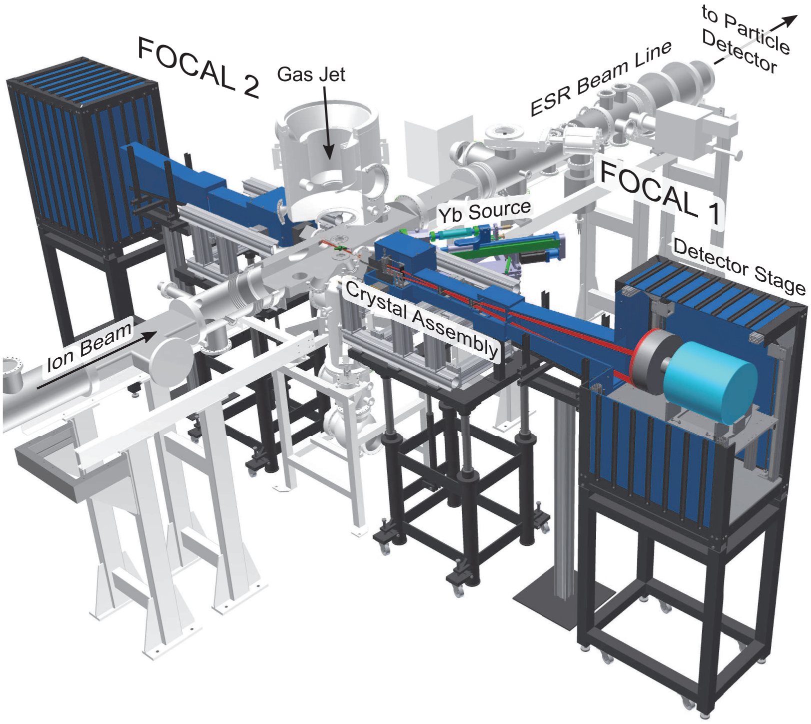

Figure 4.1: Overview of the twin-crystal spectrometer FOCAL (blue) at the internal gas-jet target of the ESR storage ring (grey).

4.1 The FOCAL Experiment

The main FOCAL components consist of the two identical crystal spectrometer arms on opposing observation ports at the ESR gas-jet target, as depicted in figure 4.1. The reason for using two spectrometers is *not* to increase the detection efficiency by a factor of two, but rather to make use of the Doppler-effect-cancelling nature of this special setup. The Doppler effect transforms the rest-frame wavelength λ_0 of a fast-moving source, in dependence of velocity and observation angle θ, into a laboratory-frame wavelength λ_{Lab}, which is given by the well-known formula

$$\lambda_{\mathrm{Lab}} = \lambda_0 \, \gamma \, (1 - \beta \, \cos(\theta)) \tag{4.1}$$

where β and γ are the velocity in units of the speed of light and the Lorentz-factor, respectively. From this formula it immediately follows that the observation angle has to be measured with comparable precision as the wavelength, in order to be able to infer the rest frame wavelength from the laboratory wavelength. This would be a challenging task, since an angle deviation of just 1° would shift the Doppler-corrected energy of the Lyman-α_1 transition of Au^{78+} by almost 600 eV (at $\beta = 0.47$), which is huge compared to the envisaged uncertainty of less than 10 eV. By aligning two identical spectrometers on both sides of the gas-jet target in an opposing manner (see figure 4.2), a full Doppler-effect cancellation is achieved, since each angle deviation of $\theta + \varepsilon$ for one spectrometer arm is compensated by an inverse deviation of $180° - (\theta + \varepsilon)$ for the other arm. Putting these angles into the Doppler formula yields

$$\lambda_1 + \lambda_2 = 2 \, \gamma \, \lambda_0 \tag{4.2}$$

where $\lambda_{1,2}$ are the wavelengths measured by the two arms. The important aspect of this expression is, that it is independent from the observation angle θ. In the general case, it is to be expected that the measured wavelengths do *not* coincide with each other, but that the hence averaged wavelengths give the “true” rest-frame wavelength λ_0 of the transition.

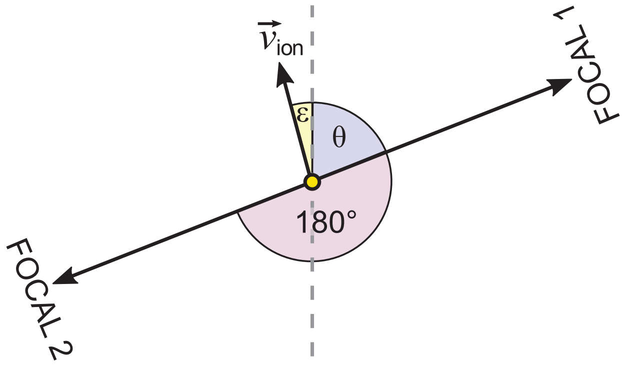

Figure 4.2: Spectroscopic setup for an intrinsically Doppler-effect-cancelling measurement scheme. Two x-ray detectors and the moving source are located on one common line of sight. By utilising equation 4.2 the actual observation angle θ has not to be known.

In figure 4.3 one of the two arms is shown. The part on the very right is the target chamber of the ESR storage ring, which hosts either the ^{169}Yb source, which

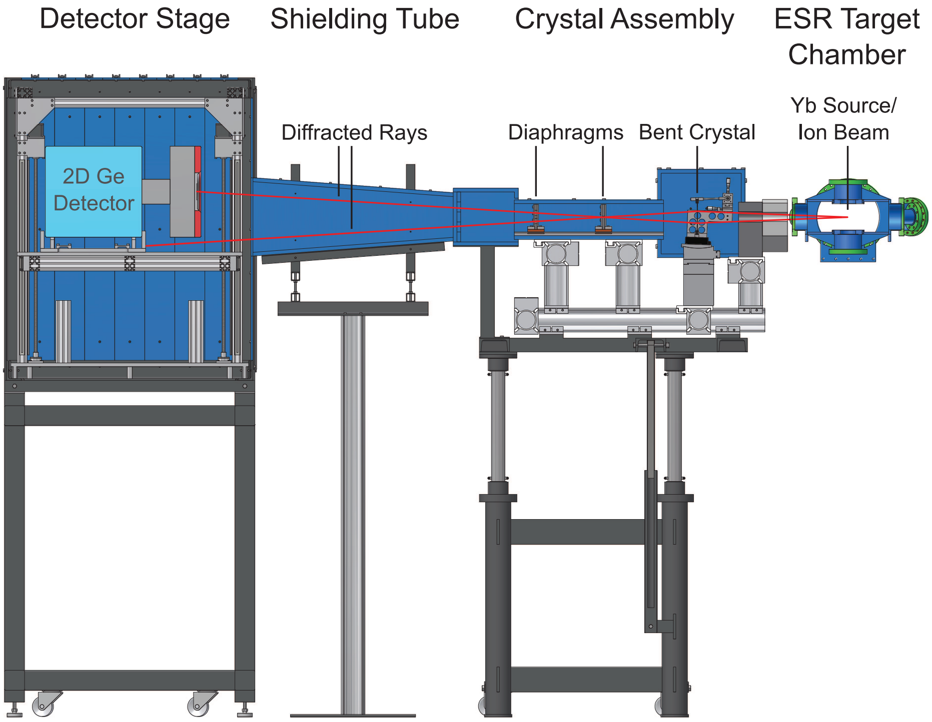

Figure 4.3: Sectional view of one of the two identical FOCAL spectrometer arms. The x-ray source is located in the ESR target chamber, on the very right, emitting radiation in the direction of the bent crystal. These x rays (red lines) get diffracted if they include the Bragg angle with the crystal and hit the 2D position-sensitive germanium detector in the movable detector stage. The whole spectrometer is shielded by several tungsten diaphragms and lead plates (blue) to suppress the strong background.

is used for calibrating the FOCAL spectrometers, or the ion beam, which interacts with the gas-jet target. Characteristic x rays from the stored ions are produced by an electron capture from the target gas atoms, and subsequent transitions to the ground state of the hydrogen-like ion. The part joining on the left is the crystal assembly of FOCAL, which houses the bent crystal (for a more detail discussion see section 4.1.1). Due to the bent, a photon hitting the crystal can fulfil the Bragg condition in two areas, one above and another below the optical axis (red lines). The crystal is followed by two diaphragms made of a tungsten alloy to shield the detector from unwanted radiation that does not stem from a diffraction process in the crystal. The first diaphragm has just a single slit in the centre and is placed at the polychromatic focus of the spectrometer. A few centimetres behind the first diaphragm a second one follows, which has two slits, one for the upper and one for the lower diffracted ray. After the crystal-assembly part of FOCAL, the rays propagate through a shielding tube before finally entering the detector stage. There, the 2D position-sensitive semiconductor detector is located which is used to determine the position of the diffracted photon lines (for a more detail discussion see section 4.1.2). The detector is placed on a movable platform which can be changed in height, in order to cover different (wavelength-)regions on the Rowland circle. For this purpose, on each of the four corners of the platform a high-precision stepping motor with a lead screw is mounted. If a change in height is required, all four motors move synchronously until the desired height is reached. The position of each stepping motor is monitored by a linear encoder with a precision of 1.5 μm per metre. Scans with the platform are exclusively conducted before and after the actual beam time for different test measurements. During the production run, the motors are blocked by means of breaks to avoid any unwanted movement. Since the upper and lower diffracted waves are equivalent, the experimenter can choose the ray path to be recorded. For the production run in 2012, the lower ray path was recorded by FOCAL 1 (in the inside of the ESR), and FOCAL 2 recorded the upper one (outside the ESR, see figure 3.3). The whole setup is passively shielded by 15 mm thick lead plates (dark blue parts) to reduce the unwanted background to a minimum. This measure is absolutely necessary due to the very low counting rate of just about three photons of interest per hour of beam time.

4.1.1 The FOCAL Crystals

FOCAL is a twin-crystal spectrometer operating in a modified Cauchois geometry, which has already been introduced in section 2.2.6. Here, the actual technical realisation of the two identical FOCAL crystals will be discussed. A scheme of the FOCAL crystal optics can be seen in figure 4.4.

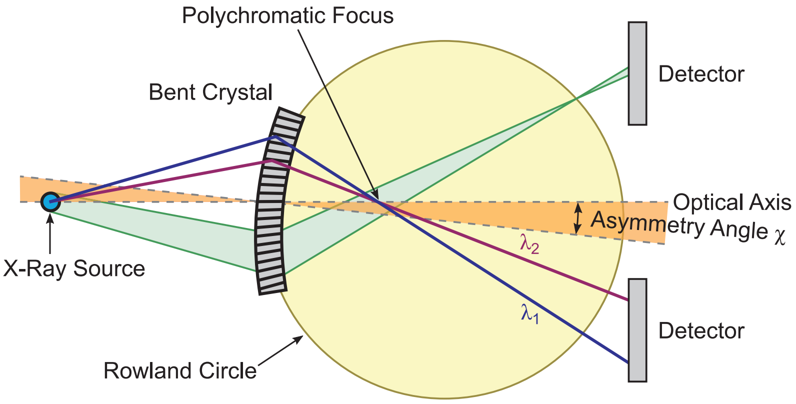

Figure 4.4: Actual crystal optics layout of the FOCAL spectrometer. It is similar to the scheme shown in figure 2.11, but the crystal is rotated by the asymmetry angle χ to generate symmetric, but mirrored spectra above and below the optical axis.

The x-ray source, which is either the Yb-calibration source (see section 4.1.4 for a more detailed discussion) or the fast-moving ion beam hitting the gas-jet target, is located on the very left. On the right hand side of the source the crystal follows, which consists of a silicon single crystal with the dimension $120 \times 40\,\text{mm}^2$ and a thickness of 1.5 mm (see table 4.1 for a comprehensive list of the crystal specifications). The (220) lattice planes are used for diffraction and deviate by an angle of $\chi = 2°$ from the symmetric Laue case. The crystal is bent by a dedicated bending device to a bending radius of $R = 2\,000\,\text{mm}$. The asymmetry angle in combination with the bending broadens the rocking curve, as already stated in section 2.2.4, which will increase the efficiency by a factor of about 25 (shown in figure 2.9 for the FOCAL crystal parameters), to a total efficiency of about 3×10^{-8} which can be calculated from the geometrical dimensions and the rocking-curve properties.

Property	Label	Value
Crystal Material & Reflective Plane		Silicon (220)
Lattice Plane Spacing	d_{220}	$192.015\,571\,4(32) \times 10^{-12}\,\mathrm{m}$
Crystal Dimensions		$140 \times 40\,\mathrm{mm}^2$, $t = 1.5\,\mathrm{mm}$
Asymmetry Angle	χ	$2°$
Bending Radius	R	$2\,000\,\mathrm{mm}$
Source–Crystal Separation	d_{SC}	$600\,\mathrm{mm}$
Primary Calibration Line		^{169}Yb-γ
Calibration Energy		$63\,120.44(4)\,\mathrm{eV}$
Bragg Angle	θ_B	$2.93°$
Rocking Curve		Height: 0.92, Width: $50\,\mu$rad
Reflection Height on Crystal		$\pm\,23.6\,\mathrm{mm}$
Registration Height on Detector	z_d	$\pm\,102.3\,\mathrm{mm}$
Line Width on Detector		$100\,\mu\mathrm{m}$ (Corresponds to $60\,\mathrm{eV}$)
Crystal Efficiency		3×10^{-8}

Table 4.1: Specifications of the FOCAL crystal optics layout [Beye15].

These crystal parameters have been chosen after conducting an optimisation procedure, with the goal to increase the crystal efficiency compared to the flat Laue case (section 2.2.3) as much as possible, without trading in too much of the resolving power, at x-ray energies predetermined by the Lyman-α radiation of heavy elements ($E_{\mathrm{Lab}} \approx 60\,\mathrm{keV}$). This issue can be illustrated best with figure 4.5 which shows the FWHM of the rocking curve as a function of the integrated reflectivity. The red dot indicates the selected parameter and is approximately located where the curve starts to leaves its linear behaviour, leading to a disproportionate growth of the FWHM compared to the gain in reflectivity. From figure 4.5 the following approximate relation can be derived

$$\frac{\Delta\theta}{R_{int}} \gtrsim 1.1 \tag{4.3}$$

linking the FHWM $\Delta\theta$ of the rocking curve to the integrated reflectivity R_{int}, both to be measured in μrad. This relation once more illustrates that it is impossible to optimise both parameters at the same time with the current FOCAL design. With the parameter fixed in this way, the integrated reflectivity as a function of x-ray transition energy can be calculated, which is shown in figure 4.6, featuring a strong maximum around the envisaged operating energy indicated by the red dot.

The bent crystal is tilt by 2° to compensate for the asymmetry angle. By doing so the central lattice plane is parallel to – and coincides with – the optical axis, leading to symmetric, but mirrored spectra above and below the optical axis. The quantitative dependence of the distance z_d between the optical axis and the point where the diffracted rays cross the Rowland circle on the wavelength λ is given by the approximate formula 2.19 which reads for the FOCAL case as

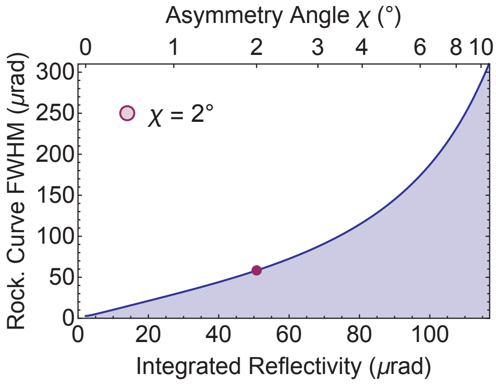

Figure 4.5: The graph shows the Rocking curve FWHM as a function of the integrated reflectivity. The FOCAL asymmetry angle of $\chi = 2°$ has been chosen at the point, where the curve starts to leave its linear behaviour, leading to an over proportional growth of the FWHM. This graph illustrates the so-called resolution vs. efficiency trade-off.

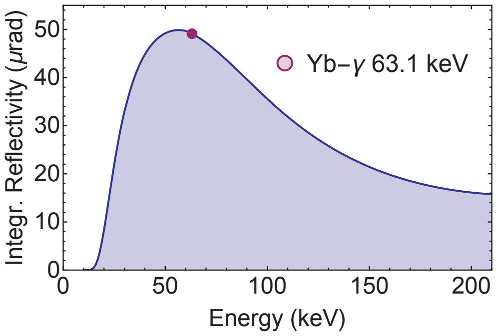

Figure 4.6: Integrated reflectivity of the FOCAL crystals (Si (220), $R = 2\,\mathrm{m}$, $\chi = 2°$) as a function of x-ray energy. The selected operation energy at 63.1 keV, as defined by the ^{169}Yb-γ calibration source, is close to the optimum. The usage of a different calibration source at 71.6 keV (see section 6.2) would not reduce the efficiency tremendously.

$$z_d = \frac{R}{2\,d_{220}}\lambda \tag{4.4}$$

with the lattice spacing of silicon $d_{220} = 192.015\,571\,4(32) \times 10^{-12}\,\mathrm{m}$ [Mohr16]. The result for the 63.1 keV Yb γ-line is $z_d = 102.3\,\mathrm{mm}$. This means that the calibration line should be found 102.3 mm above and below of the optical axis. This formula is only an approximation to illustrate the general dependence of the diffraction position z_d on the wavelength. More accurate results, which also include the asymmetry angle, the source extension etc., are obtained by full 3D ray-tracing simulations, which is addressed in detail in section 5.2.6.

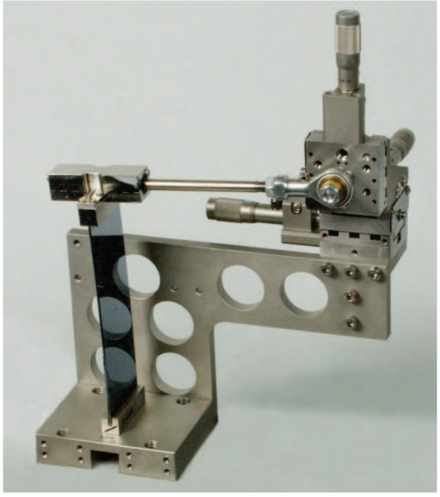

Figure 4.7: Photograph of a crystal bending device with a mount crystal (specular black). The micrometer screws pointing to the top and left are used to apply a torque onto the crystal via the sliding lever arm. The micrometer screws pointing into the paper plane is used to control the twist of the crystal around its vertical axis.

The position-sensitive x-ray detector which records the diffracted x rays is ideally placed on the edge of the Rowland circle to guarantee optimally focused lines. The large spacing between the Rowland circle and the detectors, suggested by the scheme 4.4, is in reality negligible since the drawing is not to scale.

In order to force the silicon crystal to its cylindrical shape, a dedicated crystal bending device was build (see figure 4.7). It bends the crystal by applying a torque via a long sliding lever arm. If a force perpendicular to the crystal, at the free end, instead of a torque would by applied, the resulting deflection would resemble a polynomial of third order, since the bending moment falls off linearly with distance from the fixed end. The bend and the twist of the crystal can be adjusted by tuning three micrometer screws, the whole bending procedure is described in section 5.2.1.

4.1.2 The 2D Position-Sensitive Germanium Detectors

The actual observable of the experiment is the position of the Lyman–α_1 line relative the main 63.1 keV γ–line of the ^{169}Yb calibration source. One possibility to measure this distance would be a standard semiconductor detector equipped with a narrow slit in front of the sensitive area, and to scan the whole wavelength range with the movable platform. This method is applied in the preparation phase of the experiment, where the complete upper and lower spectrum of the calibration source is recorded. Unfortunately, this method is very slow, since just one position at a time is recorded, which requires a very strong source and a long measurement period. Thus, it is preferable to use position-sensitive x-ray detectors which cover a sufficiently large part of the spectrum at once. For this purpose, a 1D position-sensitive detector was employed in an earlier beam time in 2006 [Chat06], where it was shown that even such a detector is not convenient. The reason for that is an effect called *Doppler tilt*, which only occurs when a relativistically moving source is monitored by the crystal spectrometer. For the stationary source the wavelength does not depend on the observation angle, therefore, the recorded line on the detector is horizontally orientated. If a fast moving source is observed, this is no longer the case, since according to formula 4.1 the wavelength-depends on the observation angle θ. The part of the detector viewing the moving source at an angle slightly smaller than $\theta = 90°$ registers a shorter wavelength than the part which views the source form an angle slightly higher than 90°. Hence, the line of the moving source appears slanted. The Doppler-tilt angle φ_{Dt} can be derived from the Doppler formula 4.1 and the x-ray deflection height 4.4 and results in

$$\varphi_{\mathrm{Dt}} = \beta\,\gamma\,\frac{R}{R + d_{CS}}\,\frac{\lambda_0}{2\,d_{220}} \tag{4.5}$$

with the Rowland circle radius R, the crystal–source distance d_{CS}, the silicon (220) lattice spacing d_{220} and the rest frame wavelength λ_0. The Doppler-tilt angle is proportional to the rest frame wavelength, indicating that different transitions will have diverse slopes. This illustrates that a 1D position-sensitive detector is not sufficient – if the calibration line is adjusted orthogonal to the sensitive direction, the moving source line would then be misaligned by the angle φ_{Dt}. With the theoretical values from [Yero15] in table 2.2, the Doppler-tilt angles can be calculated.

Transition	Wavelength λ_0 (pm)	Doppler Tilt φ_{Dt} (°)
$2\,p_{3/2} \rightarrow 1\,s_{1/2}$	17.3234	1.0602
$2\,p_{1/2} \rightarrow 1\,s_{1/2}$	17.8826	1.0932
$2\,s_{1/2} \rightarrow 1\,s_{1/2}$	17.8742	1.0931
$3\,p_{3/2} \rightarrow 1\,s_{1/2}$	14.8399	0.9098
$3\,p_{1/2} \rightarrow 1\,s_{1/2}$	14.9593	0.9144
$3\,s_{1/2} \rightarrow 1\,s_{1/2}$	14.9576	0.9107

Table 4.2: Calculated Doppler-tilt angles for the different transitions.

Due to this effect it becomes necessary to use 2D position-sensitive detectors, to be able to track the different line slopes for different transition energies. Commercial x-ray CCD cameras could not be used, since the maximum operation energy is about 10 keV, which is much smaller than the energy region of interest around 63.1 keV. Therefore, a custom-made semiconductor detector had to be developed and fabricated [Prot05], in close collaboration with Semikon GmbH, which was a starburst of the research centre in Jülich (FZJ). The specification of the two identical detectors have been determined by the requirements of the FOCAL experiment, and are listed in the table below.

Property	Value
Semiconductor Material	Germanium Single Crystal
Size of the Crystal	70 mm × 41 mm, 11 mm Thick
Sensitive Area	56 mm × 32 mm
Front-Side Strips (Cathode)	128, 250 μm High
Back-Side Strips (Anode)	48, 1.167 mm Wide
High-Voltage Supply	900 V – 1000 V
Energy Resolution (FWHM)	2.5 keV at 60 keV Photon Energy
Signal Rise Time	90 ns

Table 4.3: Specifications of the 2D position-sensitive germanium detector.

The detector consists of an 11 mm thick germanium single crystal, with a, in many strips structured, anode and cathode. Each strip has its own amplifier and readout electronics and behaves in this sense as a standard semiconductor detector. Due to the high segmentation, a large number of detectors are available on one crystal. The strips on the front and on the back side are oriented perpendicular with respect to each other, which allows a two-dimensional position reconstruction, if front- and back-side strips with the same measured energy are combined. In this way, a $48 \times 128 = 6144$ pixel detector can be emulated. The narrow strips on the front are orientated perpendicular to the dispersive direction of the spectrometer, allowing a more precise position determination. The coarse strips on the back side are needed to account for the Doppler tilt and cover an observation angle range of $\theta = 90^\circ \pm 0.62^\circ$ around the gas-jet target.

Even the 250 μm pitch of the front-side strips are too coarse to determine the line position with the needed precision. Therefore, the whole detector is tilt by about 1° against the Doppler-tilt rotation direction, which leads to a rotation of the ^{169}Yb calibration line in the reference system of the detector, although it is perfectly aligned horizontally in the canonical reference frame of the ESR cave. By utilising this trick, all recorded lines cross several front side strips allowing a much more precise position determination, by applying a full 2D fit onto the recorded spectrum.

In one way multi-strip detectors behave differently from several individual standard germanium detectors, which is known as *charge splitting*. This effect appears when an x-ray photon is absorbed between two strips. The generated charge clouds, which consist of electrons drifting to the anode and holes drifting to the cathode, are distributed among two neighbouring strips. The result is one x-ray event where two strips have recorded an arbitrary fraction of the complete charge. The sum charge of both strips adds up to the charge, which would be collected if just one strip would be hit [Spil09]. These split events can also be analysed to improve the statistical uncertainty of an experiment [Chat07]. As will be detailed out in section 5.1, this has not been done in this work due to the following four reasons: *(i)* Due to the fact that two instead of only one strip has to be analysed, the background of these spectra is higher than the single-strip spectrum, relativising the advantage of the higher statistics. *(ii)* Charge-split events are not as unambiguous as single-strip events resulting in a possible source for systematic errors. *(iii)* Other systematic error sources, which could be identified in the course of the data analysis predominate the uncertainty due to the counting statistics. *(iv)* The number of charge-split events is lower than the single-strip events which would improve the total result by a few percentage points only, which is disproportionate to the required effort for a more complex, and therefore error-prone, data analysis.

As already mentioned, each strip has the possibility to record a complete x-ray spectrum. Although the resolution of 2.5 keV at 60 keV photon energy does not challenge unstructured semiconductor detectors, with resolutions down to 400 eV, this information can still be used to reject background radiation which comes for example from the florescence transitions of the shielding lead. Also, the fast signal rise time of 90 ns in combination with the fast particle detector can be used to setup a coincident data acquisition system, where only those x rays will be considered as true events, when at the same time a down-charged ion has been detected in the particle detector. More detailed information on this technique is given in the next section. All these capabilities together – position, time and energy sensitivity – makes these detectors one of the key elements of the FOCAL experiment, which allows to sort out the most promising events and generate an almost background-free spectrum.

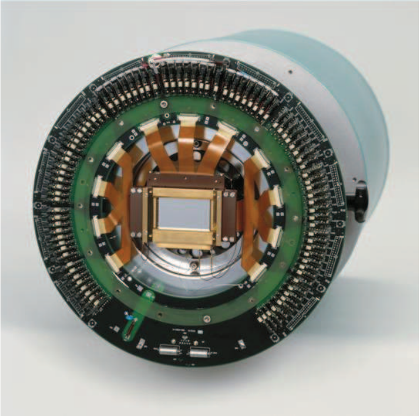

Figure 4.8: Photograph of one of the 2D position-sensitive germanium detectors with opened cryostat. The grey block in the middle is the structure germanium single crystal. Radial around the crystals, the pre-amplifier circuit boards are mount. The turquoise coloured part in the background is the liquid nitrogen Dewar for the cooling of the crystal.

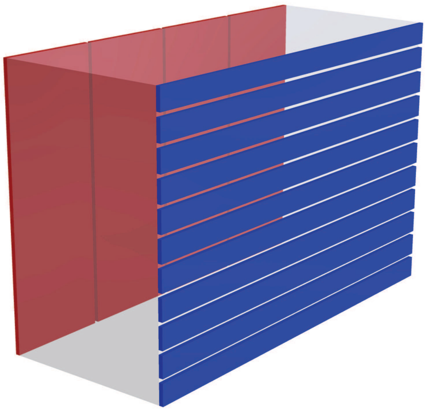

Figure 4.9: Schematic of the structured germanium single crystal block. The blue horizontal strips on the front are quite narrow and are aligned almost perpendicular to the dispersive direction of the crystal spectrometer. In this way maximum position sensitivity is reached. The wide red strips in the back are needed to correct for the Doppler tilt.

4.1.3 The Particle Detector

As already mentioned in the previous section, background reduction is crucial to sort the few true events out of the huge background. One very important aspect of background reduction is the coincident measurement of a registered x-ray photon and the corresponding down-charged ion. This is sometimes called *active shielding* in contrast to *passive shielding* with thick lead and tungsten plates.

If an ion captures an electron from the gas-jet target, and eventually emits a characteristic photon in the direction of the spectrometer, its charge state has changed by one unit according to the following scheme

$$ {}^{197}\mathrm{Au}^{79+} + e^- \longrightarrow {}^{197}\mathrm{Au}^{78+} + \gamma \qquad (4.6) $$

By this process, the mass of the ion has changed only by $3 \times 10^{-4}\,\%$, since the electron is much lighter than the heavy ion, but the charge has changed by more than one percent. Therefore, also the mass-to-charge ratio in formula 3.1 goes down by more than one percent, and since the magnetic field B and the velocity is the same as that of the originally charged ion, the bending radius in the dipole magnets has to increase. This will spatially split up the beam into the original beam, and a down-charged beam. If the beamline of the storage ring is not wide enough, those ions hit the wall, and are finally lost. To make use of these ions, a particle detector in the dipole magnet, following the gas-jet target, can be moved very close to the primary beam, which records the impinging time of every single down-charged ion, which can – in the ideal case – be correlated to an event in the x-ray detectors. The position of the particle detector can be seen in figure 3.3.

The particle detector is a gas-filled multi-wire proportional counter (MWPC, see photograph 4.10) [Klep03], which can sustain very high count rates of up to 200 kHz with a temporal resolution of about 10 ns [Klep92]. The MWPC is mount in a pocket with a 25 μm thin stainless steel window, in order to allow also very slow ions, with kinetic energies down to 10 MeV/u, to pass and be registered in the MWPC. The pocket is moved via a pneumatic drive, with a maximum velocity of 250 mm/s, and has a position reproducibility of 0.1 mm. The detector has an efficiency of more than 99 %, meaning that basically no true events are lost by applying the coincidence condition. The coincident condition is not hard-wired into the data acquisition system, but rather gets stored as a time stamp in the LMD measurement data. This has the big advantage that all timing conditions can be adjusted during the data analysing process and no data are lost due to poorly chosen limits in the preparation phase. In this way, also prompt spectra, without a timing condition, can be created to study the background.

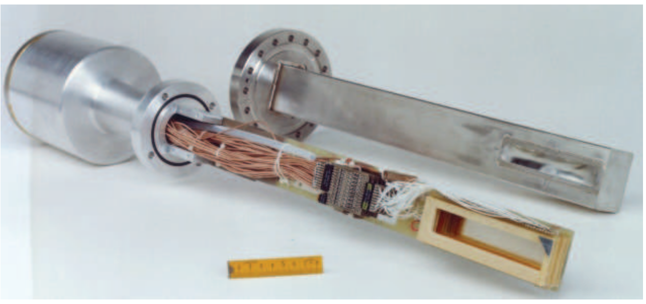

Figure 4.10: Photograph of a gas filled multi wire proportional counter (front) and the pocked in which it is mount (back). The picture has been taken from [Klep92].

4.1.4 The Calibration Source

In section 2.2.6 it was stated, that a spectrometer operated in a modified Cauchois geometry is not able to measure absolute wavelengths, but is rather a wavelength comparator, meaning that at least one calibration line is need, if the spectrometer dispersion is known. For this purpose, a radioactive element with a strong and well-known γ-line had to be selected. The calibration line should also be located in the vicinity of the maximum of the integrated reflectivity curve (see figure 4.6) which is around 60 keV. The choice fell on the isotope 169-ytterbium, which possess a very strong γ-line with a reference energy of 63 120.44(4) eV [Be04]. The source consists of 25 mg of isotope-enriched ytterbium oxide ($^{168}\mathrm{Yb}_2\mathrm{O}_3$). The ytterbium oxide is contained in a small aluminium tablet of 5 mm in diameter. By neutron activation in the TRIGA research reactor in Mainz [Inst16] a part of the ^{168}Yb is converted to ^{169}Yb through neutron capture by the following scheme

$$^{168}\mathrm{Yb} + n \xrightarrow{n\text{ caputre}} {}^{169}\mathrm{Yb} \xrightarrow{\beta^+/\varepsilon\ (32\,d)} {}^{169}\mathrm{Tm} + \gamma\text{'s} + \text{x rays} + \cdots \tag{4.7}$$

The artificially produced ^{169}Yb decays via a β^+ or an electron capture ε to 169-

thulium, where a number of γ's and characteristic x rays are emitted. An example spectrum obtained with FOCAL via scanning the dispersive direction with a standard semiconductor detector, equipped with a narrow slit, is shown in figure 4.11. For comparison, the same spectrum, measured with a good germanium detector, is superimposed. It is evident that the resolution of FOCAL is much higher and subtle details, like the Tm Kβ_1 – Kβ_3 splitting, can only be revealed with such a device.

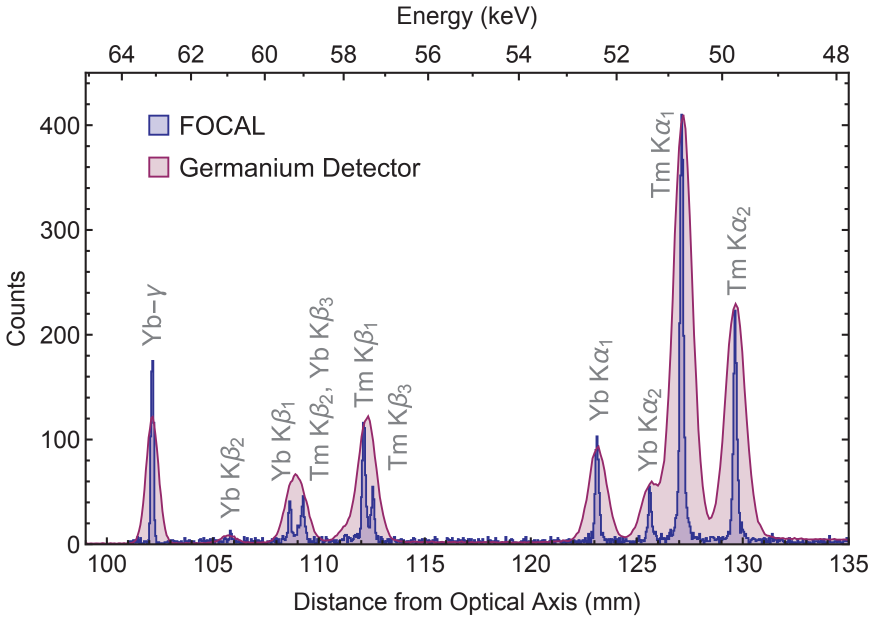

Figure 4.11: Measured energy spectrum of the ^{169}Yb calibration source with FOCAL (blue) and a standard germanium detector (red). The germanium detector has an energy resolution of 420 eV (FWHM) at 60 keV photon energy, which is too poor to compete with FOCAL. Subtle details, like the Tm Kβ_1 – Kβ_3 splitting, cannot be resolved with the semiconductor detector.

When a final activation of 1.5×10^9 Bq was achieved, the source has been delivered to GSI, where it was mounted into the source-positioning unit. The positioning unit consists of a long cantilever arm driven by a linear actuator to move the source at the same location, where the ion beam intersects with the gas-jet target. This was done to minimise systematic deviations between data collected with the beam and the calibration source. As will be explained in detail in section 5.1.4, about every six hours the ion beam was switched off and a calibration spectrum was recorded to monitor an eventual drift of the setup.

4.1.5 The Data Acquisition System

In figure 4.12 a schematic drawing of the experimental assembly and the electronic wiring is shown. On both sides of the gas-jet target, the FOCAL spectrometers can be seen. Additionally, a standard germanium detector aiming for the interaction region is located at the 150° port of the target chamber. The fraction of the Au^{79+} ion beam interacting with the gas-jet target is magnetically separated from the stored beam, in the dipole bending magnet of the ESR, and hits the particle detector. For each x-ray detector a separate, but identical data acquisition system (DAQ) has been used. If an x-ray photon (red lines) was hitting a detector the generated signal was amplified in a pre-amplifier inside the detector housing and feed into the DAQ. There, the signal was again amplified in a fast timing filter amplifier (TFA) and split in two signals, one optimised for precise timing and the other for a good energy resolution. If the timing signal was higher than a pre-defined threshold, the constant fraction discriminator (CFD) started the time to digital converter (TDC), which acts as a stopwatch between x-ray and the particle detector event. The CFD also reported to the main control computer (RIO, [Crea16]) of the DAQ that an event to be processed has been registered. The energy signal generated by the TFA was meanwhile once more amplified in the main spectroscopy amplifier, and got digitised in an analogue-to-digital converter (ADC). The result of the ADC was then read out by the RIO. After some nanoseconds the down-charged ion, which had emitted the x-ray photon, travelled the distance to the particle detector, where it generated another signal. This particle detector signal was also amplified, and stopped the TDC stopwatch. Also this time difference was read out by the RIO, which then bundled all the information to a data block and sent it via a fast Ethernet network to a file server, which stored the information in a list-mode file (LMD) on hard drives. This procedure was repeated for every single photon leading to 275 GB of pure measurement data.

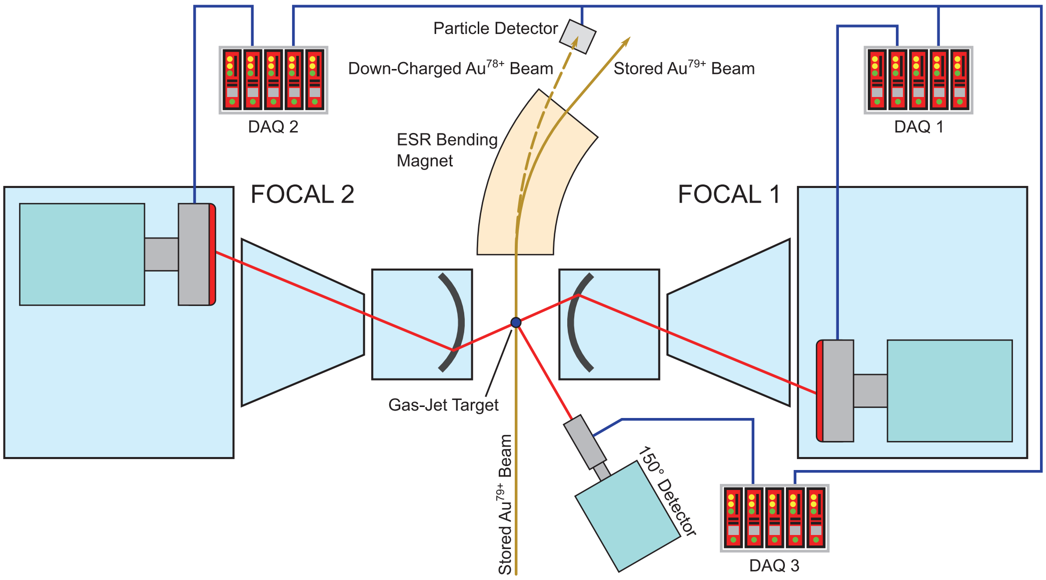

Figure 4.12: Schematic wiring of the data acquisition system (DAQ). Each spectrometer setup has its own DAQ, but the signal form the particle detector is shared by all of them.

4.2 Measuring the 1s Lamb shift

The main goal of the FOCAL experiment presented in this work is the precise determination of the 1 s Lamb shift in hydrogen-like gold $^{197}\mathrm{Au}^{78+}$. As already stated in section 2.1.2 the Lamb shift is the energy difference between the measured level energy and the Dirac value for a point-like nucleus. The Lamb shift can be calculated by modern theories, taking the nuclear size and QED contributions into account. To test the prediction made by these theories, it is desirable to measure the Lamb shift for the 1 s state in heavy highly charged ions, since the energy shift scales like $\Delta \mathrm{E}_{\mathrm{LS}} \propto \mathrm{Z}^4/\mathrm{n}^3$, with Z being the nuclear charge and n the principal quantum number. Since the Dirac value for the level energy is a purely theoretical construct the Lamb shift cannot be measured directly, and a detour has to be taken as illustrated in the scheme below.

$$\Delta \mathrm{E}_{\mathrm{LS}}^{1s} = \left(\mathrm{E}_{2p_{3/2}}^{\mathrm{theory}} - \mathrm{E}_{\mathrm{Lyman}-\alpha_1}^{\mathrm{experiment}}\right) - \mathrm{E}_{1s_{1/2}}^{\mathrm{Dirac}} \tag{4.8}$$

The transition energy $\mathrm{E}_{\mathrm{Lyman}-\alpha_1}^{\mathrm{experiment}}$ of the Lyman-α_1, $2\,p_{3/2} \rightarrow 1\,s_{1/2}$, is measured with high precision, this is the task of the FOCAL experiment. The hence obtained value is subtracted from the theoretical level energy $\mathrm{E}_{2p_{3/2}}^{\mathrm{theory}}$ for the $2\,p_{3/2}$ state, with its well-understood Lamb shift contribution of only 4.3 eV. From this difference, the Dirac value for the 1 s state $\mathrm{E}_{1s_{1/2}}^{\mathrm{Dirac}}$ is subtracted, which yields the energy value for the 1 s Lamb shift $\Delta \mathrm{E}_{\mathrm{LS}}^{1s}$. The measurement principle 4.8 is illustrated in the level diagram 4.13, which shows why the $2\,p_{3/2} \rightarrow 1\,s_{1/2}$ transition has been selected as the main experimental observable. All states, but the $2\,p_{3/2}$, lie energetically very close to other excited states. In the diagram this is exemplarily shown for the Lyman-α_2 transition, which consists of a blend of the $2\,s_{1/2} \rightarrow 1\,s_{1/2}$ and the $2\,p_{1/2} \rightarrow 1\,s_{1/2}$ transition. If the blending ratios are unknown the measurement principle 4.8 cannot be applied. In section 5.2.5 it is shown how the blending ratio may be calculated, but the uncertainty linked with this procedure decreases the precision of the experiment. For this reason the $2\,p_{3/2} \rightarrow 1\,s_{1/2}$ transition has been selected, which is free of any blend and no cascade calculation have to be performed.

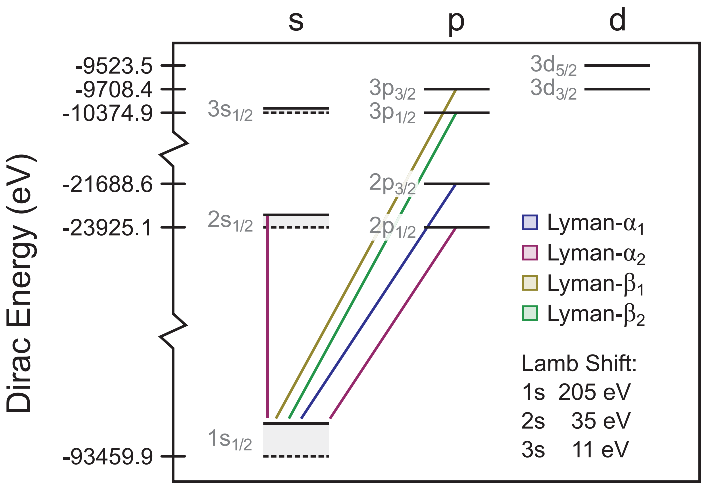

Figure 4.13: Level diagram of the lowest excited states in hydrogen-like gold. The ordinate shows the level energy according to the Dirac equation, which deviates from the measured ones especially for the s-states. The characteristic Lyman transitions are drawn in different colours. All transitions, except the Lyman-α_1 transition, consist of a blend of at least two lines.

For this endeavour starting from 13 March 2012 the FOCAL components had been assembled and carefully aligned in the ESR cave. Photograph 4.14 shows the FOCAL 1 spectrometer in the inside of the ESR storage ring.

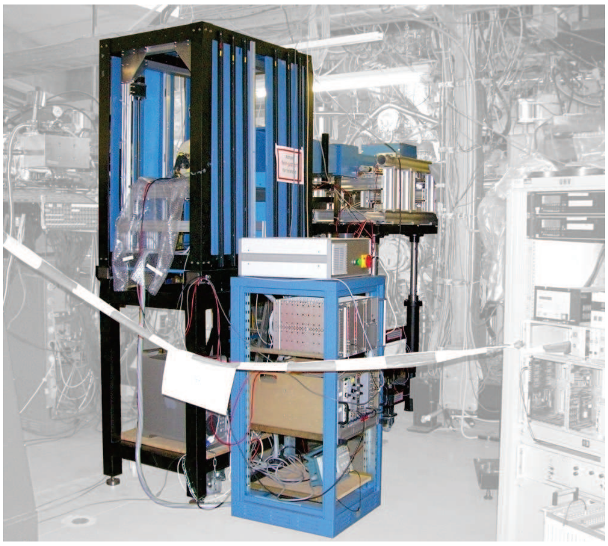

Figure 4.14: Photograph of the FOCAL 1 setup in the inside of the ESR storage ring. The rack in front of the detector stage houses the electronic for the movable platform, the rack for the 2D germanium detector read out is not yet installed.

After this, first test scans with the calibration source have been performed. An example graph of these activities is shown in figure 4.11. Including checking and ensuring the proper function of both spectrometers a time span of one month passed by. On 13 April 2012 the ESR cave was shut for beam operation, starting with tuning the storage ring for the upcoming production run. The completely ionised $^{197}\mathrm{Au}^{79+}$ ions coming from the SIS18 at a kinetic energy of 400 MeV/u were decelerated in the ESR to ≈ 124.8 MeV/u. At this energy, the electron cooler was switched on to reduce the momentum spread of the beam. After the ion beam was successfully stored, the overlap between the decelerated and cooled ion beam and the gas-jet target was optimised. In this phase, first spectra with a standard germanium detector located at the 150° port of the target chamber were recorded, which are shown in figure 4.15.

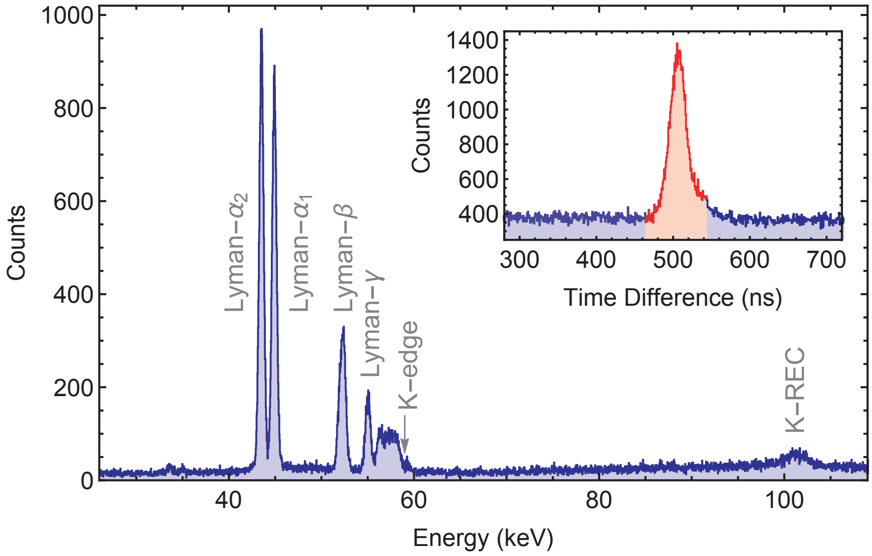

Figure 4.15: Energy spectrum of the germanium detector viewing the interaction zone from an angle of 150° (see figure 4.12). Besides the characteristic Lyman transitions stemming from the hydrogen-like gold, the K-REC electron capture can be seen around 100 keV. The inset shows the TDC time difference between the registered x-ray event in the germanium detector and the ion hitting the particle detector.

The x-ray spectrum was recorded in coincidence with the down-charged ions detected in the particle detector. The corresponding TDC spectrum can be seen in the inset, with the red-shaded area indicating the selected coincidence condition. Between 40 and 60 keV the characteristic Lyman transitions from an excited to the 1 s ground state can be identified. The only single-transition line is the Lyman-α_1, all the other lines are a blend of at least two transition due to the limited resolution of the germanium detector. The Lyman-α_2 *e.g.* is a blend of the $2\,p_{1/2} \rightarrow 1\,s_{1/2}$ and the $2\,s_{1/2} \rightarrow 1\,s_{1/2}$ transition, with a rest frame separation of just about 35 eV, which cannot resolved with FOCAL either. On the very right, around 100 keV, the K-REC can be seen, which is the transition of an electron bound to the target-gas atoms being captured directly into the ground state of the fast approaching ion. The intensity of this transition is quite low, since the selected target gas type and ion velocity were optimised in favour of the non-radiative electron capture (NRC), which preferably populates excited states, in order to increase the intensity for the characteristic transitions. After the proper operation of the ESR and experiment electronic was checked, the main production run could be started. In the following weeks all settings were kept unchanged and the beam operation was only stopped for calibrations with the Yb source, or for liquid nitrogen refilling. The accumulation of coincident Lyman-α_1 counts as a function of time can be seen in figure 4.16, which increases rather constant with time indicating a smooth operation of the ESR.

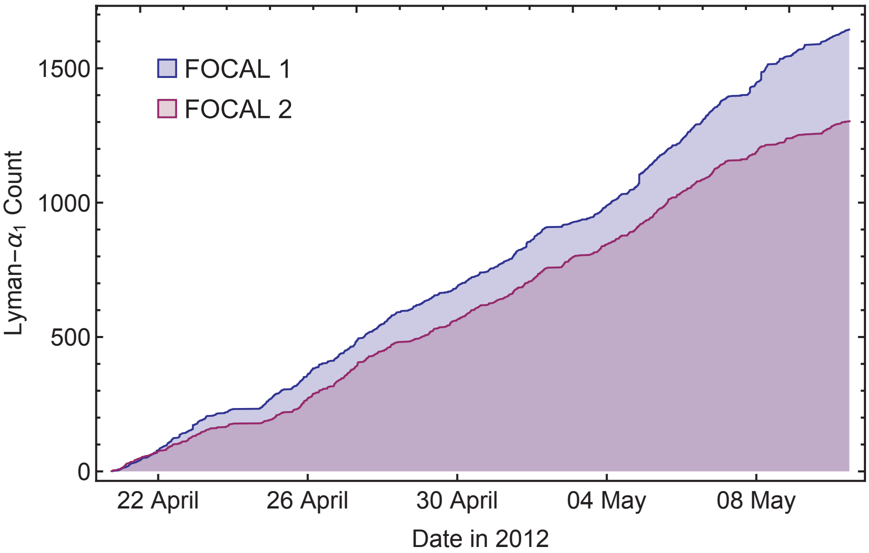

Figure 4.16: Accumulated Lyman-α_1 counts as a function of the date in 2012 over the whole beam time. The count increased rather constant with time, indicating a smooth and almost disturbance free operation of the ESR.

The beam time was over on 10th of May and about 1 500 Lyman-α_1 counts per spectrometer could be collected. Converted to a rate, this is just about three counts per hour. After the beam time was over, the FOCAL setup was removed from the target area making space for other experiments to be conducted.

Chapter 5

Analysis of the Experimental Data

During the successful beam time in April and May 2012, a lot of data was collected, which had to be analysed very carefully. The determination of the line positions on the detector is a rather small issue, compared to the identification and evaluation of influences stemming from various systematic effects. These lead to systematic measurement deviations, and will therefore dominate a major part of this chapter. Note: If the graphs shown in the following are similar for both FOCAL spectrometers, just one is displayed to avoid repetition.

5.1 Analysis of the X-Ray Data

In this section, the data recorded with the position sensitive x-ray detectors will be analysed. It can be divided into two parts: The first part treats the data collected with the Yb-γ calibration source. Important characteristics, such as the spectrometer dispersion and the position drift of the detectors over a long period of time, is studied in detail. In the second part of the x-ray data analysis, the transitions in the ions are considered. The results obtained in the first part are important input parameters for the transition-energy determination and uncertainty estimation.

5.1.1 Analysing the Yb-Source X-Ray Spectrum

The spectra obtained with the stationary ^{169}Yb source serve different purposes. They were recorded before the actual beam time to position the x-ray detectors at the right height. The ^{169}Yb-γ line is also used as the primary wavelength reference to calibrate the spectrometer. This calibration was done every six hours to monitor possible position drifts during the long measurement term of three weeks. In total, 75 ^{169}Yb calibrations have been performed during the beam time. Graph 5.1 shows a typical spectrum as obtained from the 2D x-ray detector. It has to be kept in mind that here not the lines are tilted, but that the 2D detector itself is rotated by about 1°, as described in section 4.1.2, to increase the precision of the position determination by fitting. The dispersive direction of the spectrometer is orientated vertically, mapping transitions with distinct wavelengths onto different horizontal strips. The most energetic transition in this graph is the ^{169}Yb-γ line located around the (horizontal) strip 50, the lowest energetic transitions are the Tm-Kβ transitions around strip 90.

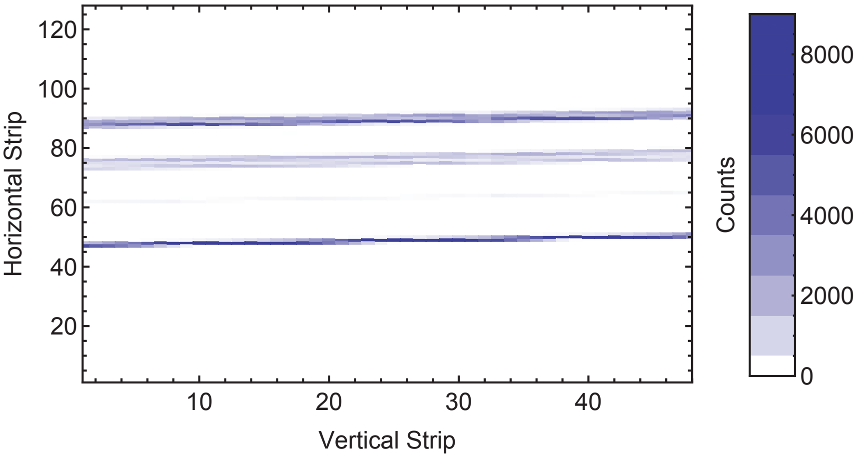

Figure 5.1: 2D spectrum of the ^{169}Yb calibration source as recorded by one of the position sensitive detectors. The strong line around the horizontal strip number 50 is the main ^{169}Yb-γ calibration line, whereas the broad lines around strip number 75 and 90 actually consist of two or more lines, as will become clear from the projection in graph 5.2.

2D spectra like this are not easy to interpret for the reader, since relative intensities and positions are hard to estimate. Therefore, projected 1D spectra are provided. The projections are done with respect to the tilt angle of the lines, and the rasterisation is not limited to the strip width, but can rather have an arbitrary value. The projections are only made for illustrating reasons, the actual fitting of the line position is always performed on the full 2D spectra, which is more direct and does not suffer from information loss.

The projected spectrum of graph 5.1 is shown in figure 5.2, with logarithmic scaling of the ordinate. In this graph, many more features are revealed to the human eye, and it becomes obvious that the broad lines in graph 5.1 are actually a blend of two equally strong lines. Besides the strong ^{169}Yb-γ line, the characteristic atomic x-ray transitions of excited ytterbium and thulium (Tm) atoms can be seen. Since the source holder is made of tungsten (W), also characteristic transitions stemming from this material can be found.

5.1.2 Line Position Determination

One of the most important tasks of the data analysis is the precise determination of the diffracted x-ray line position on the detector, via a fitting procedure. The most crucial part hereby is to define a fit function which resembles the “true” line shape rather well. The first step for constructing the model function is to recreate the output of the crystal, which is given by the rocking curve in figure 2.8. A fairly

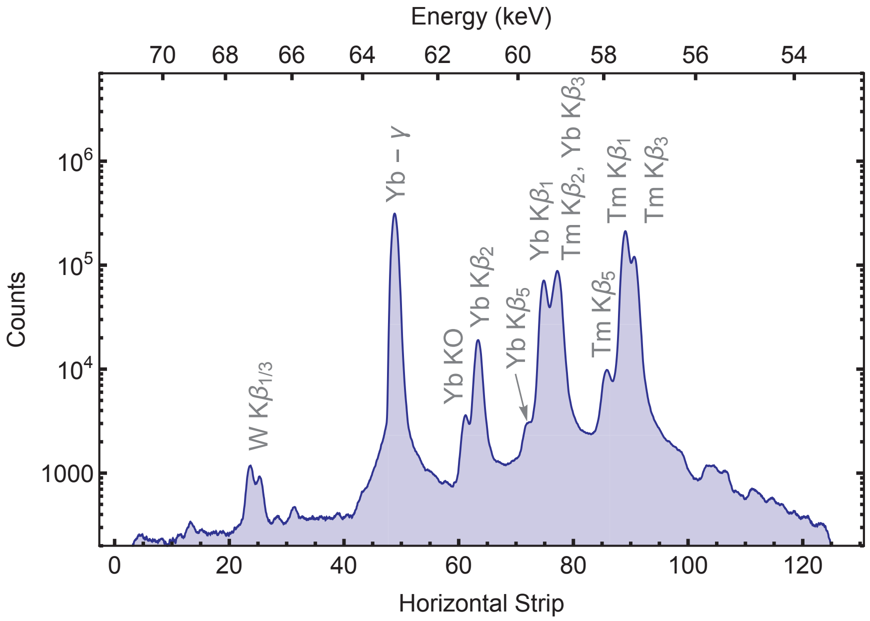

Figure 5.2: Projection of the 2D spectrum shown in figure 5.1 with respect to the line tilt angle. Besides the main ^{169}Yb-γ calibration line, a lot of other characteristic x-ray transitions stemming from ytterbium, or the daughter product thulium, can be identified.

good approximation for the $\chi = 2°$ case is a simple rectangular function $\Pi(z, \sigma)$, with a width σ.

$$\Pi(z, \sigma) := \begin{cases} 1/\sigma & |z| < \sigma/2 \\ 0 & |z| \geq \sigma/2 \end{cases} \tag{5.1}$$

The rectangular shaped x-ray beam then impinges on the 2D detector. Each horizontal strip has also a rectangular shaped response function with a width Δz, since it gives a signal, if the photon hits the strip somewhere, or it gives no signal, if the strip was missed. Therefore, the model up to now can be obtained by a convolution of two rectangular functions of (in the most general case) two different widths. The result will be a trapezoid function with a base length of $\Delta z + \sigma$, and a constant plateau region of length $\Delta z - \sigma$ (if $\Delta z \geq \sigma$ is assumed). Another important aspect of the total fit function is the fact, that the x-ray beam penetrates the germanium crystal of the 2D detector for a certain depth, instead of being completely absorbed at the surface. This effect is described by the Beer-Lambert law, which relates the intensity I of an x-ray beam with an exponential decrease of the initial intensity I_0, as a function of penetration depth $I(x) = I_0 \exp(-x/\lambda)$, where λ is the material and energy dependent attenuation length. The finite penetration of the beam would not change the position or shape of the fit function, if the x-ray beam would hit the 2D detector perfectly perpendicular, but it rather impinges under an angle slightly smaller than 90°, which can be seen in figure 4.4. By taking this effect into account, the trapezoid function has to be convoluted once more with a single sided exponential

$$\exp^{\geq 0}(x,\tau) := \begin{cases} 1/\tau\, e^{-x/\tau} & x \geq 0 \\ 0 & x < 0 \end{cases} \tag{5.2}$$

with τ being the attenuation length component parallel to the surface, which is given by $\tau = \cos(\alpha)\,\lambda$, with the impinge angle α. Hence, the total model function TMF is given by

$$\mathrm{TMF}(z,\sigma,\Delta z,\tau) := \left\{ \left[\Pi(z',\sigma) \overset{z'}{*} \Pi(z',\Delta z) \right](x) \overset{x}{*} \exp^{\geq 0}(x,\tau) \right\}(z) \tag{5.3}$$

$$\mathrm{TMF}(z,\sigma,\Delta z,\tau) = \begin{cases} \frac{e^{-\frac{2z+\Delta z+\sigma}{2\tau}}\left(e^{\frac{2z+\Delta z+\sigma}{2\tau}}\sigma+\tau-e^{\sigma/\tau}\tau\right)}{\sigma} & \text{for } \textit{(i)} \\ \frac{e^{-\frac{2z+\Delta z+\sigma}{2\tau}}\left(-1+e^{\Delta z/\tau}\right)\left(-1+e^{\sigma/\tau}\right)\tau}{\sigma} & \text{for } \textit{(ii)} \\ -\frac{2z+e^{-\frac{2z+\Delta z+\sigma}{2\tau}}\left(2\left(-1+e^{\Delta z/\tau}+e^{\sigma/\tau}\right)\tau-e^{\frac{2z+\Delta z+\sigma}{2\tau}}(\Delta z+\sigma+2\tau)\right)}{2\sigma} & \text{for } \textit{(iii)} \\ \frac{2z+\Delta z+\sigma+2\left(-1+e^{-\frac{2z+\Delta z+\sigma}{2\tau}}\right)\tau}{2\sigma} & \text{for } \textit{(iv)} \\ 0 & \text{otherwise} \end{cases}$$

(i) $(z \leq 0 \wedge 2z + \Delta z > \sigma) \vee (z > 0 \wedge 2z + \sigma \leq \Delta z)$
(ii) $2z > \Delta z + \sigma$
(iii) $z > 0 \wedge (2z = \Delta z \vee (2z \geq \Delta z \wedge 2z \leq \Delta z + \sigma) \vee (2z + \sigma > \Delta z \wedge 2z \leq \Delta z))$
(iv) $z < 0 \wedge (2z = -\Delta z \vee (2z \geq -\Delta z \wedge 2z + \Delta z \leq \sigma) \vee (2z + \Delta z > -\sigma \wedge 2z \leq -\Delta z))$

(5.4)

Up to now, the total model function TMF is defined in just one (the dispersive) dimension and is centred around the origin. In order to cover also the non dispersive direction on the detector, and to account for different line positions μ, the TMF is simply extruded into the x-axis with respect to a tilt angle θ

$$\mathrm{TMF}_{2\mathrm{D}}(x,z,\mu,\theta,\sigma,\Delta z,\tau) := \mathrm{TMF}(z-(\mu+x\tan(\theta)),\sigma,\Delta z,\tau) \tag{5.5}$$

The definition of the line position is the barycentre of the curve which does *not* coincide with the maximum. The barycentre is given by

$$\bar{z} = \int\limits_{-\infty}^{\infty} \mathrm{TMF}_{2\mathrm{D}}(0,z,\mu,\theta,\sigma,\Delta z,\tau)\cdot z\,dz = \mu+\tau \tag{5.6}$$

The function $\mathrm{TMF}_{2\mathrm{D}}$ is multiplied with an amplitude and a background is added, to be finally fitted to the real 2D measurement data. An actual fit of the function TMF (continuous blue curve), to real projected measurement data (points in dark red), can be seen in figure 5.3. The shown line is the strong ^{169}Yb-γ transition. When fitting the actual measurement data, it is more convenient to convert the coordinate system from strips to millimetre, with an origin located at the centre position $\{24.5, 64.5\}$ in strips. The slight asymmetry in figure 5.3 to lower energies (increasing position) is due to the already mentioned finite penetration depth in the 2D detector, and goes for both spectrometers and all four possible observation positions into the direction of lower energies.

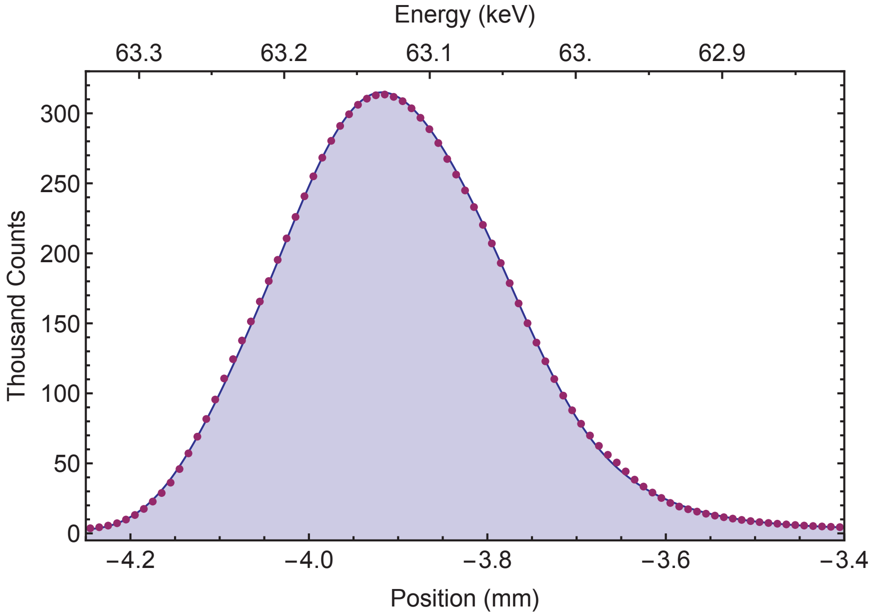

Figure 5.3: Magnified section of the main ^{169}Yb-γ calibration line (red points) from figure 5.2. The tail of the curve to lower energies (increasing position) is caused by the non-perpendicular incident of the x-ray beam, in combination with the finite penetration depth in germanium. The model function TMF (blue curve) is fitted to the data and accounts for the asymmetry.

From the fit a τ value of $76.6(1)\,\mu$m is obtained. With the impinge angle $\alpha = 86.4(1)^\circ$, an experimental attenuation length of $\lambda_{exp} = 1.22(4)$ mm can be calculated. The literature value for 63.1 keV photons penetrating germanium is 1.23 mm [Berg98], which agrees quite well with the FOCAL result.

5.1.3 Wavelength Calibration of the FOCAL Spectrometers

As already mentioned in section 2.2.6 a modified Cauchois-type spectrometer is a wavelength comparator, which needs to be calibrated with known γ or x-ray lines. For that purpose, the main ^{169}Yb-γ calibration line and other reasonably well-known transitions, stemming from the calibration source, have been fit with the TMF$_{\mathrm{2D}}$ function. The literature values for the selected transitions are listed in table 5.1.

According to formula 4.4 the location of the lines depends linearly on the wavelength, therefore, the simple ansatz

$$\lambda(z_d) = D\, z_d + b \tag{5.7}$$

Transition	Wavelength (pm)	Energy (eV)	Reference
Tm-Kβ_3	21.636 6(30)	57 303.0(79)	[Desl03]
Tm-Kβ_1	21.559 184(56)	57 508.76(15)	[Desl03]
^{169}Yb-γ	**19.642 479(12)**	**63 120.44(4)**	[Be04]

Table 5.1: Compilation of literature values for various x-ray and γ-ray transitions used for calibration.

with the spectrometers dispersion D, and an offset b, can be made. The value of D is an important characteristic of the spectrometer, whereas the offset b depends only on the definition of the origin, and has no physical meaning. The results of fitting function 5.7 onto the positions of the calibration lines, is listed in table 5.2.

Spectrometer	Dispersion D
FOCAL 1	$1.905\,29(53) \times 10^{-10}$
FOCAL 2	$1.909\,74(52) \times 10^{-10}$

Table 5.2: Experimentally determined dispersions D for the two FOCAL spectrometers.

The dispersion D can also be approximately calculated by deriving equation 4.4 with respect to z_d

$$D_{th} = \frac{d\lambda}{dz_d} = \frac{2\,d_{220}}{R} \tag{5.8}$$

By using the Rowland circle design radius of $R = 2\,000\,\mathrm{mm}$ and the literature value for the silicon lattice spacing $d_{220} = 192.015\,571\,4(32)\,\mathrm{pm}$, $D_{th} = 1.92 \times 10^{-10}$ is obtained, which is in a fairly good agreement with the fitted values from FOCAL if one neglects deviations for the Rowland circle radius, which are treated in section 5.2.1.

Figure 5.4 shows the residuals for the different selected transitions (red points), in combination with the position-dependent confidence interval (blue region). The error bars consist of the combined literature value uncertainty, plus the resulting component introduced by the position uncertainty. The confidence interval is the narrowest in the vicinity of the ^{169}Yb-γ, which illustrates why the Lyman-α_1 transition is Doppler tuned to this region.

5.1.4 Temporal Drift of the Calibration Line Position

During the beam time, the calibration with the ^{169}Yb source was done every six hours, to monitor a potential drift in position. For that purpose, the position of the ^{169}Yb-γ line has been determined for each of the 75 calibrations, and the results are shown in figure 5.5. A position drift of 50 μm (100 μm) for FOCAL 1 (FOCAL 2) can be seen. Although a drift of less than 100 μm over three weeks of beam time is not much for the normal experience, it is of major concern for a high-precision experiment like FOCAL. A shift Δz in position corresponds to a shift in energy via

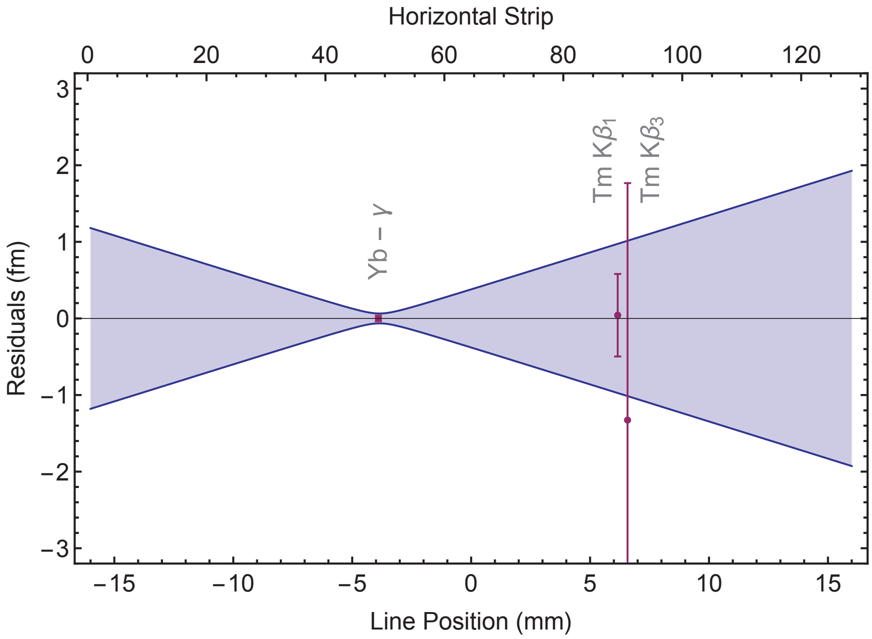

Figure 5.4: Residuals of the used calibration lines (red points), to fit the dispersion (equation 5.7). The error bars consist of the wavelength uncertainties from the literature values (see table 5.1), and the position uncertainty due to the fitting procedure. The blue region indicates the $1\,\sigma$ confidence band of the fit. It is the narrowest around the main ^{169}Yb-γ calibration line, which is the reason why the Lyman-α_1 transition is Doppler tuned to this position.

$$\Delta E \approx \frac{\partial E}{\partial z}\,\Delta z = \frac{E^2}{hc}\,D\,\Delta z \tag{5.9}$$

with D being the dispersion from table 5.2. For shifts of $\Delta z = 100\,\mu\text{m}$ at the main ^{169}Yb-γ calibration line energy, one obtains $\Delta E \approx 60\,\text{eV}$, which would be much larger than the envisaged experimental uncertainty. To compensate for this drift, each registered Lyman-α photon has its own timestamp, when it was recorded, to correct its position according to the curves seen in figure 5.5.

The reason for this drift might be explained by temperature variation in the experimental cave. Over the whole beam time, the temperature of both spectrometers was monitored, and a slight correlation between temperature and drift could be seen. The temperature in the ESR cave, averaged over the whole beam time, was $T_{ESR} = 27.2(2)\,°C$, with slightly lower temperatures at the beginning, when for both setups the largest movement could be observed.

5.1.5 Analysis of the Lyman Data

The analysis of the Lyman data is similar to that of the Yb-calibrations, as described in section 5.1.1, but an additional timing information from the TDCs has to be considered. Graph 5.6 (a) shows the combined energy spectrum of all vertical strips without “Prompt”, and with a coincidence condition “Coincident”. Whereas in the prompt spectrum, just the characteristic lead (Pb) transitions from the shield resting upon

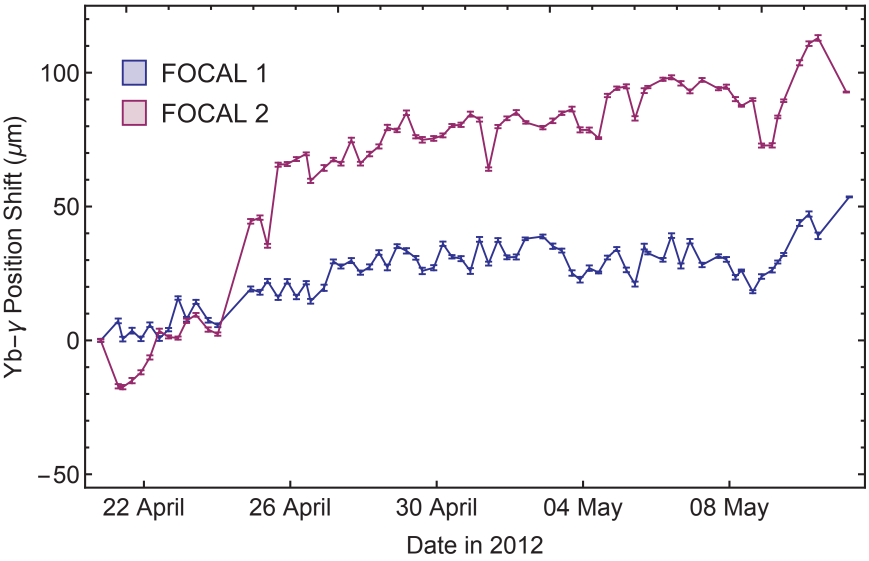

Figure 5.5: Position drift of the main ^{169}Yb-γ calibration line as a function of the date in 2012, for all 75 individual calibrations. The solid lines are drawn to guide the eye.

a strong background can be seen, the coincident spectrum shows a clear indication of the Lyman-α transitions. The Lyman-α peak should consist of two distinct lines, but due to the low energy resolution of the 2D detectors the lines blend. The same happens for the Lyman-β peak, which also contains a considerable fraction of Pb-K$_\alpha$ transitions, which cannot be completely suppressed by the coincidence method. The contamination with Pb-K$_\alpha$ transitions is not a big issue, since the Lyman transitions are concentrated in a narrow region, whereas the lead background is spread over the whole detector area. Graph 5.6 (b) shows the prompt TDC spectrum, where no clear peak can be found. Only after applying an energy condition with the Lyman-α transition energy to it, the peak for the Lyman transition is revealed. The region marked in red in the TDC spectrum is selected as coincidence condition, which has already been used in graph 5.6 (a).

After identifying the proper values for the energy and timing conditions, the 2D position spectra for the Lyman transitions could be generated and are shown in figure 5.7. Figures (a) and (b) are the 2D spectra for FOCAL 1 and FOCAL 2, respectively, and (c) and (d) are the corresponding projected graphs. Only the FOCAL 2 setup recorded the Lyman-β transitions, due to its slightly smaller distance from the optical axis. Since it was neither intended nor needed to record the Lyman-β transitions, it can be viewed as a nice bonus to demonstrate the high resolving power of the FOCAL spectrometer. A precise energy determination is not feasible due to the low statistics in the 2D spectra, and the large separation from the main calibration line. However, a result for it will be given below.

To account for the temporal drift of the setup mentioned in the previous section, the actual Yb γ-line position, at the time each single Lyman-α_1 photon was registered, was determined, by interpolating the data points in graph 5.5. By doing this for

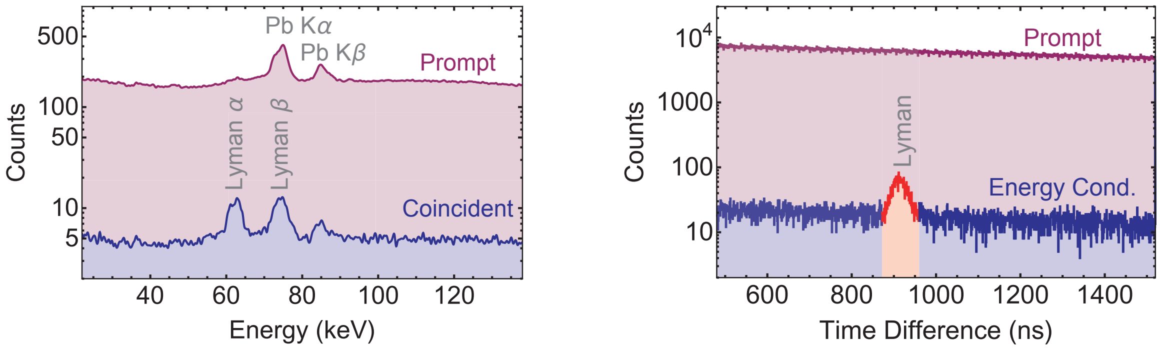

(a) Red: Prompt energy spectrum of a 2D germanium detector. Besides a huge background, and the characteristic radiation from the lead shielding, no further transitions can be seen. Blue: If the TDC coincident condition is applied, the background is reduced by a factor of 40, and the Lyman transitions can be unambiguously identified.

(b) Red: Prompt timing spectrum of the TDC. Unlike the case for the 150° germanium detector (see figure 4.15) no clear peak can be identified. This is due to the much lower detection efficiency of the FOCAL spectrometer. Blue: If the energy condition for the Lyman transitions is applied to the TDC spectrum, the TDC peak becomes clearly visible. The red shaded area marks the timing condition used to generate figure 5.6 (a).

Figure 5.6: Energy and timing spectrum for one 2D position-sensitive germanium detector.

every Lyman-α_1 photon, an effective Yb γ-line position could be defined, by means of a weighted average of all these positions. The uncertainty linked to this procedure was estimated by calculating the standard deviation of the distances between the actual positions, and a long term moving average of the interpolated temporal drift curve. The position of the Lyman transitions relative to the main Yb γ-line have been determined by fitting the TMF model 5.5, the results are compiled in table 5.3.

Transition	Line Separation Δz_d (μm)	
	FOCAL 1	FOCAL 2
Lyman-α_1	−35.2(5.1)(3.9)	−51.8(3.6)(7.2)
Lyman-α_2	−3 338.7(4.8)(4.3)	−3 352.9(5.4)(7.0)
Lyman-β_1	–	14 746.2(29.3)(7.2)
Lyman-β_2	–	14 037.2(35.7)(7.2)

Table 5.3: Line separation between the main ^{169}Yb-γ calibration line and the Lyman transitions. The minus signs indicate a shift to lower energies compared to the main Yb-γ calibration transition. The first bracket gives the statistical uncertainty, while the second one accounts for the temporal drift effect, which is larger for FOCAL 2. This is consistent with the greater drift shown in figure 5.5.

The first bracket specifies the statistical uncertainty of the Lyman photons, whereas the second bracket accounts for the temporal drift. The minus signs in the Lyman-α values indicate that the lines were situated at lower energies compared to the Yb-γ transition. Also it can be seen, that the temporal drift uncertainty for the FOCAL 2 spectrometer is considerably larger than that for FOCAL 1. This can be explained by the larger drift, which FOCAL 2 has experienced (see also graph 5.5).

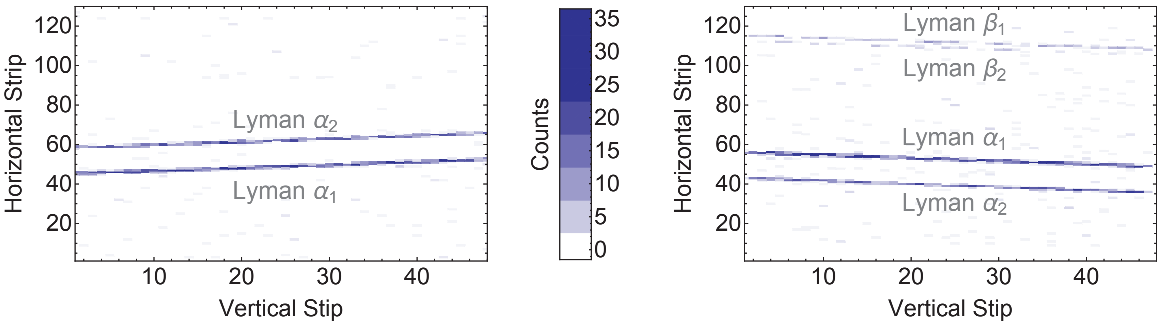

(a) Coincident 2D spectrum of the FOCAL 1 spectrometer.

(b) Coincident 2D spectrum of the FOCAL 2 spectrometer.

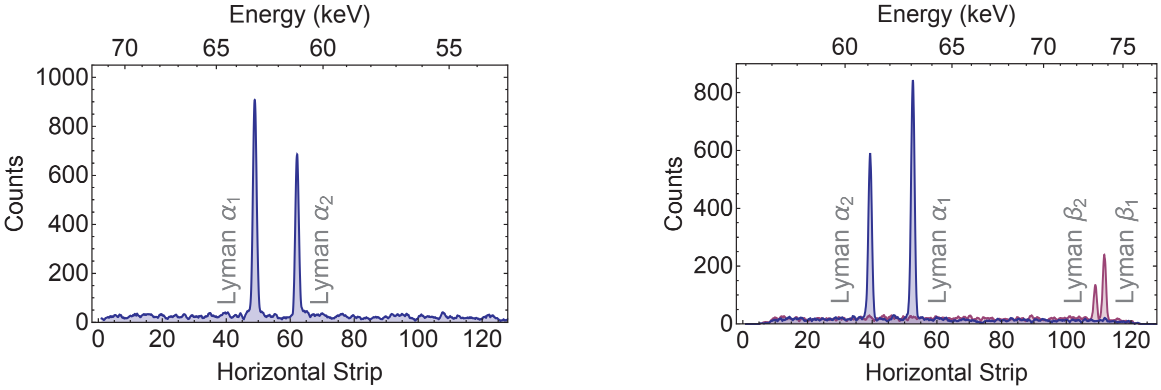

(c) Projected spectrum of the FOCAL 1 spectrometer.

(d) Projected spectrum of the FOCAL 2 spectrometer.

Figure 5.7: Accumulated spectra for the two FOCAL spectrometer arms.

5.2 Accompanying Experiments and Simulations

During the evaluation of the data it became necessary to perform several accompanying experiments, to determine parameters such as the gas-jet position or the detector crystal position, on which the FOCAL spectrometer critically depends. Besides these investigations, several *computer experiments* in the form of simulations have been conducted to study the behaviour of the spectrometer which are not accessible by other means.

5.2.1 Radius-of-Curvature Measurement

Before the beam time was started, one of the most important preparation steps was the bending of the two crystals, with the bending device. After bending the crystal a certain amount, an optical measurement technique was used to check if the desired bending radius of $R = 2\,000\,\mathrm{mm}$ was achieved, or if further bending was required. During and after the beam time, the bending radius was checked with two further, complementary methods, which will be explained in the following. The knowledge of the actual bending radius is of special interest, since it is closely connected via formula 5.8 with the dispersion D of the spectrometer.

The first technique applied was the optical method, where crystals mounted in the bending devices were fixed on a high-precision vertically movable table, and a laser beam was shone onto, and reflected off the polished crystal surface. By moving the crystal up– or downwards, also the reflected laser spot on a screen moved accordingly. This was recorded for several heights h_C on the crystal. From the distance between the crystal and the screen, and the height of the laser spot, the reflection angle α could be calculated, and the bending radius of the crystal was determined by fitting the formula

$$\sin(\alpha) = \frac{h_C}{R} \tag{5.10}$$

to the data points. This method also allowed to check the twist of the crystal around its vertical axis, which would have resulted in an additional movement in the horizontal direction of the laser spot. The twist of the crystal was corrected by a special micrometer screw shown in figure 4.7, pointing into the paper plane. The crystals adjusted by this method were transported to the crystal assembly support of the FOCAL setup in the ESR cave (see figure 4.3).

The second method to measure the bending radius can be performed within the FOCAL assembly, with the help of the calibration source. According to the approximate formula 5.8, the dispersion D_{th} and the Rowland circle radius R are closely connected. However, this equation is only valid if the spectrometer is perfectly aligned, meaning that the detector-crystal spacing d_{DC} is equal to the actual crystal bending radius R, as already mentioned in section 2.2.6. If the crystal bending radius deviates from this set-point, an x-ray line with wavelength λ will be found on a different position z_d, as predicted by equation 4.4, due to a modified dispersion D. If the dispersion is known (measured), the actual bending radius can be calculated. For that purpose the following relation on the basis of the intercept theorem and figure 2.11 can be formulated

$$\frac{z_c + z_R}{R} = \frac{z_c + z_d}{d_{DC}} \tag{5.11}$$

where z_c is the height of the x-ray footprint on the crystal, and z_R the distance of the x-ray from the optical axis, at a position R from the crystal (assuming $R \neq d_{DC}$). An approximate formula for the footprint height z_c on the (symmetric) crystal is given by

$$z_c = R \, \frac{d_{SC}}{R + d_{SC}} \, \frac{\lambda}{2\, d_{hkl}} \tag{5.12}$$

with the source-crystal separation d_{SC} [Beye04]. Having noted this, equation 5.11 can be solved for λ

$$\lambda = \frac{2\, d_{hkl}\, (d_{SC} + R)}{2\, d_{SC}\, d_{DC} - d_{SC}\, R + d_{DC}\, R} \, z_d \tag{5.13}$$

Since the dispersion is given by $D = d\lambda/dz_d$ (formula 5.8), equation 5.13 is derived with respect to z_d, and solved for R. To indicate that this is the theoretical solution a '*th*' is added

$$R_{th} = \frac{2\,d_{SC}(D\,d_{DC} - d_{hkl})}{2\,d_{hkl} + D\,(d_{SC} - d_{DC})} \tag{5.14}$$

This equation roughly gives the functional dependence of the crystal bending radius from the dispersion. Since all equations, which are used to derive formula 5.14, are approximations to motivate the physical relation between the various parameters, it *cannot* be used to determine the experimental curvature radius R from the measured dispersions in table 5.2. For this task, a dedicated three-dimensional ray-tracing simulation utilising the MacRay package has been conducted [Beye16], which incorporates the geometrical dimensions of the spectrometer, as well as the fact that one spectrometer is in the lower (FOCAL 1), and the other spectrometer is in the upper (FOCAL 2) observation position. Details concerning the ray tracing simulations are treated in section 5.2.6. The results of these simulations are described by a second order polynomial

$$R_{\text{MacRay}}(D) = m_0 + m_1\,D + m_2\,D^2 \tag{5.15}$$

with numerical parameters $m_0 \dots m_2$, which are listed in table 5.4. For comparison reasons the approximate formula 5.14 has been developed in a series expansion, and numerical values for the FOCAL case have been inserted. The result of this procedure can also be found in table 5.4, which are similar to the results from the simulation.

Parameter	FOCAL 1	FOCAL 2	R_{th}
m_0 (m)	12.6212	12.6665	12.7
m_1 (m)	-1.5677×10^{11}	-1.56517×10^{11}	-1.57×10^{11}
m_2 (m)	5.30278×10^{20}	5.27214×10^{20}	5.25×10^{20}

Table 5.4: Numerical values for the polynomial $R_{\text{MacRay}}(D)$ 5.15 for both FOCAL spectrometers as obtained by the MacRay simulations. For comparison reasons, the approximate theoretical formula R_{th} 5.14 has been developed in a series expansion, and the resulting parameters are listed in the last column.

With the polynomial $R_{\text{MacRay}}(D)$ and the measured dispersions D in table 5.2, the local curvature radius in the vicinity of the main Yb-γ calibration line can be calculated. The results are shown in figure 5.9.

The third method applied to determine the curvature radius was a dedicated test beam time at the European Synchrotron Radiation Facility (ESRF) in Grenoble, France, where highly intense and collimated x-ray beams can be provided. These measurements were performed directly after the beam time at GSI, to avoid systematic deviations due to a long pause between the experiments. The two crystals have been transported to the ESRF beam line BM05, where numerous actuators and detectors, mounted on an optical table, were available. The setup for the measurements can be seen in figure 5.8.

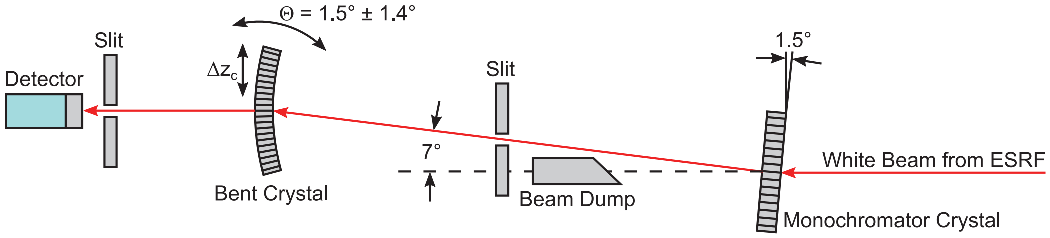

Figure 5.8: Setup at the ESRF beam line BM05 to measure the radius of curvature for the two FOCAL crystals. The white x-ray beam from the ESRF enters from the right, where it is diffracted by the monochromator crystal. Only x rays with an energy of 53 keV encounter the bent crystal, the rest is disposed at a beam dump. The angle Θ of the second crystal is varied, and the count rate in the detector is recorded. This procedure is repeated for several heights z_c on the crystal.

The white x-ray beam from the synchrotron enters the experimental cave from the right. “White” means that the x-ray spectrum consists of a broad distribution, instead of a single selected wavelength, since the monochromatisation was done in the cave, by means of a flat crystal. The wavelength of the diffracted beam could be selected by tuning the (Bragg-) angle at the monochromator crystal, resulting in an energy of 53 keV for the used settings. The remaining part of the beam traversed the crystal unchanged, and was disposed at the beam dump. One of the bent FOCAL crystals from the experiment was fixed on a tiltable and vertical movable stage, which was positioned in the beam path of the diffracted beam. For several heights z_c on the crystal, an angle range of $\Delta\Theta = \pm 1.4°$ was scanned, and the count rate at an x-ray detector was recorded as a function of Θ. If the Bragg condition was fulfilled, the x-ray detector registered a clear increase in intensity. Since these rocking curves have been recorded for many positions in the range $\Delta z_c = -40\,\text{mm} \ldots +40\,\text{mm}$, the curvature radius could be determined for the whole interesting region around the crystal centre at $z_c = 0\,\text{mm}$, for both crystals.

Figure 5.9 represents the findings for all three techniques. It has to be noted that the “error bars” for the optical and ESRF measurements indicate rather a curvature radius interval over the averaged section on the crystal, than an actual error. The error bar for the FOCAL measurement is the smallest, since it is the only measurement, which represents a local, not averaged, curvature radius.

5.2.2 Gas-Jet Target Position Determination

As already stated in section 4.1, the purpose of using two spectrometer arms opposing each other is to correct for the Doppler effect. If the relativistically moving source is located between the two spectrometers, the rest-frame transition wavelength can be

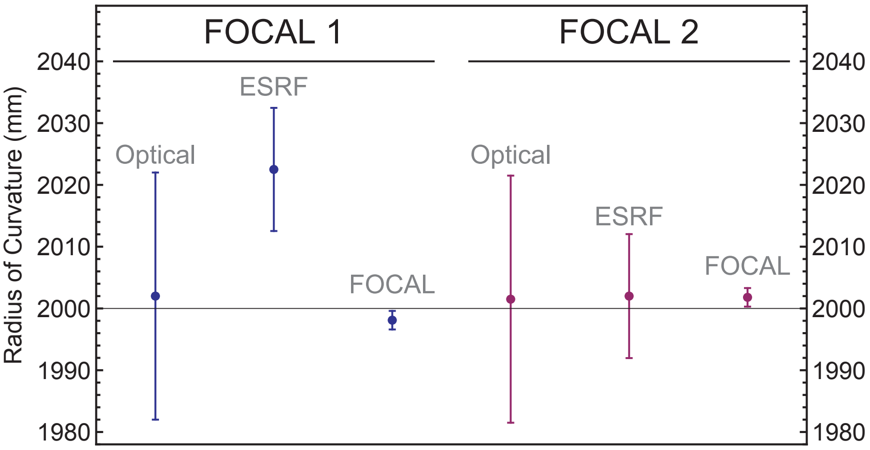

Figure 5.9: Results of the radius of curvature measurements for the different applied methods. The "error bars" represent a bending radius interval averaged over a certain height, rather than an uncertainty [Beye13].

calculated by applying formula 4.2. In a real-world scenario, the x-ray source may not coincide exactly with the line of sight, leading to correction terms in formula 4.2. This fact does not make the two-arms technique redundant, but it requires more effort to characterise the whole assembly. The deviations $\Delta x_{1,2}$ from the ideal case are shown in figure 5.10, and consist of two contributions: *(i)* The possible misalignment of the gas-jet target, and *(ii)* the actual position of the 2D detector crystals inside their housings. The measurement of the gas-jet position is treated in this section, while the detector crystal measurement is treated in the next section.

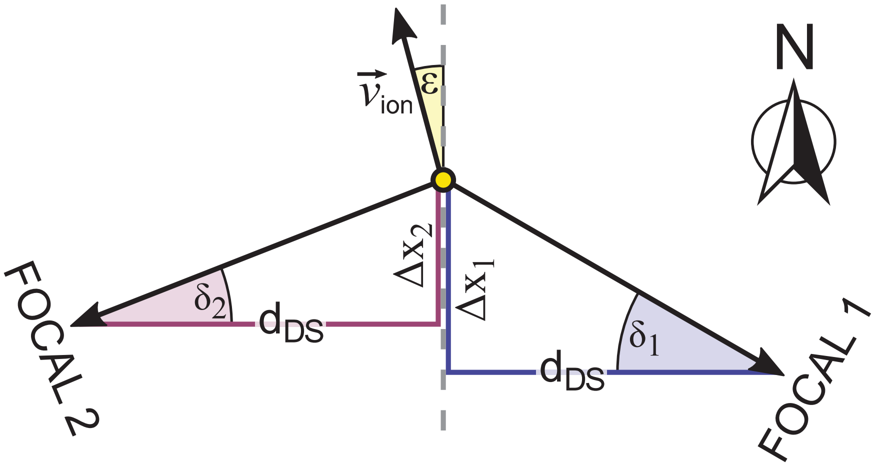

Figure 5.10: Modified Doppler cancelling scheme, if the moving source is not exactly located on one common line of sight with the two detectors (*cf.* figure 4.2)

The gas jet can deviate in two main directions from its nominal value: In the East–West (EW) and the North–South (NS) direction. The cardinal directions for the ESR are indicated by the compass rose in figure 3.3, and influence the FOCAL result as follows: A shift in the EW-direction displaces the target parallel to the line of sight. The angle enclosed by the two spectrometer arms and the source still is 180°, making a shift in this direction *uncritical* for the FOCAL experiment. However, a shift in the NS direction would reduce the enclosed angle to $180^\circ - (\delta_1 + \delta_2)$, and formula 4.2 is no longer applicable. Therefore, a deviation in this direction is *critical* for the experiment. A more general formula can be derived in the same manner as sketched in section 4.1 and is given by

$$\lambda_1 + \lambda_2 = \gamma\,\lambda_0\,\left[2 + \beta\,(\sin(\delta_1 - \varepsilon) + \sin(\delta_2 + \varepsilon))\right] \tag{5.16}$$

with $\delta_{1,2}$ being the deviation angles, which are given by $\tan(\delta_{1,2}) = \Delta x_{1,2}/d_{\mathrm{DS}}$, the detector–source spacing d_{DS} and the ion beam deviation angle ε, already known from section 4.1. This new formula now depends on the angle ε, but it appears with different signs compensating its influence almost completely.

To measure the gas target part of $\Delta x_{1,2}$, a dedicated measurement campaign, following the experiment beam time, had to be conducted [Gass15]. The main challenge to overcome was the low density of just 10^{12} atoms/cm^3 inside the gas jet, which would normally be defined as *high vacuum*. The measurement technique, which was developed and used, was a mechanical gas-scatter probe, which consisted of an aluminium frame on which a 0.6 mm thin wire was tensed (see figure 5.11).

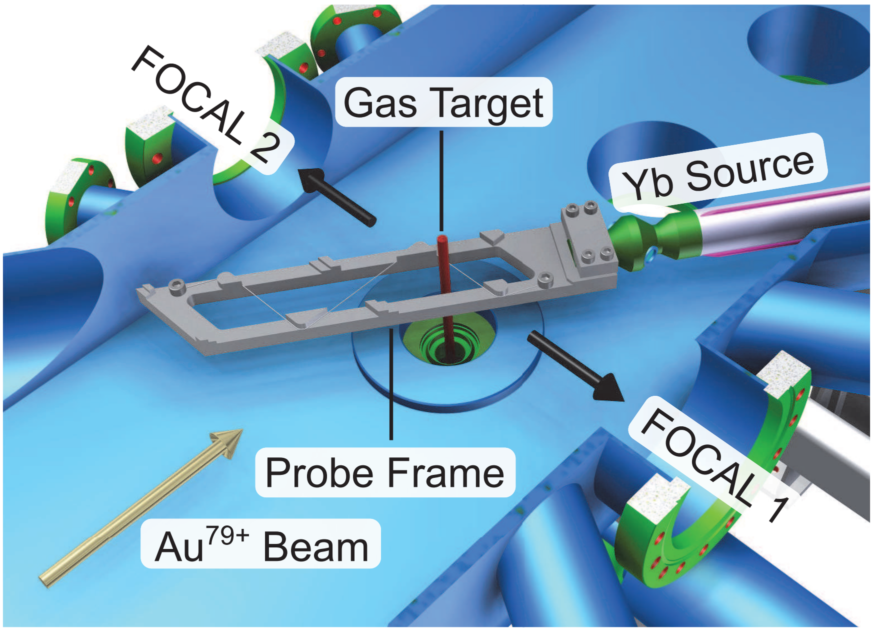

Figure 5.11: Probe frame for determining the gas-jet position and density profile in the direction of the ion beam, and perpendicular to it.

The wire was fixed on the frame, in a zigzag manner, with sections being parallel or perpendicular to the ion beam direction. To move the frame through the gas jet, it was mounted at the tip of the Yb-source cantilever arm, while its position was monitored by a high-precision linear encoder. To relate the position of the frame with the FOCAL coordinate system, the same telescope supports were used, to aim for three dedicated fiducial marks, situated on the aluminium frame. If the gas jet hit the wire, the fraction of atoms proportional to the intersecting area was scattered into the volume of the ESR target chamber, leading to a rise of pressure in the ring vacuum.

This pressure rise was measured by a highly-sensitive mass spectrometer, that was adjusted to the probe gas krypton. With this method, almost background-free profiles could be recorded, for both directions (NS and EW). The barycentre of the profiles was determined by fitting a model function, motivated by the following considerations: The density profile of the gas jet is defined by several circular skimmers, located in the gas inlet chamber (see figure 3.6), hence, the gas-jet also has a circular shape. The amount of scattered atoms is proportional to the intersecting length of the wire with the gas-jet. This leads to the following formula

$$\Delta p(x,\, r) \propto \begin{cases} 2\sqrt{r^2 - x^2} & |x| \leq r \\ 0 & \text{otherwise} \end{cases} \tag{5.17}$$

with x being the position and r the radius of the gas-jet. From this formula follows that the full width at half maximum is given by $\mathrm{FWHM} = \sqrt{3}\, r$. For actual fitting, an amplitude, a background, and a position shift in the x-direction is added. Figure 5.12 shows an example of such a measurement (red points) in the critical NS direction, together with the best fit of the model function (blue curve). The arrow marks the centre obtained by the fit, where the negative value stands for a shift to the North.

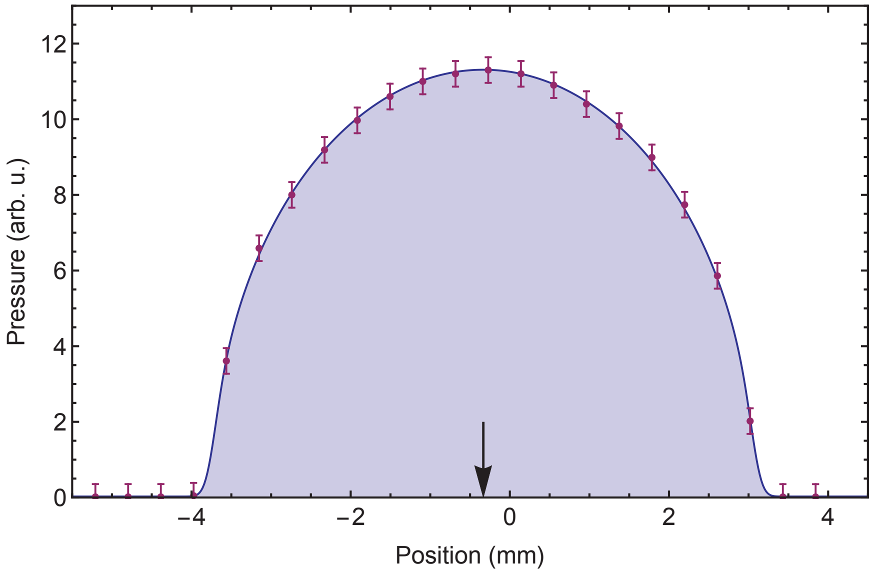

Figure 5.12: Measured pressure rise in the ESR target chamber as a function of the wire position. The arrow marks the barycentre of the distribution, which is slightly shifted to the North (= negative position values).

Table 5.5 summarises the results for both measurement directions. The letter N (W) in the column "Position" indicates a shift to the North (West). The relatively large uncertainty for the position, of about 0.3 mm, is completely determined by the optical alignment, which scattered by this value at repetition.

Direction	Label	Position (mm)	Radius r (mm)	FWHM (mm)
North–South	$\Delta x^{\mathrm{NS}}_{\text{Gas-Jet}}$	0.25(30) N	3.11(4)	5.39(7)
East–West	$\Delta y^{\mathrm{EW}}_{\text{Gas-Jet}}$	0.43(30) W	3.19(4)	5.53(7)

Table 5.5: Measured positions and gas-jet radii in the two main cardinal directions [Gass15].

5.2.3 Detector Crystal Position Measurement

The position of the detector crystal in the housing of the 2D germanium detector was assumed to be perfectly centred during the assembly phase of the experiment. To verify this, a dedicated measurement campaign was conducted, which consisted of two parts: In the first part, the position of the crystal relative to the beryllium x-ray window of the detector was measured, at the ESRF in Grenoble. In a second step, the x-ray window distance relative to the reference edge, used during the setup phase of the FOCAL experiment, was determined. By combining these two results with the findings from the gas target measurement, the total value for displacement $\Delta x_{1,2}$ was determined.

The first part of this measurement campaign took place at the ESRF, where a well collimated and intense photon beam was available. The detector was fixed on a movable table pointing directly into the $1\,\mathrm{mm} \times 1\,\mathrm{mm}$ small x-ray beam, coming from the synchrotron. The monochromators of the beam line were tuned to 63.1 keV, which corresponds to the energy of the main calibration line, in order to avoid any systematic deviations. The position of the x-ray beam on the detector was determined with photosensitive paper, which darkens when being irradiated. An optical telescope was adjusted to the dark spot, and the detector was moved until an edge of the beryllium window fell in line with the telescope cross hairs. By recording the travel of the movable table, the position of the x-ray beam could be related to this characteristic point of the outer detector housing. After establishing a reliable coordinate system, an arbitrary vertical strip was scanned, with a step width of $100\,\mu$m. At the same time, the trigger rate of this strip was recorded, leading to the profile shown in figure 5.13. The origin of the position axis indicates the expected centre for this strip.

Since the strip response function and the x-ray beam profile can be modelled by a rectangular function, the convolution results in a trapezoid curve, as already stated in section 5.1.2. The trapezoid shape shown in figure 5.13 fits the data points well, and the obtained centre of $\Delta x^{1}_{\mathrm{ESRF}} = -0.25(30)\,\mathrm{mm}$ for FOCAL 1 is marked by an arrow. The negative sign indicates a shift to the North (in terms of the ESR coordinate system), and the relatively large uncertainty is again completely determined by the optical alignment procedure. Unfortunately, only the crystal position of the detector used for FOCAL 1 could be measured, since the crystal for the other detector was changed in the meantime. Despite of this fact, an estimate for the accuracy of the centring could be obtained, and the value for FOCAL 2 is set, with an increased uncertainty, to $\Delta x^{2}_{\mathrm{ESRF}} = 0.00(60)\,\mathrm{mm}$.

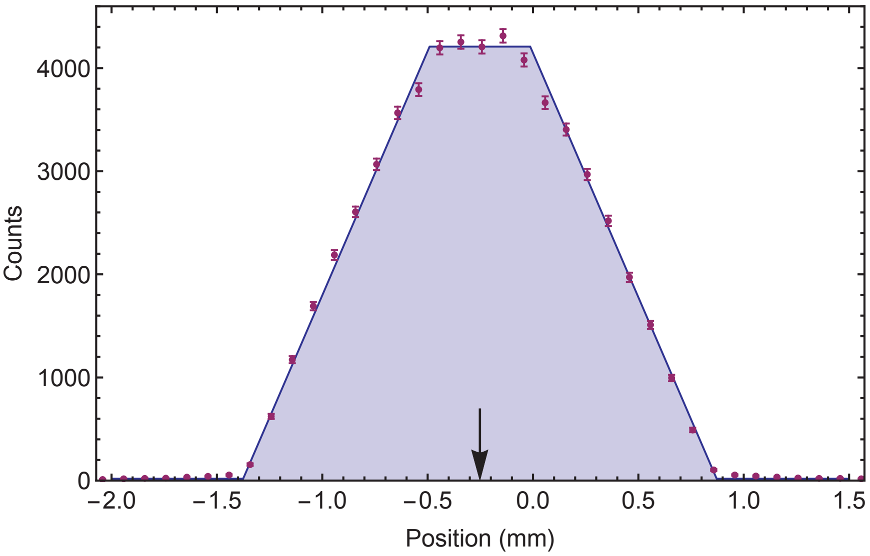

Figure 5.13: Recorded x-ray counts as a function of the strip position for FOCAL 1. The arrow marks the barycentre of the distribution, which is slightly shifted to the North (= negative position values).

The second part of the position measurement could be conducted in the technology laboratory at GSI. For this purpose, both detectors were placed on a flat polished granite plate and the distance between the beryllium window and the reference edge was measured mechanically by means of steel squares and vernier calliper measurements.

The determined shifts are listed in table 5.6 and the sum of these values add to the total detector crystal position shift Δx_{Det}.

Detector	Δx_{ESRF} (mm)	Δx_{GSI} (mm)	Δx_{Det} (mm)
FOCAL 1	0.25(30) N	1.66(30) N	**1.91(42) N**
FOCAL 2	0.00(60)	0.13(30) S	**0.13(67) S**

Table 5.6: Detector crystal position shifts relative the assumed centre during the beam time 2012.

A detector crystal which is shifted to the North is exposed to higher-energetic x rays due to the Doppler effect. According to the findings in table 5.6 it can be supposed that FOCAL 1 would register energetically richer radiation compared to FOCAL 2. This assumption is supported by the results listed in table 5.3, where the line separations Δz_d for the Lyman-α radiation is systematically smaller for FOCAL 1 compared to FOCAL 2, leading to higher laboratory frame transition energies for that spectrometer.

5.2.4 The Ion Beam Velocity

The Doppler equation 4.1 connects the known (measured) laboratory-frame wavelength λ_{Lab} of a transition, with the following three parameters: The velocity, represented by the Lorentz factor γ (and hence also β), the observation angle θ and the desired rest-frame wavelength λ_0. By making use of the Doppler cancelling aspect of the two opposing crystal spectrometers, the angle dependency could be removed, resulting in equation 4.2. However, this equation still depends on the ion beam velocity via γ, which has to be determined separately. In section 3.4.1 it has already been stated, that the velocity of a stored beam is defined by the electron beam velocity in the electron cooler, which, in turn, depends on the applied voltage U_{Cool} accelerating the electrons. The γ-factor of a single electron, being accelerated by a voltage U_{Cool}, is given by

$$\gamma = 1 + \frac{e\,U_{\text{Cool}}}{m_e\,c^2} \tag{5.18}$$

with the elementary charge e. The applied voltage during the experiment was $U_{\text{Set}} = 68\,390\,\text{V}$ to meet the velocity of the decelerated ion of $E_{kin} \approx 124.8\,\text{MeV/u}$. However, this voltage is not equal to the voltage U_{Cool}, which is experienced by the electron and has to be corrected by a voltage U_{Corr} consisting of two contributions.

The first correction is called the *space charge effect*, termed U_{SC}. It is caused by the fact, that not a single electron, but rather an intense beam of electrons is accelerated continuously. In contrast to a single electron, which only experiences the accelerating electric field, an ensemble of electrons in addition interacts via the Coulomb force with all the other electrons as well. The charge distribution of the electrons thus leads to a decelerating electrostatic potential U_{SC}, which increases with the number of electrons in the beam, which is proportional to the electron current I_e. For the ESR electron cooler, U_{SC} can be estimated by

$$U_{\text{SC}} \approx 0.112\,15 \times \frac{I_e\ [\text{mA}]}{\beta} \tag{5.19}$$

which for $I_e = 200\,\text{mA}$ and $\beta \approx 0.471$ results in $U_{\text{SC}} \approx 48\,\text{V}$ [Bran00]. During the beam time, the space charge effect was also measured to be $U_{\text{SC}} = 48\,\text{V}$.

The second effect that alters the accelerating voltage, is a systematic deviation between the voltage generated by the high-voltage terminal, compared to the voltage measured using a well calibrated high voltage divider. Unfortunately, the last calibration of the high voltage terminal of the ESR was done in 2001, and the drift of the cooler voltage since then is a major contribution to the total experimental uncertainty. Right after the FOCAL beam time, in April/May 2012, Matthias Lochmann conducted a laser spectroscopy experiment on the ground state hyperfine structure of Li-like bismuth, being very sensitive on the actual ion beam velocity. In his thesis [Loch13] he treats this systematic effect in great detail, and the further discussion relies on his findings. The estimated voltage shift increases the accelerating voltage by $U_{\text{Cal}} = 63(35)\,\text{V}$, with a quite substantial uncertainty of 35 V. The high-voltage terminal itself is capable to control the voltage with a precision better than 10 V, but, due to the long time between the calibration and the FOCAL run, this value had to be increased [Nrte15]. A detailed discussion of the uncertainty connected to this effect can be reduced in a future run is given in the sections 6.1.3 and 6.3.

After having discussed the two major contributions that change the accelerating potential, and hence the ion beam velocity, the cooler voltage U_{Cool} is given by

$$U_{\text{Cool}} = U_{\text{Set}} + U_{\text{Corr}} \tag{5.20}$$

with the correction voltage $U_{\text{Corr}} = U_{\text{Cal}} - U_{\text{SC}}$. The results and uncertainty estimation of this evaluation is given in table 5.7.

Parameter	Value
U_{Set}	68 390 V
U_{Corr}	15(35) V
U_{Cool}	68 405(35) V
γ	1.133 865(68)
β	0.471 36(10)
E_{kin}	124.695(64) MeV/u

Table 5.7: Electron cooler voltage and the derived ion beam velocity parameters.

5.2.5 Calculation of Decay Cascades

As already explained in section 4.2 and shown in figure 4.13, the $2p_{3/2}$ state is the only energetically isolated excited state in hydrogen-like gold. All other transitions stemming from different states cannot be resolved separately, with the resolution available with FOCAL. Due to this purity, the Lyman-α_1 transition has been chosen as the main experimental observable. However, it would be preferable to extract information about the Lamb shift from other recorded transitions, especially from the strong Lyman-α_2, as well. For such an investigation, the mixing ratio between the $2\,p_{1/2} \rightarrow 1\,s_{1/2}$ and the $2\,s_{1/2} \rightarrow 1\,s_{1/2}$ transitions has to be determined. Unfortunately, it is not sufficient to calculate the initial population of both excited states during the capture process, since cascading transitions from higher excited states have also to be taken into account. An electron which is captured *e.g.* into the $3\,s_{1/2}$ can either decay directly to the ground state via an M1 transition, or feed the $2\,p_{1/2}$ state via an E1 transition (see figure 4.13). Recursively, the same can happen to the $3\,s_{1/2}$ and other higher excited states. To perform a cascade simulation, two input data sets are needed: *(i)* the initial population of each atomic state, and *(ii)* the transition rate between each excited state to each other state, in order to calculate the branching ratios.

The initial population has been calculated from J.P. Rozet from the Institut des NanoSciences de Paris with the non-relativistic ETACHA code [Roze96] for the beam time parameters of the 2012 run. The program calculates the capture cross section for each (n, ℓ)-state up to $n = 10$. The result of this calculation can be seen in figure

5.14, where the thickness of the black horizontal lines scales logarithmically with the initial occupation. It can be seen that high (n, ℓ) states are less frequently occupied than *e.g.* the $2\,p_{3/2}$. The ratio between the $2\,p_{3/2}$ and the $10\,p_{3/2}$ is ≈ 35. Whereas the ratio between the $1\,s_{1/2}$ and the $10\,\ell_{1/2}$ is even ≈ 580. Therefore, one can be sure that the most important states have been taken into account, although it would be preferable to have even higher states available. Due to the non-relativistic treatment of the collisional process and the complexity of the problem, an uncertainty of 50 % has been attributed to the calculated values.

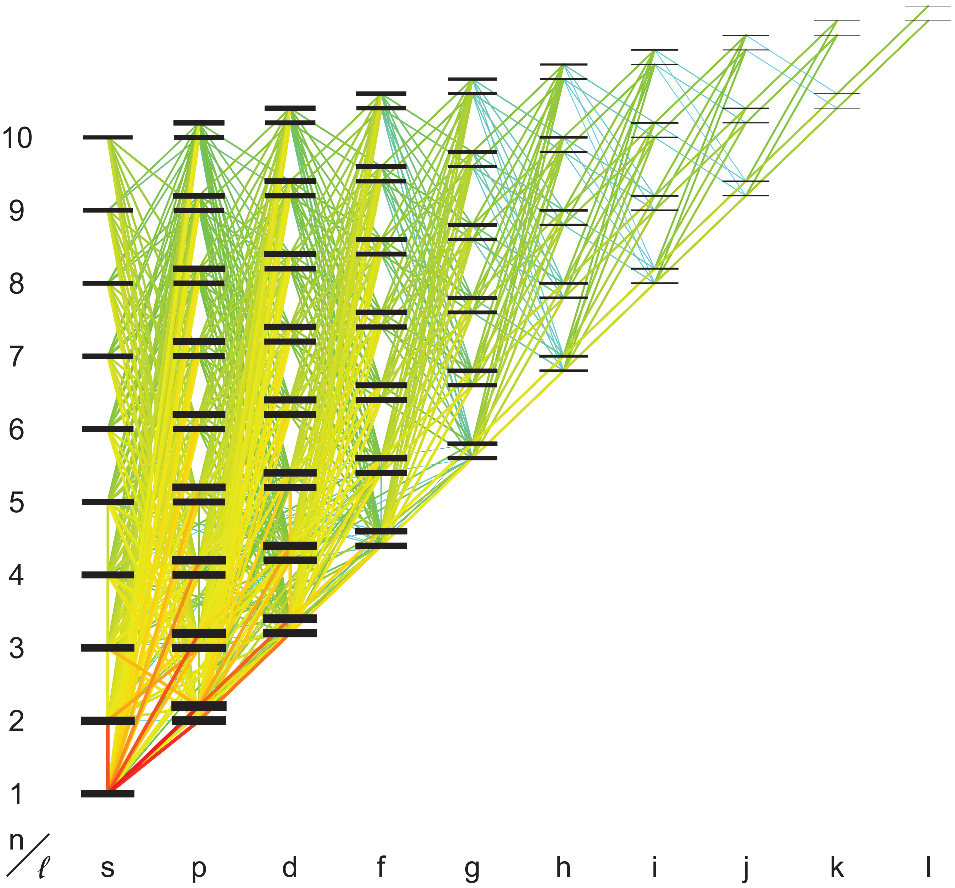

Figure 5.14: Cascade calculation for completely ionised gold, capturing an electron at 124.6 MeV/u form an argon gas target. The thickness of the black bars indicates the initial occupation of each state, which scales logarithmically. This is the result of the ETACHA calculation [Roze96]. All possible transitions are shown as straight lines, connecting one state with the other. Also here the (logarithmic) thickness of the line indicates how often a certain transition occurs. In addition to the thickness, also the colour encodes the number of occurring transitions, from often (red) to seldom (blue).

The transition rates have been calculated in the same way as described in [Stoh97, Stoh16]. With the help of the General-purpose Relativistic Atomic Structure Program GRASP [Dyal89], which utilises the multiconfiguration Dirac-Fock method (MCDF) [Gran88], it is possible to calculate the transition rates between arbitrary states for all atoms or ions in any desired charge state.

After having both input sets available, a program calculating the cascade was written. Since only 100 states making about 700 different transitions had to be taken into account, a completely analytical approach was chosen instead of a time-discrete simulation [Reus06], which is suitable when excited states up to $n = 120$ have to be considered. The advantages of an analytical calculation is that time does not need to be divided into discrete steps, with an arbitrary selected step width. Choosing a too small step size results in long simulation times, choosing too long steps sizes will result in a simulation which is not able to follow the fastest transitions, and hence reduces the accuracy of the result. The step width of an analytical solution is by definition infinitesimal, hence yielding exact results. Therefore, it is called cascade *calculation* rather than *simulation*.

In the following, the decay formula describing the time-dependent occupation $n(t)$ of an arbitrary state will be derived. This state has some donator states, lying energetically above it, and acceptor states, lying energetically below it. The transition between two states is described by the transition rate Γ_i, which is positive for a donator, and negative for an acceptor state. The differential equation for the time-dependent occupation is given by

$$\frac{\mathrm{d}n(t)}{\mathrm{d}t} = n_1(t)\,\Gamma_1 + n_2(t)\,\Gamma_2 + \cdots = \sum_i n_i(t)\,\Gamma_i \tag{5.21}$$

where the sum runs over all donator and acceptor states i. This differential equation can be solved with the initial condition $n(0) = n_0$, being the initial occupation of this state, before any transition, *i.e.* the ETACHA result. The solution is called decay equation and is given by

$$n(t) = e^{-\Gamma_{\mathrm{ges}}\,t}\left[n_0 + \int_0^t e^{+\Gamma_{\mathrm{ges}}\,\tau}\left(\sum_{\substack{i\\ \Gamma_i>0}} n_i(\tau)\,\Gamma_i\right)\,d\tau\right] \tag{5.22}$$

with Γ_{ges} being the sum of all acceptor states transition rates ($\Gamma_i < 0$), since this is the rate $n(t)$ gets depopulated. The sum in the integral runs over all donator states ($\Gamma_i > 0$), and is therefore responsible for feeding the observed state. If there are no feeding donator states then the sum is zero, resulting in a vanishing integral and one obtains $n(t) = n_0\,e^{-\Gamma_{\mathrm{ges}}\,t}$, which is the usual exponential decay law. A cascade calculation for an arbitrary state is conducted, by putting in the characteristic input values (n_0, Γ_{ges}), and evaluating the sum in the integral. If there are no feeding states then the calculation is finished. Otherwise, one has to apply the decay formula $n(t)$ for each $n_i(t)$ recursively. A decay formula $n(t)$ obtained in this manner describes the exact temporal behaviour of a certain state, and consists normally of many dozens of exponential functions. The expected energy for the Lyman-α_2 transition is given by the weighted mean of both transition energies, with the weighting factors derived with the cascade calculation. To get the weighting factors, one calculates the number of transitions for both involved states via

$$N_i = \int_0^\infty n(t)\,\Gamma_i\,dt \tag{5.23}$$

and normalises the sum of N_i to 100 %. Calculations performed for the Lyman-α_2 yield $N_{2p_{1/2}} = \int_0^\infty n_{2p_{1/2}}(t)\,\Gamma_{2p_{1/2}\to 1s_{1/2}}\,dt = 61.5\,\%$ and $N_{2s_{1/2}} = 38.5\,\%$. By taking the theoretical transition energies, given in table 2.2, one obtains $E_{Ly-\alpha_2} = 69\,345.0\,\mathrm{eV}$. Since the cross sections calculated with ETACHA are afflicted with uncertainties, the cascade calculation have been performed many times, with disturbed values for the cross sections. The obtained expectation energy scattered with a standard deviation of 2.3 eV. Similar calculations were performed for the Lyman-β transitions, the results are compiled in table 5.8 and illustrated graphically in figure 5.15.

Transition	Contributing States (%)	Cascade Energy (eV)
Lyman-α_2	$2\,p_{1/2}$ 61.5(7.3), $2\,s_{1/2}$ 38.5(7.3)	69 345.0(2.3)
Lyman-β_1	$3\,p_{3/2}$ 96.9(1.1), $3\,d_{5/2}$ 1.66(64), $3\,d_{3/2}$ 1.43(53)	83 550.7(1.2)
Lyman-β_2	$3\,p_{1/2}$ 94.6(1.9), $3\,s_{1/2}$ 4.4(1.9)	82 881.3(3)

Table 5.8: Theoretical transition energies due to the blending of neighbouring states, according to the cascade calculation.

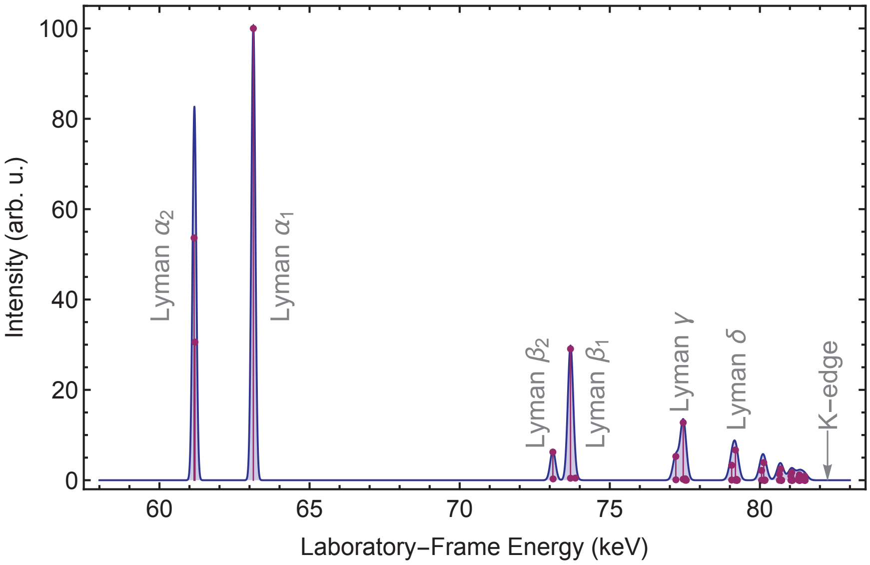

Figure 5.15: Calculated intensity for each transition at the corresponding energy (red points) and the corresponding x-ray spectrum, convoluted with the FOCAL resolution (blue curve).

In addition to the cascade energies listed in table 5.8, also the temporal emission of Lyman radiation could be studied. This is important if some slow transitions delay the depopulation in such a way, that the ion travelled a substantial distance in the meantime, leading to different Doppler corrections, and hence asymmetric peaks, as reported in [Beye95b, Gumb05]. With the help of the cascade program, it could be shown that almost all down-charged ions are in the ground state after less than 10^{-15} s, which is much too fast to alter the result significantly.

5.2.6 Raytracing Simulation of the Spectrometer

In the course of the data evaluation, a three-dimensional ray-tracing program for x rays has been written, to study the influence of various physical effects in a well-defined *computer experiment*. In its functionality, the program behaves similar to the MacRay code, which has been written by H.F. Beyer [Beye97a]. Both programs were used side-by-side during the experiment analysis.

The program simulates either resting or moving sources, which emit radiation in a random direction. If a ray hits the bent FOCAL crystal, it is reflected with the probability given by the rocking curve, which has been pre-calculated with the help of the XOP package [Rio97, Rio11]. If the simulated photon is diffracted by the crystal, it continues its path until it hits the germanium crystal of the position sensitive detector, where it stops at a random depth, following the Beer-Lambert law.

With the help of the ray tracer, it could be proven that the asymmetry of the lines is caused by the finite photon absorption length, in the germanium crystal of the 2D detector, in combination with a non-perpendicular incident angle, as already stated in section 5.1.2. The result of two simulations with a moving (Lyman-α_1) and a source (Yb-γ) at rest are shown in graph 5.16. Although the simulation is fully three-dimensional, the graph shows only a projection onto the entrance surface area of the germanium crystal. This is due to the following two reasons: *(i)* A projection is much easier perceived for a human reader, and *(ii)* the 2D germanium detector is only capable to record the projected line shape. For both lines, especially for the source at rest, the asymmetry to large distances from the optical axis (lower transition energies) can be seen, manifested in a lower point density in this region. The simulation is also able to reproduce the Doppler tilt for the moving source, which moves in this example from the left to the right.

The MacRay code was also used to generate the crystal bending radius versus the spectrometer dispersion curves, given by formula 5.15 and table 5.4. This was necessary to determine the bending radii of the FOCAL crystal, which would otherwise lead to large deviations, if the approximate formula 5.14 had been used.

5.3 Final Value Determination

In the previous sections, the main data analysis with the line profile fitting and the accompanying experiments have been treated in detail. In this paragraph, the final value for the 1s Lamb shift in hydrogen-like gold, including all corrections, will be derived. The evaluation follows the entries in table 5.9 from top to bottom, illustrating the derivations exemplary on the Lyman-α_1 transition. A detailed discussion of the uncertainties and how they can be minimised in a future FOCAL run is given in the next chapter.

The evaluation of the final value starts with the main FOCAL equation 4.2, which

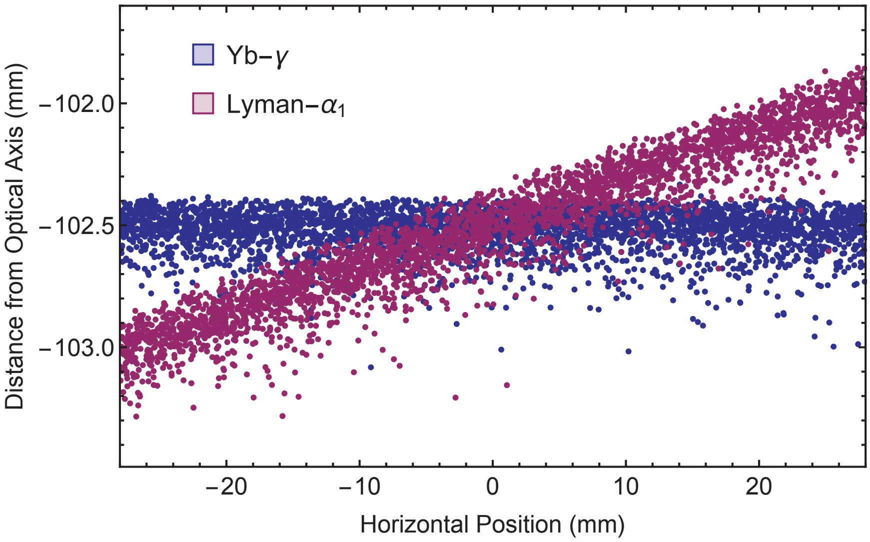

Figure 5.16: Simulated x-ray events as recorded by a detector (without rasterisation). Each blue point corresponds to one ^{169}Yb-γ photon event. Since this x-ray source is at rest, the line is orientated horizontally. It can also be seen that above the main line no photons are registered. However, below it, a few events can be found, with decreasing density. These photons are responsible for the low energy tail in figure 5.3. The red points have been simulated from a fast source, moving from the left to the right. Due to the high velocity, the line experiences the already mentioned Doppler tilt.

does not include any corrections from the accompanying experiments. The only measured input values, which are used at this point, are the spacings Δz_d between the Lyman-α_1 and the main Yb-γ calibration line, summarised in table 5.3. To derive the individual $\lambda^{\text{Ly-}\alpha_1}_{F1,F2}$ for each spectrometer (F1, F2), formula 2.23 has been used. For the dispersion, the approximate theoretical result $D_{th} = 1.92 \times 10^{-10}$, given by equation 5.8, has been used. The last remaining input parameter is the velocity of the ion beam, which is calculated by setting $U_{\text{Cool}} = U_{\text{Set}}$ in formula 5.18, with the voltage $U_{\text{Set}} = 68\,390\,\text{V}$, given in table 5.7. The obtained rest frame wavelength $\lambda_0^{\text{Ly-}\alpha_1}$ is converted to an energy via $E'_{\text{Ly-}\alpha_1} = hc/\lambda_0^{\text{Ly-}\alpha_1}$, which is more convenient for x-ray radiation. The resulting transition energy $E'_{\text{Ly-}\alpha_1} = 71\,537.8(2.2)\,\text{eV}$ is up to now only afflicted with uncertainties due to the statistical position uncertainty in Δz_d, and the (negligible) Yb-γ calibration line uncertainty of 40 meV.

The corrections are taken into account by utilising formula 5.16, instead of formula 4.2. Each single contribution is evaluated by setting all the other corrections (and their corresponding uncertainties) to zero, and noting its influence on the final value. The ordering of the corrections listed in table 5.9 is according to its impact on the final value uncertainty.

- For the **observation angle** ε it is assumed that the ion beam in the ESR and the line of sight of the FOCAL spectrometers is 90° ($\varepsilon = 0°$), with a conservatively estimated uncertainty of 1°.

- The first of three contributions to the $\delta_{1,2}$ angles in figure 5.10 is the **detector–**

source spacing $d_{\mathrm{DS}} = 2\,600(5)\,\mathrm{mm}$. Although the alignment of the FOCAL spectrometers was performed with the greatest care, a generous uncertainty of 5 mm has been estimated. This is due to the fact that the gas-jet target has a certain width (see table 5.5), and also the finite penetration depth of x rays in the germanium detector crystal relativise the justification efforts.

- The measured **dispersions** D of the spectrometers, listed in table 5.2, deviate from the simple estimations made with the approximate formula 5.8, and are, in addition, afflicted with uncertainties. By utilising these experimentally determined results for the dispersions, the obtained Lyman-α_1 transition energy is shifted to a slightly higher value.

- The **temporal drift** effect does not change the transition energy, but increases its uncertainty. With 2.8 eV this effect is more critical to the final result than the uncertainty due to the limited statistics in the line position determination Δz_d.

- FOCAL is sensitive to a shift of the moving source, and, hence, the **gas-jet position** $\Delta x^{\mathrm{NS}}_{\text{Gas-Jet}}$ in the North–South direction. This correction is the second, and more critical contribution to the $\delta_{1,2}$ angles. Its contribution increases the measured rest frame energy of the Lyman-α_1 $E'_{\text{Ly-}\alpha_1}$ by 3.2 eV.

- Although the corrections of the ion beam velocity linked to the **electron cooler correction voltage** U_{Corr} is of minor influence, the corresponding uncertainty due to the insufficient calibration of the high voltage terminal is the second largest uncertainty contribution.

- The last and most striking contribution to the measured transition energy, as well as its uncertainty is linked to the **detector crystal position** shift Δx_{Det}. It is the third contribution to the $\delta_{1,2}$ angles and it is rather large. In total 6.5 eV from the 8.6 eV final value uncertainty is due to the three contributions for the $\delta_{1,2}$ angles determination.

Together, all these contributions add up to a final measured value for the Lyman-α_1 transition of 71 531.5(8.6) eV. The same procedure, as described for the Lyman-α_1 transition, was applied to the Lyman-α_2 and the Lyman-β transitions. One speciality appears when treating the Lyman-β transitions: Due to the fact that only the FOCAL 2 spectrometer recorded these lines the positions from FOCAL 1 are missing, and equation 5.16 cannot be applied. To circumvent this constraint, the determined $\lambda^{\text{Ly-}\beta}_{F2}$ wavelengths are multiplied by the ratio $\lambda^{\text{Ly-}\alpha_1}_{F1}/\lambda^{\text{Ly-}\alpha_1}_{F2}$, which is known from the Lyman-α_1 transition. This procedure is attributed with a 100 % uncertainty, contributing approximately 10 eV to the total uncertainty. This contribution is still small compared to the uncertainty introduced by the line position determination (see table 5.3), due

Contribution	Label	Value	Influence (eV)
Lyman Line Position	Δz_d		**71 537.8(2.2)**
FOCAL 1		$-35.2(5.1)\,\mu$m	
FOCAL 2		$-51.8(3.6)\,\mu$m	
Observation Angle	ε	$0(1)^\circ$	**$0(10^{-4})$**
Detector Source Spacing	d_{DS}	2 600(5) mm	**−(0.02)**
Dispersion Relation	D		**+0.191(46)**
FOCAL 1		$1.905\,29(53)\times10^{-10}$	
FOCAL 2		$1.909\,74(52)\times10^{-10}$	
Temporal Drift	–		**−(2.8)**
FOCAL 1		$-(3.9)\,\mu$m	
FOCAL 2		$-(7.2)\,\mu$m	
Gas Target Position	$\Delta x^{\mathrm{NS}}_{\mathrm{Gas\text{-}Jet}}$	0.25(30) mm	**+3.2(3.9)**
Electron Cooler Voltage	U_{Corr}	15(35) V	**+1.9(4.3)**
Detector Crystal Position	Δx_{Det}		**−11.6(5.1)**
FOCAL 1		1.91(42) mm	
FOCAL 2		0.13(67) mm	
Total Corrections			**−6.3(8.2)**
Lyman-α_1 Transition Energy (with Corrections)			**71 531.5(8.6)**

Table 5.9: Experimental Lyman-α_1 transition energy and the contribution due to various corrections.

to the much lower statistics compared to the Lyman-α case. Table 5.10 compiles the measured transition energies and compares them to the theoretical predictions. The theoretical value for the Lyman-α_1 transition is taken from table 2.2, while the other energies have been obtained by the cascade calculation listed in table 5.8. In the last column the experimental value for the 1 s Lamb shift is given, which is calculated via equation 4.8, and has for all transitions a theoretical value of $\Delta \mathrm{E}^{1s}_{\mathrm{LS}} = 205.2(2)$ eV.

Transition	Theoretical Energy (eV)	**This Work**	
		Energy (eV)	Lamb shift (eV)
Lyman-α_1	71 570.4(2)	71 531.5(8.6)	244.1(8.6)
Lyman-α_2	69 345.0(2.3)	69 309.8(8.3)	240.5(8.7)
Lyman-β_1	83 550.7(1.2)	83 529.2(23.3)	226.8(23.3)
Lyman-β_2	82 881.3(3)	82 863.3(26.6)	223.3(26.6)

Table 5.10: Summary of the experimentally determined Lyman transition energies and the corresponding Lamb shifts. The theoretical value for the 1 s Lamb shift is 205.2(2) eV, see table 2.1.

Figure 5.17 represents the data from table 5.10 graphically. The horizontal line at 205.2 eV gives the theoretical Lamb shift. The blue band around this value shows the uncertainty introduced by theory and, if required, the cascade calculations. The red dots with error bars show the FOCAL results for the different transitions.

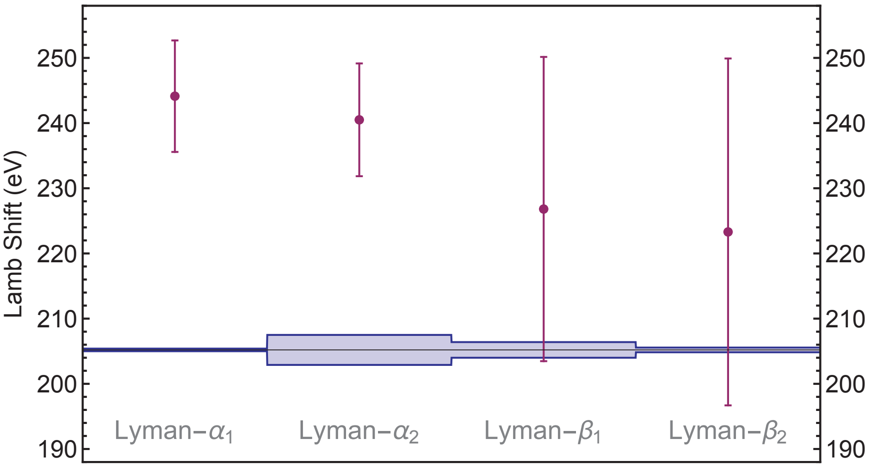

Figure 5.17: Measured Lamb shifts for the different transitions (red points). The blue band indicates the uncertainty introduced by theory and, if required, the cascade calculations.

Chapter 6

Future Improvements and Perspectives

This chapter starts with a discussion of the various uncertainty sources listed in table 5.9, and how they can be minimised in a near future run of FOCAL, if the design is only slightly adapted. The next two sections expand these ideas by looking farther into the future, where it is planned to move the whole spectrometer to a low-velocity storage ring, like the CRYRING. At the CRYRING, FOCAL could be combined with the maXs microcalorimeter to increase the robustness of the experiment. To demonstrate that the maXs prototype is on the right path to reach maturity, a first test experiment at the ESR storage ring is presented.

6.1 Future Improvements

In the last section of the previous chapter, the final result of the FOCAL experiment for the Lamb shift has been determined. Although the production run of 2012, with the fully equipped FOCAL spectrometer, demonstrated its reliability, the obtained uncertainty of 8.6 eV is too large to challenge modern theoretical predictions, including higher-order QED contributions and nuclear-structure effects. In the following sections, an outlook will be given, which measures in a future run have to be taken, in order to reduce the uncertainty significantly.

6.1.1 The Uncritical Parameters

Although the first three corrections in table 5.9 (the “green” parameters) are not critical to the final result of the FOCAL experiment, some explanatory notes will be given.

As already illustrated with formula 4.2, FOCAL is designed to be intrinsically observation angle independent, but due to small position shifts of the gas-jet target, and the detector crystal position, it depends weakly on ε after all. With the help of formula 5.16, and the accompanying text, it has been shown that its influence is negligible. This has been illustrated by assuming a large uncertainty of 1°, adding only 10^{-5} eV to the final result.

Also, for the detector–source spacing a generous uncertainty of 5 mm was assumed, which is in no means a limiting factor for the experiment. With modern theodolites and laser rangefinder it should be possible to reduce this value.

The error introduced by the dispersion relation is already on its minimum since the Lyman-α_1 transition energy was Doppler-tuned to a value, which coincides with the main Yb-γ calibration line. The given uncertainty of 46 meV has been obtained, by fitting Yb-spectra with high statistics. By comparing two different Yb-spectra recorded under the same conditions (no temporal drift), this would be their mean deviation, and can be regarded as FOCALs uncertainty in the limit of very high statistics. A measurement with a lower uncertainty is not possible, with the current instrumentation.

6.1.2 The Semi-Critical Parameters

The semi-critical contributions in table 5.9 (the “orange” parameters) affect the final uncertainty substantially, and strategies for their reduction should be a matter of concern.

Compared to the FOCAL test beam time in 2006 [Beye09], the stability of the all new constructed detector support has been increased. Also, the continuous liquid nitrogen filling of the 2D x-ray detectors, which keeps the weight of them quasi-constant, helped to reduce the temporal drift a lot. However, it would be preferable to replace critical aluminium and steel parts of the supports, with materials with a lower thermal expansion coefficient, like Invar® [Guil20]. Another possibility would be a temperature-stabilised experimental cave, which would unfortunately require a significant amount of money to be invested.

The precision of the fitted Lyman position is completely determined by the statistics collected in the three weeks of beam time. The simplest way to increase the statics would be a longer measurement period. Such an approach is unrealistic, since three weeks are basically the absolute maximum, which has a chance for approval by the General Program Advisory Committee (G-PAC) [GSI 16]. Also, the temporal drift over much longer time scales could set a natural limit to the lowest reachable uncertainty. The key to improve this value has to be a higher count rate over a shorter period of time. Another possibility to increase the count rate by a factor of two would be to use all four instead of just two of the diffracted rays. This would require another two x-ray detectors. Furthermore, the number of stored Au^{79+} ions circulating the ESR could be increased. This would require to replace the currently used MWPC particle detector by a diamond detector, which can sustain substantially higher count rates. A high current operation would also increase the intra-beam scattering, which would worsen the quality of the ion beam (see section 3.4.1). The last knob, which could be turned to increase the count rate, would be a redesign of the bent crystals. In sections 2.2.4 and 4.1.1, numerous examples were given how the efficiency of the crystals could be improved. One example can be seen in figure 2.9. Unfortunately, all measures which could be taken, would result in an increased rocking curve width, and, therefore, in a broader footprint of the x-ray lines on the 2D x-ray detectors. After this beam time, it should be possible to make a more reasonable estimation how much resolution could be trade, in favour for a higher efficiency.

6.1.3 The Critical Parameters

The last three rows in table 5.9 (the “red” parameters) dominate the final uncertainty completely. A reduction or elimination of these error sources is absolutely essential to put stringent tests onto the most advanced theories of modern atomic physics. All three parameters are of systematic nature and can therefore be eliminated with a more advanced experimental assembly.

As formula 4.2 indicates, even for a perfectly aligned spectrometer the input parameter γ, determining the speed of the ions, has to be known with a comparable precision as the measured wavelength in the spectrometers. In the current, and many other experiments, the ion velocity is determined via the applied electron cooler voltage. In section 5.2.4, it has been described which difficulties arise, when the correct cooler voltage has to be determined. One possibility to increase the accuracy of such measurements would be the usage of a high precision high voltage divider, similar to the one being used by the Physikalisch-Technische Bundesanstalt (PTB) to calibrate the high-voltage terminal of the electron cooler.

Since 2014, a high-voltage divider, with a relative precision of $\Delta U/U \approx 10^{-4}$, is available for ESR experiments [Ullm15]. In section 6.2, it will be shown that such a precision is already high enough to improve the FOCAL result.

Another possibility would be to calibrate the electron-cooler voltage with an in-ring laser spectroscopy experiment, which was performed shortly before or after the main experiment [Bote14, Loch14]. For such an experiment, one would use an atomic transition in the visible spectral rage, which is known with a very high precision. A co– or counter propagating laser beam with a tunable wavelength would then scan for this transition within the range of the expected Doppler shift. Once the resonance has been found, the ion beam velocity can be calculated via equation 4.1, very accurately. By using the same electron cooler voltage for both experiments, any systematic shift could be ruled out. The main drawback of such a measurement strategy would be, that an additional beam time had to be requested. The third method would be a measurement campaign including the maXs microcalorimeter, which will be treated in section 6.3.

The parameters concerning the Δx position in table 5.9 contribute the most to the total error budget of the FOCAL run 2012. The gas target position (3.9 eV uncertainty), and the detector crystal position (5.1 eV uncertainty), are almost completely determined by the 0.3 mm position reproducibility of the optical telescope adjustments. Therefore, it would be preferable to develop an assembly strategy, which requires neither an absolute position determination with the telescopes, nor laborious accompanying experiments. Fortunately, this is possible by introducing only a few modifications to the FOCAL experiment. The first modification concerns the Yb source holder shown in figure 6.1. Instead of having a simple butt at the tip of the source cantilever, a defined edge with an angle of 55° will be added (drawn in orange). Together with the 35° from the used view port of the target chamber, an angle of 90° relative to ion beam axis is formed. This edge can be used to scan for the gas-jet target position, in a similar manner to the one described in section 5.2.2. Such a test measurement where, after a certain travel of the Yb source holder, the complete gas jet is scattered into the target camber, has already been performed, and is shown in figure 6.2. Instead of having the peaking distribution shown in graph 5.12, one rather records the integral of this curve, which is equivalently well suited to extract the central position. Since the distance between the edge and the Yb-source window in the source holder (the blue circle in the green part in figure 6.1) is known from the manufacturing process, the Yb source can be positioned accurately where the gas jet is located, without using the telescopes.

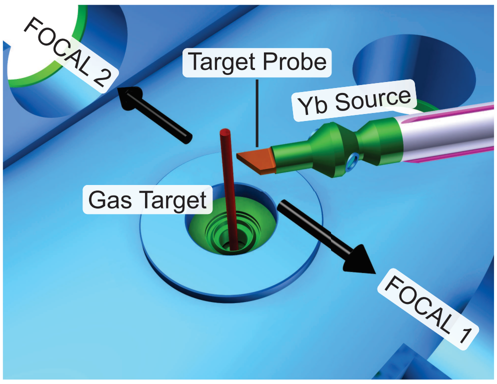

Figure 6.1: Possible extension of the Yb source positioning unit to measure the gas target position during a running beam time.

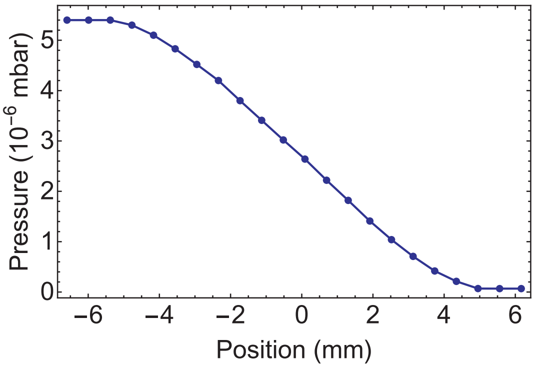

Figure 6.2: Measured pressure rise in the ESR target chamber, generated from a target probe similar to the one shown in figure 6.1.

Now, the second step of the adjustment follows. The bent crystals are rotated around the axis running through the centre of the 90° ports of the target chamber (also defined by the black arrows in figure 6.1), in clockwise and counter-clockwise direction for a few degrees. For both directions an Yb spectrum is recorded. After completing these measurements, two 2D spectra, similar to figure 5.1, have been obtained, one with rising lines from left to the right, and the other one with falling lines. For both spectra, the Yb-γ line is fitted with the $\mathrm{TMF}_{\mathrm{2D}}$ function 5.5. The intersection of the lines marks the central vertical strip position relative to the Yb-source, and hence to the gas-jet position. After completing the measurement, the bent crystals are brought back to their upright position, and the actual measurement can start. By applying this adjustment scheme, all three main unknowns – gas-jet position, detector crystal position and Yb source position – are brought in congruence, without using the telescopes or having to measure any exact position, since only relative positions matter.

6.2 Perspectives of FOCAL at the CRYRING

In the previous section, an improved measurement setup has been introduced, in order to reduce the large contributions connected with the "critical parameters". A further possibility to reduce the uncertainty is to reduce the velocity of the ions. Figure 6.3 illustrates this circumstance by reducing only and exclusively the kinetic energy of the ions, and keeping all the other uncertainties unchanged. The blue curve has been calculated for a relative voltage uncertainty of the electron cooler in the order $\Delta U/U = 5 \times 10^{-4}$, which is approximately the assumed voltage uncertainty for the 2012 run. The red curve shows the same but for a voltage uncertainty of only $\Delta U/U = 1 \times 10^{-4}$, which can be achieved with the, already available, high-voltage divider [Ullm15]. Even better voltage dividers, in the 10^{-5} region, lead to no significant improvement, compared to the 10^{-4} devices, since other uncertainty sources then start to dominate. The strong improvement in total uncertainty as the velocity is reduced can be explained by the fact, that the uncertainties in the gas-jet target positions and the detector crystal position are directly linked to the beam velocity. As shown in figure 5.10, an uncertainty in Δx leads immediately to an uncertainty in the angle δ. This angle uncertainty couples via the Doppler formula 4.1 to an uncertainty in the wavelength. By reducing the velocity (β), the influence of the angle uncertainties get reduced, and, thereby, the overall uncertainty. The reduction of the ion velocity would require to use a different calibration source, which would have to fit with the changed Doppler-shifted laboratory-frame wavelength of the moving source. A candidate for a gold beam would be a ^{177}Lu source, with γ-line at 71 641.8(6) eV [Be04], which is only 71 eV higher than the rest-frame energy of the Lyman-α_1 transition of Au^{78+}. The slower the ions are (which is desirable), the fewer one has to extrapolate. For a completely resting, or slow-moving ion, the separation in FOCALs dispersive direction would be about 120 μm, which is small enough to avoid large extrapolation uncertainties, as assured by figure 5.4. Another advantage of this source is that natural or slightly enriched ytterbium could be used, since it is produced by neutron activation of an Yb sample via

$$^{176}\mathrm{Yb} + n \xrightarrow{n\text{ caputre}} {}^{177}\mathrm{Yb} \xrightarrow{\beta^-(1.9\,\mathrm{h})} {}^{177}\mathrm{Lu} \xrightarrow{\beta^-(6.6\,\mathrm{d})} {}^{177}\mathrm{Hf} + \gamma\,(71.6\,\mathrm{keV}) \qquad (6.1)$$

A disadvantage of ^{177}Lu as the main calibration source is its uncertainty in energy of 600 meV, which is more than one order of magnitude worse than the ^{169}Yb γ-line, with only 40 meV uncertainty. It is a general problem to find precise γ-ray standards in this energy region, and the ^{169}Yb γ-line being the only transition which features such a good precision. If possible, calibration transitions would be determined with the same precision as the ^{169}Yb γ-line, or even better, this flaw could be eliminated, even if the calibration would be re-measured after a future FOCAL run. However, it is reasonable to assume that this drawback is more than made up for by the gain in precision according to graph 6.3. If a kinetic ion beam energy of *e.g.* 8 MeV/u is envisaged this would lead to a total precision increase by a factor of three. Since the storage time of an ion beam depends strongly on the electron capture cross section from the rest gas atoms, which increases very strongly with slower velocities, a storage ring with very good vacuum conditions should be used.

The CRYRING, which is currently under installation at FAIR, is such a storage ring that has specifically been designed for a low-velocity ion beam operation. It has been demonstrated that a vacuum of better than 10^{-11} mbar can be achieved [FAIR11], which is a crucial requirement for storing highly charged heavy ions. The expected beam lifetimes in the CRYRING for Au^{79+} lies between 3 s (300 keV/u), and 20 min (14 MeV/u), with 7 min at the chosen energy of 8 MeV/u [Lest15]. Such a storage time would be sufficiently long to conduct the experiment.

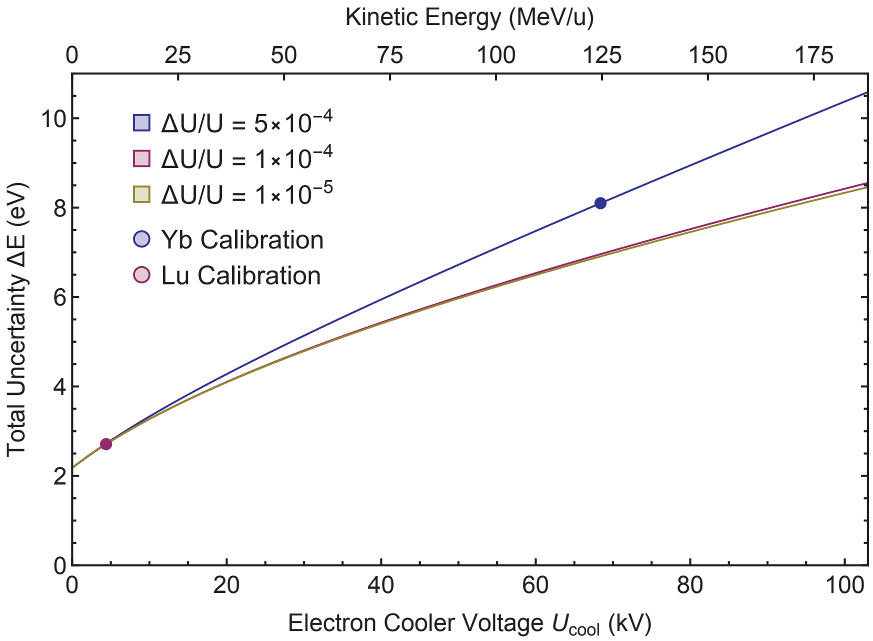

Figure 6.3: Obtained total uncertainty for a future FOCAL run, if all parameters would have the same value as listed in table 5.9, but only the kinetic energy of the beam would be reduced. The three different curves show the influence of the relative precision of the electron cooler voltage calibration, which is only in the high energy regime of major interest.

6.3 Perspectives of a maXs–FOCAL Combination

Even if in the future the electron cooler voltage can be determined much more accurate with the help of voltage dividers, a determination on the basis of a third independent E_{Lab} measurement would be preferable. This would make the Doppler correction completely independent from any external input parameters, except from the calibration lines of the source, which are likely to improve in precision, as time goes by. This third detector should feature a comparable resolving power as the FOCAL spectrometers, and has to be located at a well defined observation angle with respect to the ion beam. A detector that meets these requirements is the maXs microcalorimeter, which has been introduced in section 2.3. While the high resolution has already been discussed, the calorimeters suffer the same problem as other detector types when it comes to precise angle determination. However, the sensitivity on the angle-dependence is not the same for all observation angles. If the Doppler formula 4.1 is derived with respect to the angle, one yields

$$\frac{\partial}{\partial\theta}\lambda_{\text{Lab}} = \lambda_0\,\beta\,\gamma\,\sin(\theta) \tag{6.2}$$

which is 0 for $\theta = 0°$ and 180°. At these two special angles, small misalignments in θ do *not* influence the final result, which is why these angles are good positions for x-ray detectors. Since these directions are blocked by the beam pipes, angles very close to 0° and 180° have to be used [Beye95b, Gumb05]. In a small storage ring, like the CRYRING, the ion beam moves only on very short section on a straight path, and is then deflected by the dipole bending magnets. Therefore, the microcalorimeter can be positioned in a common line of sight with the ion beam, at the future CRYRING storage ring. As depicted in figure 6.4 the microcalorimeter could be positioned at the 0° (or 180°) port at the CRYRING electron cooler.

To test if the sensitive microcalorimeter, which measure smallest magnetisation changes, works also properly in a storage ring environment, where high magnetic fields of up to 1.6 T are ramped in a few seconds, two dedicated detector test beam times have been performed, in April and August 2014, at the ESR. While the results for the April beam time have been treated in great detail in [Kell14], the findings for the August beam time are discussed in the following.

In the August beam time, the projectile ion Xe^{54+} was stored at a kinetic energy of 50.0(5) MeV/u, and collided with a xenon gas-jet target [Heng15]. The observation angle was $\theta = 60(1)°$, leading to Doppler-shifted characteristic transitions to higher energies. Figure 6.5 shows the most interesting region of the recorded x-ray spectrum. At a laboratory frame energy around 30 keV, a broad continuum of x-ray photons can be seen. This radiation stems from the xenon target gas, which is ionised to different charge states, ranging from 1+ up to 53+, when being hit by the projectile ion. Depending on the actual charge state of the emitting ion, the characteristic K_α-radiation exhibits slightly different transition energies, result-

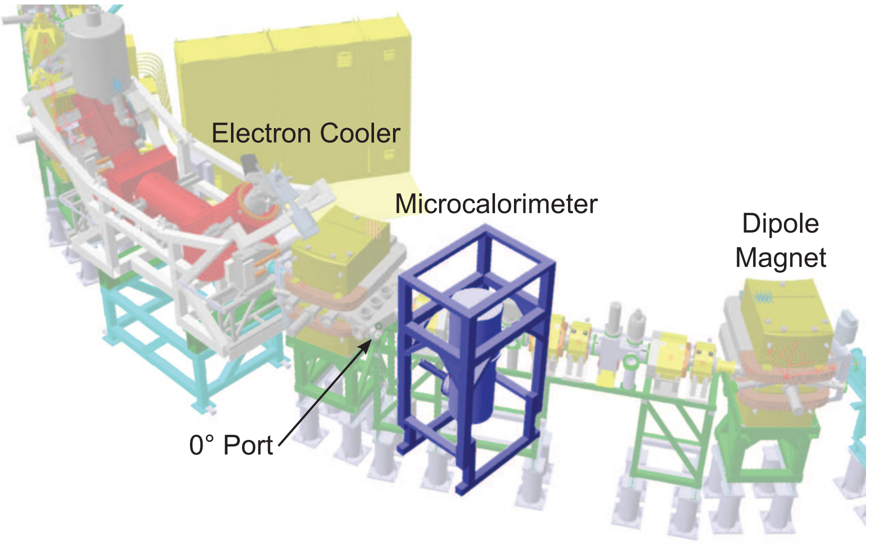

Figure 6.4: CAD drawing of the maXs microcalorimeter at the 0° port of the CRYRING electron cooler. By having the calorimeter at this observation angle insensitive port, the FOCAL experiment would not have to rely on the external input parameter for the ion beam velocity.

ing in a broad distribution. The one-electron capture by a completely ionised ion, and the subsequent decay cascade to the ground state via emission of characteristic (Lyman) radiation, has already been detailed in sections 4.2 and 5.2.5. The very same also happens to the Xe^{54+} ions, when colliding with the xenon gas-jet. At 35 keV, the Lyman-α transition from a single electron capture of a projectile ion, making it a hydrogen-like system, can be seen. At higher energies, shown in the inset between 41 keV and 47 keV, transitions up to Lyman-ζ ($n = 6 \to 1$) can be identified. This would not be possible with a standard semiconductor detector, due to its much lower energy resolution. To illustrate this fact, the whole spectrum has been convoluted with a Gaussian profile (labelled with “Ge-Detector”, FWHM = 300 eV), which smoothens out subtle details, like the Lyman-β fine structure splitting, which is only visible in the microcalorimeter spectrum. Slightly below the Lyman-α_2 transition, two peaks labelled with “$n = 2 \to 1\,(\mathrm{He})$” can be seen. At a higher zoom level it turns out that each of these peaks again consists of two very close transitions, stemming from projectile ions which have captured two electrons, making it a *helium*-like system. The lower two transitions are the $1\mathrm{s}\,2\mathrm{s} \to 1\,\mathrm{s}^2$ ($^3\mathrm{S}_1 \to {}^1\mathrm{S}_0$) and the $1\mathrm{s}\,2\mathrm{p} \to 1\,\mathrm{s}^2$ ($^3\mathrm{P}_1 \to {}^1\mathrm{S}_0$), whereas the two upper transitions are the $1\mathrm{s}\,2\mathrm{p} \to 1\,\mathrm{s}^2$ ($^3\mathrm{P}_2 \to {}^1\mathrm{S}_0$) and the $1\mathrm{s}\,2\mathrm{p} \to 1\,\mathrm{s}^2$ ($^1\mathrm{P}_1 \to {}^1\mathrm{S}_0$).

To compare the measured laboratory-frame energies with theoretical results for the rest-frame energy, the Doppler correction for the relativistically moving ions has to be performed. The Doppler factor

$$f_D^1 = \frac{1}{\gamma\,(1 - \beta\,\cos(\theta))} \tag{6.3}$$

gives the ratio between the Doppler-shifted laboratory frame and the rest-frame en-

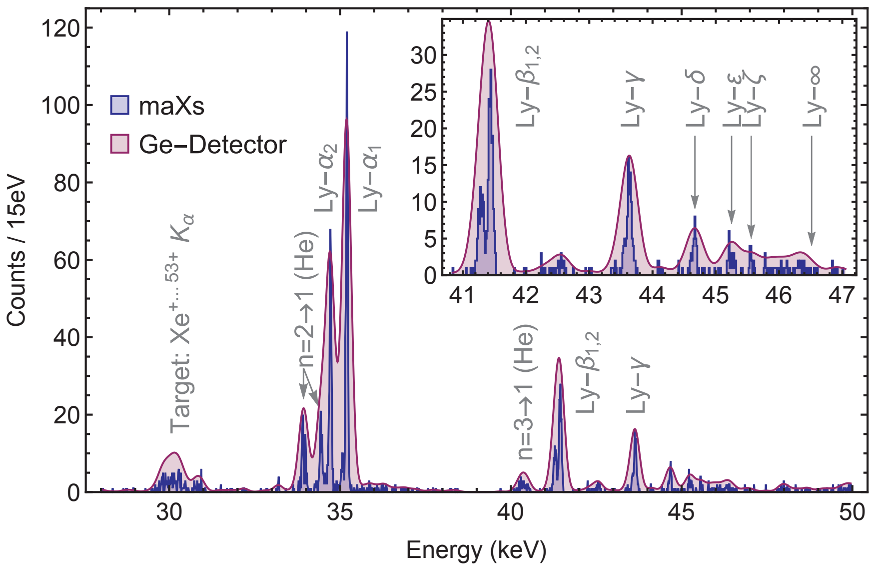

Figure 6.5: X-ray spectrum recorded with the maXs microcalorimeter (blue) at the 60° port of the ESR target chamber. The target gas was xenon being hit by a 50 MeV/u Xe^{54+} ion beam. Compared to the spectrum 4.15, recorded with a conventional germanium detector in the same energy region, the much higher resolution becomes obvious. For comparison, the whole spectrum has been convoluted with a Gaussian curve with 300 eV FWHM, to illustrate the corresponding result obtained with a good germanium detector (red).

ergy. Calculating the Doppler factor with values for the kinetic energy and observation angle given above yields $f_D^1 = 1.126\,6(64)$, which is afflicted with an unusable large uncertainty, due to the insufficient precision of the observation angle determination.

To circumvent this problem, a second Doppler factor f_D^2 had been determined experimentally, by dividing the measured Lyman-α_1 transition energy by the theoretical rest frame energy for this transition. By doing so, it is not longer possible to compare the measured H-like transitions with the theoretical results, since this information has been used to adjust both spectra on each other. However, two other circumstances can still be studied: *(i)* The measured transition energies of the He-like transitions can still be compared with theory, since this is a completely different system. *(ii)* This beam time was intended as a detector test experiment, where the performance of a magnetic calorimeter, in the harsh environment of a magnetic storage ring, should be studied. The linearity and obtained quality of the results still hold very important information for future runs of the microcalorimeter.

With the theoretical Lyman-α_1 transition energy of 31 283.9 eV [Yero15] and the measured value of 35 200.0(1.3) eV, a new Doppler factor $f_D^2 = 1.125\,179(42)$ can be calculated, which is more than two orders of magnitude more precise than f_D^1.

With this Doppler factor, the theoretical transition energies for all major lines in the spectrum 6.5 can be transformed in laboratory frame energies, which is done in table 6.1. Also the experimental results of these transitions are listed in this table, and can be compared with the predictions.

Most of the measured energies agree within 1 σ with the theoretical predictions, the

Charge State	Transition to Ground State	Theoretical Energy (eV)		Measurement (eV)
		Rest Frame	Laboratory Frame$^{(i)}$	
He-like	$1s2s\ ^3S_1$	30 129.1	33 900.7(1.3)	33 901.1(3.3)
He-like	$1s2p\ ^3P_1$	30 206.2	33 987.3(1.3)	33 983.6(2.9)
He-like	$1s2p\ ^3P_2$	30 594.3	34 424.0(1.3)	34 433.9(6.1)
He-like	$1s2p\ ^1P_1$	30 630.0	34 464.3(1.3)	34 480.3(23.5)
H-like	Ly-α_2, $2\,p_{1/2}$	30 856.5	34 719.1(1.3)	34 722.5(4.2)$^{(ii)}$
H-like	Ly-α_2, $2\,s_{1/2}$	30 863.6	34 727.1(1.3)	
H-like	Ly-α_1, $2\,p_{3/2}$	31 283.9	35 200.0(1.3)	35 200.0(1.3)$^{(iii)}$
H-like	Ly-β_2, $3\,p_{1/2}$	36 706.6	41 301.5(1.5)	41 298.3(6.8)
H-like	Ly-β_1, $3\,p_{3/2}$	36 833.4	41 444.2(1.5)	41 449.2(3.4)
H-like	Ly-γ_2, $4\,p_{1/2}$	38 736.2	43 585.2(1.6)	43 559.2(10.9)
H-like	Ly-γ_1, $4\,p_{3/2}$	38 789.5	43 645.2(1.6)	43 644.5(5.5)

Table 6.1: Measured transition energies for the most prominent lines in the spectrum 6.5. The theoretical rest frame transition energies have been taken from [John95] for the He-like system, from [Yero15] for the H-like system ($n \leq 2$) and with the help of the solution of the Dirac equation 2.6 ($n \geq 3$). **Annotations:** *(i)* The column 'Laboratory Frame' has been calculated with the Doppler factor f_D^2, given uncertainties are only due to this factor. *(ii)* This line is a blend of the $2\,p_{1/2}$, $2\,s_{1/2} \rightarrow 1\,s_{1/2}$ transitions, which cannot be resolved separately. *(iii)* This transition has been used to determine the Doppler factor f_D^2 mentioned in *(i)*.

values which deviate more than $1\,\sigma$ are all well below $2.5\,\sigma$, which is compatible with statistical fluctuations. The overall linearity in this energy region is very encouraging, marking the transition from a prototype system to a reliable and mature measurement tool.

The 'moderate' precision of only down to 1.3 eV requires some explanatory notes. The reason for that can be found in the low counting statistics in the spectrum. This low statistics is due to three reasons: *(i)* The accumulation time was only one day, which is very short compared to the three weeks of the 2012 FOCAL run. *(ii)* The data shown in the figure is from one 1 mm^2 small pixel, being located at *(iii)* 1.6 m from the target due to mechanical constraints. For the near future it is planned to test the microcalorimeter at the CRYRING, where longer measurement periods and smaller distances to the target will be possible. Also, a microcalorimeter system with more pixels will then be available, which increases the solid angle coverage additionally. It is also informative to note, that a modern semiconductor detector, measuring with the same statistics, would reach a more than ten times worse precision.

Chapter 7

Discussion

In the present work, the high resolving power of two complementary x-ray detector types, capable of surpassing that of standard semiconductor detectors, has been studied. With these detectors it should be possible to enhance the current experimental precision in the field of high-precision x-ray spectroscopy by at least one order of magnitude, being competitive with the latest theoretical predictions, and trigger further research in this area.

The first detector type covered was the crystal spectrometer FOCAL utilising the *wave-like* character of the x-ray photons to conclude on its *wavelength*. After a successful beam time of three weeks at the ESR storage ring, about 1 500 Lyman-α_1 photons per spectrometer, stemming from hydrogen-like gold ions (Au^{78+}), could be collected. The positions of the characteristic lines relative to the main Yb-γ calibration line could be determined with great precision, being basically limited by the counting statistics only. Figure 7.1 shows once again the different contribution to the total Lamb shift, as already presented with figure 2.1, but extended by the reached experimental precision (black dots) reported for various measurements on hydrogen-like heavy ions [Beye97b, Yero15]. The red dot represents the *statistical* uncertainty reached by this experiment. This dot represents a breakthrough, since it demonstrates that a crystal spectrometer for hard x-ray radiation can be operated at a comparably low-luminous x-ray source, like a storage ring, and being competitive with the most precise experiments ever conducted.

Due to its complicated geometrical assembly, a number of accompanying experiments and simulations had to be performed to correct for systematic deviations linked to these effects. The temporal drift of the calibration line position and hence the Lyman line positions could be corrected by calibrating the spectrometer in regular intervals. Although the uncertainty introduced by this effect is of minor importance compared to other uncertainty sources, in a future run enhancements concerning the long term mechanical stability should be addressed, as already pointed out in section 6.1.2.

More crucial to the total uncertainty of the experiment was the ion beam velocity

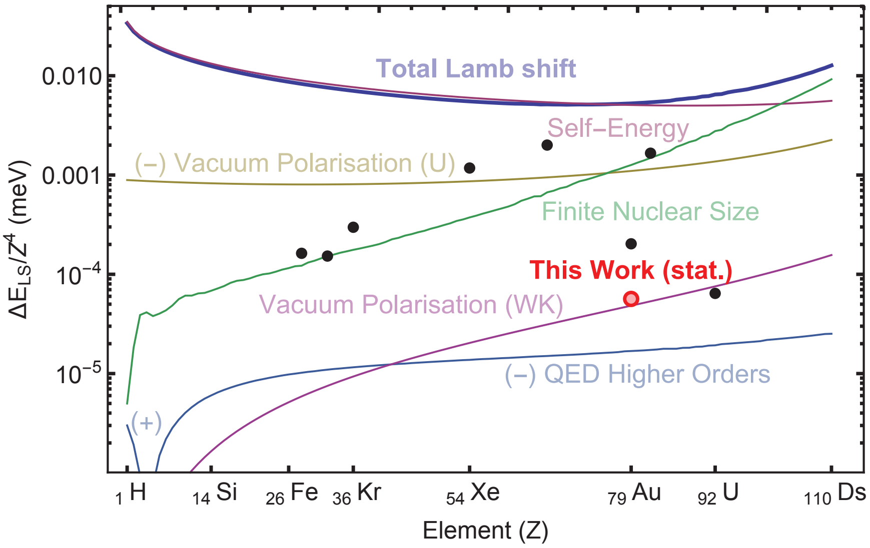

Figure 7.1: Same figure as 2.1, but extended by the reached experimental precision (black dots) reported for various measurements on hydrogen-like heavy ions [Beye97b, Yero15]. The red dot represents the *statistical* uncertainty reached by the FOCAL experiment, being competitive with the most precise experiments ever conducted.

determined by the electron cooler voltage. This external input parameter is the limiting factor for many experiments conducted at the ESR [Gumb05, Loch14], but in the near future this issue should be resolved by an external, absolute voltage determination, by a high voltage divider with a relative uncertainty of at least $\Delta U/U \leq 10^{-4}$ [Ullm15], which will be sufficient for the FOCAL experiment, as depicted in figure 6.3.

The last and main contribution to the total uncertainty is the lack of knowledge of the actual moving source position (gas-jet target position) relative to the detector position. In the aftermath of a beam time, it is difficult to reconstruct the precise position, but in a future run this should be avoidable from the beginning, with the help of a special build-up strategy given in the last paragraph of section 6.1.3. In this way, all the critical (“red”) corrections in table 5.9 should be eliminated, or being at least reduced by a huge factor.

After having included all corrections obtained by these investigations, the Lyman transition energies, and hence the corresponding 1s Lamb shift, in hydrogen-like gold Au^{78+} could be determined as listed in table 5.10. All four experimental results for the 1s Lamb shift are in good agreement with each other. While the precision for the Lyman-α results are limited to about 9 eV, mainly caused by systematic effects, the uncertainty of the Lyman-β transitions are afflicted with uncertainties of about 23 eV, due to the much lower statistics in these lines (*cf.* graph 5.7 (d)). These results can be compared with the findings of two earlier experiments also conducted at the ESR storage ring.

- The first experiment on the 1 s Lamb shift in hydrogen-like gold was performed by H.F. Beyer *et al.* in 1994 [Beye94, Beye95a]. The experiment was performed by utilising the electron cooler of the ESR as a free-electron target. A germanium detector was mounted in the forward direction, with an observation angle close zero degrees. A particle detector in the following dipole magnet was used to apply the coincidence technique. In this way a 1 s Lamb shift of 202.3(7.9) eV could be obtained.

- The second experiment aiming for the determination of the 1 s Lamb shift was performed by S. Kraft-Bermuth *et al.* in 2012 [Kraf13]. It was conducted at the gas-jet target section of the ESR, parallel to the FOCAL experiment. The used detector was a thermistor based microcalorimeter with an energy resolution of 200 eV (FWHM) under experiment conditions. The observation angle relative to the ion beam was about 145°, whereas the accurate determination was a major contribution to the systematic uncertainty. The obtained value for the Lamb shift was 206(11) eV.

Both experiments, and the theoretical prediction, tend to a lower value for the Lamb shift compared to the FOCAL results. While the Lyman-α values deviate notably from these findings ($3.6\,\sigma$ for Beyer *et al.*, $2.7\,\sigma$ for Kraft-Bermuth *et al.*), the Lyman-β results are in a fairly good agreement ($1.0\,\sigma$ for Beyer *et al.*, $0.8\,\sigma$ for Kraft-Bermuth *et al.*), which is mainly due to the much higher uncertainty for the Lyman-β results. This indicates that systematic effects have to be addressed more seriously before the next measurement campaign with the FOCAL spectrometer is performed. Some first considerations can be found in section 6.1.3.

The second detector system covered was the metallic magnetic microcalorimeter maXs utilising the *particle-like* character of the photons to conclude on its *energy*, instead of its wavelength. The development of a working sensor, operating in the hard x-ray region ($E_\gamma \approx 60\,\mathrm{keV}$), is still in progress, and only first preliminary results obtained by prototypes are available. Nevertheless, this first findings are very promising since it could be successfully demonstrated that the high energy resolution of the sensor does not suffer in the harsh magnetic storage-ring environment, compared to well-controlled conditions present in laboratory tests. In [Kell14] is has been reported that the archived energy resolution inside the ESR cave was even better than in the laboratory, due to a somewhat lower operating temperature. In table 6.1 the measured transition energies stemming from the $\mathrm{Xe}^{54+} \xrightarrow{50\,\mathrm{MeV/u}} \mathrm{Xe}$ beam time are listed. The results for the helium-like xenon are in good agreement with theoretical predictions, if the Lyman-α_1 transition of the hydrogen-like ion is used for the Doppler correction. Another very motivating feature of the spectrum 6.5 is the high content of over 100 counts per pixel and day of beam time. If one considers the large sensor to gas-jet target distance of 1.6 m this is even more impressive. In a detector test at the CRYRING, this distance would shrink to a few dozens of centimetres, boosting the solid-angle coverage of the system by high factors. The complete system is planned to have 64 working pixels, which would enhance the overall system efficiency by more than two orders of magnitude.

As already mentioned in section 6.3, a combination of both detector types and a relocation of the experiment activities to the low energy storage ring CRYRING would make the whole process independent of any external input parameters, like the electron cooler voltage, resulting in a clean and completely by the experimenters defined research environment.

With this new generation of high-resolution detector system, in combination with a low energy storage ring, the field of high precision x-ray spectroscopy is looking in a very bright future, getting rid of the low resolving power constraints from the semiconductor detectors, governing this domain for many years.

Zusammenfassung

In der vorliegenden Arbeit wurde untersucht, mit welchen Mitteln sich die Genauigkeit von röntgenspektroskopischen Untersuchungen von hochgeladenen Schwerionen steigern lässt. Solche Messungen sind notwendig, um theoretische Vorhersagen der Quantenelektrodynamik (QED) über die Lage der Energieniveaus im Bereich extrem hoher Feldstärken zu überprüfen. Bisherige Experimente stützten sich hauptsächlich auf die Verwendung von Halbleiterdetektoren, deren maximal erzielbares Auflösungsvermögen bereits das technologische Limit erreicht hat. Weitere Auflösungssteigerungen bedingen daher den Einsatz neuer Technologien, von denen im Rahmen dieser Arbeit zwei komplementäre Ansätze untersucht wurden.

Die erste behandelte Möglichkeit zur Auflösungssteigerung besteht in der Verwendung eines hochauflösenden, aber gleichzeitig effizienten Doppel Kristallspektrometers am internen Gas-Jet Target des Experimentierspeicherring ESR des GSI Helmholtzzentrums in Darmstadt. Das in fokussierender asymmetrisch- kompensierte Laue-Geometrie aufgebaute FOCAL Spektrometer erreicht hierbei eine um den Faktor zehn höhere Auflösung, als die besten kommerziell erhältlichen Halbleiterdetektoren und ist durch den Aufbau als Zwillingsspektrometer inhärent beobachtungswinkelunabhängig. Dies ist bei relativistisch-schnell bewegten Quellen, wie etwa den gespeicherten Schwerionen im ESR, aufgrund des Doppler Effektes von maßgeblicher Wichtigkeit. Das in den vergangenen Jahren von Dr. Heinrich F. Beyer entwickelte FOCAL Experiment konnte 2012 erstmals vollausgestattet, während einer dreiwöchigen Strahlzeit, getestet werden. Dabei wurde ein Wert von 244.1(8.6) eV für die $1\,s$ Lamb Verschiebung in wasserstoffähnlichem Gold (Au^{78+}) ermittelt.

Die zweite behandelte Methode, um die Genauigkeit zukünftiger röntgenspektroskopischer Untersuchungen zu erhöhen, liegt in der Verwendung des metallisch-magentischen Mikrokalorimeters maXs, welches gegenwärtig von der Gruppe um Prof. Dr. Christian Enss am Kirchhoff Institut für Physik in Heidelberg entwickelt wird. Da sich diese Sensoren noch in der Entwicklung befinden, konnte noch kein Wert für die Lamb-Verschiebung ermittelt, dafür aber erste, sehr vielversprechende Röntgenspektren von wasserstoffähnlichem Xenon aufgezeichnet werden. Mit diesem Test wurde gezeigt, dass die hervorragende Auflösung von Labortests auch unter Strahlbedingungen erreicht werden kann.

Beide Systeme ergänzen sich optimal, insbesondere im Hinblick auf die zukünftigen Experimentiermöglichkeiten, die das FAIR Projektes bieten wird. Speziell am neuen Niederenergiespeicherring CRYRING ist damit zu rechnen, dass sich die erreichbare Genauigkeit drastisch erhöhen wird.

Bibliography

[Acke07] W. a. Ackermann, G. Asova, V. Ayvazyan, A. Azima, N. Baboi, J. Bähr, V. Balandin, B. Beutner, A. Brandt, A. Bolzmann, *et al.* "Operation of a free-electron laser from the extreme ultraviolet to the water window". *Nature photonics*, Vol. 1, No. 6, pp. 336–342, 2007.

[Alta06] M. Altarelli, R. Brinkmann, M. Chergui, W. Decking, B. Dobson, S. Düsterer, G. Grübel, W. Graeff, H. Graafsma, J. Hajdu, *et al.* *The Technical Design Report of the European XFEL.* Vol. 4, DESY XFEL Project Group, 2006.

[Ange13] I. Angeli and K. Marinova. "Table of experimental nuclear ground state charge radii: An update". *Atomic Data and Nuclear Data Tables*, Vol. 99, No. 1, pp. 69 – 95, 2013.

[Attw99] D. Attwood. *Soft X-Rays and Extreme Ultraviolet Radiation.* Cambridge University Press, 1999.

[Auma10] Aumann, T., Langanke, K., Peters, K., and Stöhlker, Th. "FAIR - from a few-body perspective". *EPJ Web of Conferences*, Vol. 3, p. 01006, 2010.

[Auth01] A. Authier. *Dynamical Theory of X-Ray Diffraction.* Oxford University Press Inc., 2001.

[Bash76] S. Bashkin, Ed. *Beam-Foil Spectroscopy.* Springer-Verlag, 1976.

[Batt64] B. W. Batterman and H. Cole. "Dynamical Diffraction of X Rays by Perfect Crystals". *Rev. Mod. Phys.*, Vol. 36, pp. 681–717, Jul 1964.

[Be04] M.-M. Bé, V. Chisté, C. Dulieu, E. Browne, V. Chechev, N. Kuzmenko, R. Helmer, A. Nichols, E. Schönfeld, and R. Dersch. *Table of Radionuclides.* Vol. 2 of *Monographie BIPM-5*, Bureau International des Poids et Mesures, Pavillon de Breteuil, F-92310 Sèvres, France, 2004.

[Beie93] P. Beiersdorfer, D. Knapp, R. E. Marrs, S. R. Elliott, and M. H. Chen. "Structure and Lamb shift of $2s_{1/2}$-$2p_{3/2}$ levels in lithiumlike U^{89+} through neonlike U^{82+}". *Phys. Rev. Lett.*, Vol. 71, pp. 3939–3942, Dec 1993.

[Berg98] M. J. Berger *et al.* “XCOM: Photon Cross Sections Database”. `http://www.nist.gov/pml/data/xcom/index.cfm`, 1998.

[Bern12] S. Bernitt, G. Brown, J. K. Rudolph, R. Steinbrügge, A. Graf, M. Leutenegger, S. Epp, S. Eberle, K. Kubiček, V. Mäckel, *et al.* “An unexpectedly low oscillator strength as the origin of the Fe xvii emission problem”. *Nature*, Vol. 492, No. 7428, pp. 225–228, 2012.

[Beth47] H. A. Bethe. “The Electromagnetic Shift of Energy Levels”. *Phys. Rev.*, Vol. 72, pp. 339–341, Aug 1947.

[Beth77] H. A. Bethe and E. E. Salpeter. *Quantum Mechanics of One- and Two-Electron Atoms.* A Plenum/Rosetta Edition, 1977.

[Beye04] H. Beyer, T. Stöhlker, D. Banas, D. Liesen, D. Protic, K. Beckert, P. Beller, J. Bojowald, F. Bosch, E. Förster, B. Franzke, A. Gumberidze, S. Hagmann, J. Hoszowska, P. Indelicato, O. Klepper, H.-J. Kluge, S. König, C. Kozhuharov, X. Ma, B. Manil, I. Mohos, A. Oršic-Muthig, F. Nolden, U. Popp, A. Simionovici, D. Sierpowski, U. Spillmann, Z. Stachura, M. Steck, S. Tachenov, M. Trassinelli, A. Warczak, O. Wehrhan, and E. Ziegler. “FOCAL: X-ray optics for accurate spectroscopy”. *Spectrochimica Acta Part B: Atomic Spectroscopy*, Vol. 59, No. 10-11, pp. 1535 – 1542, 2004. 17th International Congress on X-Ray Optics and Microanalysis.

[Beye09] H. Beyer, D. Attia, D. Banas, E.-O. L. Bigot, F. Bosch, J.-C. Dousse, E. Förster, A. Gumberidze, S. Hagmann, S. Heß, J. Hoszowska, P. Indelicato, P. Jagodzinski, C. Kozhuharov, T. Krings, D. Liesen, X. Ma, B. Manil, I. Mohos, M. Pajek, D. Protic, R. Reuschl, J. Rzadkiewicz, A. Simionovici, U. Spillmann, Z. Stachura, T. Stöhlker, M. Trassinelli, S. Trotsenko, A. Warczak, O. Wehrhan, and E. Ziegler. “Crystal optics for hard-X-ray spectroscopy of highly charged ions”. *Spectrochimica Acta Part B: Atomic Spectroscopy*, Vol. 64, No. 8, pp. 736 – 743, 2009. A Collection of Papers Presented at the 19th International Congress on X-Ray Optics and Microanalysis (ICXOM-19).

[Beye13] H. Beyer, T. Gaßner, *et al.* “FOCAL - x-ray spectroscopy for QED in strong fields”. *GSI annual report 2012*, 2013.

[Beye15] H. F. Beyer, T. Gassner, M. Trassinelli, R. Heß, U. Spillmann, D. Banaś, K.-H. Blumenhagen, F. Bosch, C. Brandau, W. Chen, C. Dimopoulou, E. Förster, R. E. Grisenti, A. Gumberidze, S. Hagmann, P.-M. Hillenbrand, P. Indelicato, P. Jagodzinski, T. Kämpfer, C. Kozhuharov, M. Lestinsky, D. Liesen, Y. A. Litvinov, R. Loetzsch, B. Manil, R. Märtin, F. Nolden, N. Petridis, M. S. Sanjari, K. S. Schulze, M. Schwemlein, A. Simionovici,

M. Steck, T. Stöhlker, C. I. Szabo, S. Trotsenko, I. Uschmann, G. Weber, O. Wehrhan, N. Winckler, D. F. A. Winters, N. Winters, and E. Ziegler. “Crystal optics for precision x-ray spectroscopy on highly charged ions - conception and proof”. *Journal of Physics B: Atomic, Molecular and Optical Physics*, Vol. 48, No. 14, p. 144010, 2015.

[Beye16] H. Beyer. “private communication”. 2016.

[Beye94] H. Beyer, D. Liesen, F. Bosch, K. Finlayson, M. Jung, O. Klepper, R. Moshammer, K. Beckert, H. Eickhoff, B. Franzke, F. Nolden, P. Spädtke, M. Steck, G. Menzel, and R. Desllates. “X rays from radiative electron capture of free cooling electrons for precise Lamb-shift measurements at high Z: Au78+”. *Physics Letters A*, Vol. 184, No. 6, pp. 435 – 439, 1994.

[Beye95a] H. Beyer. “The 1s Lamb shift of hydrogen-like very heavy ions measured at an electron cooler”. *Instrumentation and Measurement, IEEE Transactions on*, Vol. 44, No. 2, pp. 510–513, Apr 1995.

[Beye95b] H. Beyer, G. Menzel, D. Liesen, A. Gallus, F. Bosch, R. Deslattes, P. Indelicato, T. Stöhlker, O. Klepper, R. Moshammer, F. Nolden, H. Eickhoff, B. Franzke, and M. Steck. “Measurement of the ground-state lambshift of hydrogenlike uranium at the electron cooler of the ESR”. *Zeitschrift für Physik D Atoms, Molecules and Clusters*, Vol. 35, No. 3, pp. 169–175, 1995.

[Beye97a] H. F. Beyer. “Characterization of transmission-type curved-crystal X-ray optics for fast ion-beam spectroscopy”. *Nuclear Instruments and Methods in Physics Research Section A: Accelerators, Spectrometers, Detectors and Associated Equipment*, Vol. 400, No. 1, pp. 137 – 148, 1997.

[Beye97b] H. F. Beyer, H.-J. Kluge, and V. P. Shevelko, Eds. *X-Ray Radiation of Highly Charged Ions*, Chap. Atomic Structure and Spectra, p. 82. Springer, 1997. Table 3.16.

[Beye99] H. F. Beyer and V. P. Shevelko, Eds. *Atomic Physics with Heavy Ions*. Springer, 1999.

[Bhne90] P. Marin and P. Mandrillon, Eds. *The Performance of SIS and Developments at GSI*, Editions Frontieres, June 1990.

[Blas89] K. Blasche and D. Bohne. “Status report on the GSI Synchrotron facility and first beam results”. In: *Particle Accelerator Conference, 1989. Accelerator Science and Technology., Proceedings of the 1989 IEEE*, pp. 27–28 vol.1, Mar 1989.

[Blok65] M. Blokhin. *Method of X-Ray Spectroscopic Research.* Pergamon Press, 1965.

[Blue16] BlueFors Cryogenics. “Dilution Refrigerator”. `http://www.bluefors.com`, 2016.

[Borr59] G. Borrmann and G. Hildebrandt. “Absorption und Weg interferierender Röntgenstrahlen im schwach deformierten Kristallgitter”. *Zeitschrift für Physik*, Vol. 156, No. 3, pp. 189–199, 1959.

[Bote14] B. Botermann, D. Bing, C. Geppert, G. Gwinner, T. W. Hänsch, G. Huber, S. Karpuk, A. Krieger, T. Kühl, W. Nörtershäuser, C. Novotny, S. Reinhardt, R. Sánchez, D. Schwalm, T. Stöhlker, A. Wolf, and G. Saathoff. “Test of Time Dilation Using Stored Li^+ Ions as Clocks at Relativistic Speed”. *Phys. Rev. Lett.*, Vol. 113, p. 120405, Sep 2014.

[Brag13] W. H. Bragg and W. L. Bragg. “The Reflection of X-rays by Crystals”. *Proceedings of the Royal Society of London A: Mathematical, Physical and Engineering Sciences*, Vol. 88, No. 605, pp. 428–438, 1913.

[Bran00] C. Brandau. *Messungen zur Photorekombination hochgeladener lithiumähnlicher Ionen.* PhD thesis, Justus-Liebig-Universität Gießen, 2000.

[Bran03] C. Brandau, C. Kozhuharov, A. Müller, W. Shi, S. Schippers, T. Bartsch, S. Böhm, C. Böhme, A. Hoffknecht, H. Knopp, N. Grün, W. Scheid, T. Steih, F. Bosch, B. Franzke, P. Mokler, F. Nolden, M. Steck, T. Stöhlker, and Z. Stachura. “Precise Determination of the $2s_{1/2}$-$2p_{1/2}$ Splitting in Very Heavy Lithiumlike Ions Utilizing Dielectronic Recombination”. *Phys. Rev. Lett.*, Vol. 91, p. 073202, Aug 2003.

[Bria90] J. P. Briand, P. Chevallier, P. Indelicato, K. P. Ziock, and D. D. Dietrich. “Observation and measurement of $n=2\rightarrow n=1$ transitions of hydrogenlike and heliumlike uranium”. *Phys. Rev. Lett.*, Vol. 65, pp. 2761–2764, Nov 1990.

[Cauc32] Y. Cauchois. “Spectrographie des rayons X par transmission d’un faisceau non canalisé à travers un cristal courbé - I.”. *J. Phys. Radium*, Vol. 3, pp. 320 – 336, Jul 1932.

[Cauc33] Y. Cauchois. “Spectrographie des rayons X par transmission d’un faisceau non canalisé à travers un cristal courbé - II.”. *J. Phys. Radium*, Vol. 4, No. 2, pp. 61–72, 1933.

[Chat06] S. Chatterjee, H. Beyer, D. Liesen, T. Stöhlker, A. Gumberidze, C. Kozhuharov, D. Banas, D. Protic, K. Beckert, P. Beller, T. Krings,

F. Bosch, B. Franzke, S. Hagmann, J. Hoszowska, P. Indelicato, H.-J. Kluge, X. Ma, B. Manil, I. Mohos, F. Nolden, U. Popp, A. Simionovici, D. Sierpowski, M. Steck, U. Spillmann, C. Brandau, E. Förster, Z. Stachura, S. Tashenov, M. Trassinelli, A. Warczak, O. Wehrhan, E. Ziegler, S. Trotsenko, and R. Reuschl. “The FOCAL spectrometer for accurate X-ray spectroscopy of fast heavy ions”. *Nuclear Instruments and Methods in Physics Research Section B: Beam Interactions with Materials and Atoms*, Vol. 245, No. 1, pp. 67 – 71, 2006. Swift Heavy Ions in Matter Proceedings of the Sixth International Symposium on Swift Heavy Ions in Matter (SHIM 2005) Sixth International Symposium on Swift Heavy Ions in Matter.

[Chat07] S. Chatterjee. *Measurement of the Wavelength of the Lyman-*α_1 *Transition of* $^{208}Pb^{81+}$ *Using FOCAL Spectrometers.* PhD thesis, University of Heidelberg, 2007.

[Crea16] Creative Electronic Systems. “Single Board Computers”. `http://www.ces-swap.com/single-board-computers`, 2016.

[Desc75] J. Desclaux. “A multiconfiguration relativistic DIRAC-FOCK program”. *Computer Physics Communications*, Vol. 9, No. 1, pp. 31 – 45, 1975.

[Desl03] R. D. Deslattes, E. G. Kessler, P. Indelicato, L. de Billy, E. Lindroth, and J. Anton. “X-ray transition energies: new approach to a comprehensive evaluation”. *Rev. Mod. Phys.*, Vol. 75, pp. 35–99, Jan 2003.

[Dira28] P. A. M. Dirac. “The Quantum Theory of the Electron”. *Proceedings of the Royal Society of London A*, Vol. 117, No. 778, pp. 610–624, Jan 1928.

[Doli11] A. Dolinskii, K. Knie, C. Dimopoulou, V. Gostishchev, S. Litvinov, F. Nolden, and M. Steck. “Antiproton complex at the FAIR project”. *Nuclear Instruments and Methods in Physics Research Section A: Accelerators, Spectrometers, Detectors and Associated Equipment*, Vol. 629, No. 1, pp. 16 – 24, 2011.

[Drun96] D. Drung and H. Weinstock. *SQUID Sensors: Fundamentals, Fabrication and Application.* Vol. 329, Kluwer, Dordrecht, 1996.

[Dyal89] K. Dyall, I. Grant, C. Johnson, F. Parpia, and E. Plummer. “GRASP: A general-purpose relativistic atomic structure program”. *Computer Physics Communications*, Vol. 55, No. 3, pp. 425 – 456, 1989.

[Dyso49] F. J. Dyson. “The Radiation Theories of Tomonaga, Schwinger, and Feynman”. *Phys. Rev.*, Vol. 75, pp. 486–502, Feb 1949.

[Dyso52] F. J. Dyson. “Divergence of Perturbation Theory in Quantum Electrodynamics”. *Phys. Rev.*, Vol. 85, pp. 631–632, Feb 1952.

[Eich07] J. Eichler and T. Stöhlker. “Radiative electron capture in relativistic ion-atom collisions and the photoelectric effect in hydrogen-like high-Z systems”. *Physics Reports*, Vol. 439, No. 1-2, pp. 1 – 99, 2007.

[Emma10] P. Emma, R. Akre, J. Arthur, R. Bionta, C. Bostedt, J. Bozek, A. Brachmann, P. Bucksbaum, R. Coffee, F.-J. Decker, *et al.* “First lasing and operation of an ångstrom-wavelength free-electron laser”. *nature photonics*, Vol. 4, No. 9, pp. 641–647, 2010.

[Enss00a] C. Enss, A. Fleischmann, K. Horst, J. Schönefeld, J. Sollner, J. Adams, Y. Huang, Y. Kim, and G. Seidel. “Metallic Magnetic Calorimeters for Particle Detection”. *Journal of Low Temperature Physics*, Vol. 121, No. 3-4, pp. 137–176, 2000.

[Enss00b] C. Enss and S. Hunklinger. *Tieftemperaturphysik*. Springer, 2000.

[Enss05] C. Enss, Ed. *Cryogenic Particle Detection*. Vol. 99 of *Topics in Applied Physics*, Springer, 2005.

[Enss16] C. Enss. “Quantum sensors”. `http://www.kip.uni-heidelberg.de/tt-detektoren`, 2016.

[Epp15] S. W. Epp, R. Steinbrügge, S. Bernitt, J. K. Rudolph, C. Beilmann, H. Bekker, A. Müller, O. O. Versolato, H.-C. Wille, H. Yavaş, J. Ullrich, and J. R. Crespo López-Urrutia. “Single-photon excitation of $K\alpha$ in heliumlike Kr^{34+}: Results supporting quantum electrodynamics predictions”. *Phys. Rev. A*, Vol. 92, p. 020502, Aug 2015.

[FAIR01] FAIR. “FAIR Conceptual Design Report”. Tech. Rep., FAIR, 2001.

[FAIR11] FAIR. “Low-energy Storage Ring”. Tech. Rep., FAIR, 2011.

[Fano47] U. Fano. “Ionization Yield of Radiations. II. The Fluctuations of the Number of Ions”. *Phys. Rev.*, Vol. 72, pp. 26–29, Jul 1947.

[Flei05] A. Fleischmann, C. Enss, and G. Seidel. “Metallic Magnetic Calorimeters”. In: C. Enss, Ed., *Cryogenic Particle Detection*, pp. 151–216, Springer Berlin Heidelberg, 2005.

[Fole48] H. M. Foley and P. Kusch. “On the Intrinsic Moment of the Electron”. *Phys. Rev.*, Vol. 73, pp. 412–412, Feb 1948.

[Fran90] B. Franzke *et al.* “Commissioning of the heavy ion storage ring ESR”. *Second European Particle Accelerator Conference*, p. 46, 1990.

[Gass12] T. Gassner. *Messung der Lebensdauer des 2* $^3P_0$ *Zustandes in heliumähnlichem Uran*. Diploma thesis, University of Heidelberg, 2012.

[Gass15] T. Gassner and H. F. Beyer. "Spatial characterization of the internal gas target at the ESR for the FOCAL experiment". *Physica Scripta*, Vol. 2015, No. T166, p. 014052, 2015.

[Gran88] I. Grant and S. Wilson. "Methods in Computational Chemistry". *Relativistic Effects in Atoms and Molecules*, Vol. 2, p. 1, 1988.

[GSI 16] GSI Helmholtz Centre for Heavy Ion Research. "General Program Advisory Committee". `https://www.gsi.de/work/organisation/wissenschaftliche_gremien/pac/g_pac.htm`, 2016.

[Guil20] C. E. Guillaume. *Invar and Elinvar*. Vol. Physics 1901-1921 of *Nobel Lectures*, Elsevier Publishing Company, 1920.

[Gumb05] A. Gumberidze, T. Stöhlker, D. Banaś, K. Beckert, P. Beller, H. F. Beyer, F. Bosch, S. Hagmann, C. Kozhuharov, D. Liesen, F. Nolden, X. Ma, P. H. Mokler, M. Steck, D. Sierpowski, and S. Tashenov. "Quantum Electrodynamics in Strong Electric Fields: The Ground-State Lamb Shift in Hydrogenlike Uranium". *Phys. Rev. Lett.*, Vol. 94, p. 223001, Jun 2005.

[Hann08] D. Hanneke, S. Fogwell, and G. Gabrielse. "New Measurement of the Electron Magnetic Moment and the Fine Structure Constant". *Phys. Rev. Lett.*, Vol. 100, p. 120801, Mar 2008.

[Haus00] M. Hausmann, F. Attallah, K. Beckert, F. Bosch, A. Dolinskiy, H. Eickhoff, M. Falch, B. Franczak, B. Franzke, H. Geissel, T. Kerscher, O. Klepper, H.-J. Kluge, C. Kozhuharov, K. Löbner, G. Münzenberg, F. Nolden, Y. Novikov, T. Radon, H. Schatz, C. Scheidenberger, J. Stadlmann, M. Steck, T. Winkler, and H. Wollnik. "First isochronous mass spectrometry at the experimental storage ring ESR". *Nuclear Instruments and Methods in Physics Research Section A: Accelerators, Spectrometers, Detectors and Associated Equipment*, Vol. 446, No. 3, pp. 569 – 580, 2000.

[Heng15] D. Hengstler, M. Keller, C. Schötz, J. Geist, M. Krantz, S. Kempf, L. Gastaldo, A. Fleischmann, T. Gassner, G. Weber, R. Märtin, T. Stöhlker, and C. Enss. "Towards FAIR: first measurements of metallic magnetic calorimeters for high-resolution x-ray spectroscopy at GSI". *Physica Scripta*, Vol. 2015, No. T166, p. 014054, 2015.

[Henk93] B. Henke, E. Gullikson, and J. Davis. "X-Ray Interactions: Photoabsorption, Scattering, Transmission, and Reflection at E = 50-30,000 eV, Z =

1-92". *Atomic Data and Nuclear Data Tables*, Vol. 54, No. 2, pp. 181 – 342, 1993.

[Herf15] F. Herfurth, Z. Andelkovic, W. Barth, W. Chen, L. A. Dahl, S. Fedotova, P. Gerhard, M. Kaiser, O. K. Kester, H.-J. Kluge, N. Kotovskiy, M. Maier, B. Maaß, D. Neidherr, W. Quint, U. Ratzinger, A. Reiter, A. Schempp, T. Stöhlker, H. Vormann, G. Vorobjev, S. Yaramyshev, and for the HITRAP collaboration. "The HITRAP facility for slow highly charged ions". *Physica Scripta*, Vol. 2015, No. T166, p. 014065, 2015.

[Hild59] G. Hildebrandt. "Gekrümmte Röntgenstrahlen im schwach verformten Kristallgitter A. Laue-Fall der Interferenz". *Zeitschrift für Kristallographie - Crystalline Materials*, Vol. 112, pp. 312–339, 1959.

[Hunt58] L. P. Hunter. "Anomalous Transmission of X-Rays by Single Crystal Germanium". Vol. 61, pp. 214–219, 1958.

[Inst16] Institut für Kernchemie. "Der Mainzer Forschungsreaktor TRIGA Mark II mit Pulseinrichtung". `http://www.kernchemie.uni-mainz.de/234.php`, 2016.

[John85] W. Johnson and G. Soff. "The lamb shift in hydrogen-like atoms, $1 \leq Z \leq 110$". *Atomic Data and Nuclear Data Tables*, Vol. 33, No. 3, pp. 405 – 446, 1985.

[John95] W. Johnson, D. Plante, and J. Sapirstein. "Relativistic Calculations of Transition Amplitudes in the Helium Isoelectronic Sequence". pp. 255 – 329, Academic Press, 1995.

[Kars05] S. G. Karshenboim. "Precision physics of simple atoms: QED tests, nuclear structure and fundamental constants". *Physics Reports*, Vol. 422, No. 1-2, pp. 1 – 63, 2005.

[Kaza14] G. Kazakov, V. Schauer, J. Schwestka, S. Stellmer, J. Sterba, A. Fleischmann, L. Gastaldo, A. Pabinger, C. Enss, and T. Schumm. "Prospects for measuring the 229Th isomer energy using a metallic magnetic microcalorimeter". *Nuclear Instruments and Methods in Physics Research Section A: Accelerators, Spectrometers, Detectors and Associated Equipment*, Vol. 735, pp. 229 – 239, 2014.

[Kell14] M. Keller. *Erster Test eines metallischen magnetischen Kalorimeters am Experimentellen Speicherring ESR der GSI.* Bachelor's thesis, Kirchhoff-Institut für Physik, 2014.

[Kemp14] S. Kempf, M. Wegner, L. Gastaldo, A. Fleischmann, and C. Enss. “Multiplexed Readout of MMC Detector Arrays Using Non-hysteretic rf-SQUIDs”. *Journal of Low Temperature Physics*, Vol. 176, No. 3-4, pp. 426–432, 2014.

[Khne09] M. Kühnel, N. Petridis, D. Winters, U. Popp, R. Dörner, T. Stöhlker, and R. Grisenti. “Low-Z internal target from a cryogenically cooled liquid microjet source”. *Nuclear Instruments and Methods in Physics Research Section A: Accelerators, Spectrometers, Detectors and Associated Equipment*, Vol. 602, No. 2, pp. 311 – 314, 2009.

[Kino14] T. Kinoshita. “Tenth-Order QED Contribution to the Electron g-2 and High Precision Test of Quantum Electrodynamics”. *International Journal of Modern Physics A*, Vol. 29, No. 02, p. 1430003, 2014.

[Klep03] O. Klepper and C. Kozhuharov. “Particle detectors for beam diagnosis and for experiments with stable and radioactive ions in the storage-cooler ring ESR”. *Nuclear Instruments and Methods in Physics Research Section B: Beam Interactions with Materials and Atoms*, Vol. 204, No. 0, pp. 553 – 556, 2003. 14th International Conference on Electromagnetic Isotope Separators and Techniques Related to their Applications.

[Klep92] O. Klepper, F. Bosch, H. Daues, H. Eickhoff, B. Franczak, B. Franzke, H. Geissel, O. Gustafsson, M. Jung, W. Koenig, C. Kozhuharov, A. Magel, G. Münzenberg, H. Stelzer, J. Szerypo, and M. Wagner. “First steps towards radioactive beams in the experimental storage ring at GSI”. *Nuclear Instruments and Methods in Physics Research Section B: Beam Interactions with Materials and Atoms*, Vol. 70, No. 1, pp. 427 – 433, 1992.

[Kraf13] S. Kraft-Bermuth, V. Andrianov, A. Bleile, A. Echler, P. Egelhof, P. Grabitz, C. Kilbourne, O. Kiselev, D. McCammon, and P. Scholz. “Precise Determination of the Lyman-α1 Transition Energy in Hydrogen-like Gold Ions with Microcalorimeters”. *Journal of Low Temperature Physics*, pp. 1–7, 2013.

[Krme01] A. Krämer, A. Kritzer, H. Reich, and T. Stöhlker. “Commissioning of a hydrogen cluster target at the experimental storage ring”. *Nuclear Instruments and Methods in Physics Research Section B: Beam Interactions with Materials and Atoms*, Vol. 174, No. 1-2, pp. 205 – 211, 2001.

[Kusc47] P. Kusch and H. M. Foley. “Precision Measurement of the Ratio of the Atomic ‘g Values’ in the $^2P_{\frac{3}{2}}$ and $^2P_{\frac{1}{2}}$ States of Gallium”. *Phys. Rev.*, Vol. 72, pp. 1256–1257, Dec 1947.

[Lamb47] W. E. Lamb and R. C. Retherford. “Fine Structure of the Hydrogen Atom by a Microwave Method”. *Phys. Rev.*, Vol. 72, pp. 241–243, Aug 1947.

[Laue13] M. Laue. “Eine quantitative Prüfung der Theorie für die Interferenzerscheinungen bei Röntgenstrahlen”. *Annalen der Physik*, Vol. 346, No. 10, pp. 989–1002, 1913.

[Lest12] M. Lestinsky. “CRYRING@ESR: A study group report”. Tech. Rep., FAIR, 2012.

[Lest15] M. Lestinsky, A. Bräuning-Demian, H. Danared, M. Engström, W. Enders, S. Fedotova, B. Franzke, A. Heinz, F. Herfurth, A. Källberg, O. Kester, Y. Litvinov, M. Steck, D. Reistad, A. Simonsson, . Skeppstedt, T. Stöhlker, G. Vorobjev, and for the CRYRING@ESR working group. “CRYRING@ESR: present status and future research”. *Physica Scripta*, Vol. 2015, No. T166, p. 014075, 2015.

[Litv05] Y. Litvinov, H. Geissel, T. Radon, F. Attallah, G. Audi, K. Beckert, F. Bosch, M. Falch, B. Franzke, M. Hausmann, M. Hellström, T. Kerscher, O. Klepper, H.-J. Kluge, C. Kozhuharov, K. Löbner, G. Münzenberg, F. Nolden, Y. Novikov, W. Quint, Z. Patyk, H. Reich, C. Scheidenberger, B. Schlitt, M. Steck, K. Sümmerer, L. Vermeeren, M. Winkler, T. Winkler, and H. Wollnik. “Mass measurement of cooled neutron-deficient bismuth projectile fragments with time-resolved Schottky mass spectrometry at the FRS-ESR facility”. *Nuclear Physics A*, Vol. 756, No. 1-2, pp. 3 – 38, 2005.

[Loch13] M. Lochmann. *Laserspektroskopie der Grundzustands-Hyperfeinstruktur des lithiumähnlichen* $^{209}Bi^{80+}$. PhD thesis, Johannes Gutenberg-Universität Mainz, 2013.

[Loch14] M. Lochmann, R. Jöhren, C. Geppert, Z. Andelkovic, D. Anielski, B. Botermann, M. Bussmann, A. Dax, N. Frömmgen, M. Hammen, V. Hannen, T. Kühl, Y. A. Litvinov, R. López-Coto, T. Stöhlker, R. C. Thompson, J. Vollbrecht, A. Volotka, C. Weinheimer, W. Wen, E. Will, D. Winters, R. Sánchez, and W. Nörtershäuser. “Observation of the hyperfine transition in lithium-like bismuth $^{209}\mathrm{Bi}^{80+}$: Towards a test of QED in strong magnetic fields”. *Phys. Rev. A*, Vol. 90, p. 030501, Sep 2014.

[Lupt94] J. H. Lupton, D. D. Dietrich, C. J. Hailey, R. E. Stewart, and K. P. Ziock. “Measurements of the ground-state Lamb shift and electron-correlation effects in hydrogenlike and heliumlike uranium”. *Phys. Rev. A*, Vol. 50, pp. 2150–2154, Sep 1994.

[Matv13] A. Matveev, C. G. Parthey, K. Predehl, J. Alnis, A. Beyer, R. Holzwarth, T. Udem, T. Wilken, N. Kolachevsky, M. Abgrall, D. Rovera, C. Salomon,

P. Laurent, G. Grosche, O. Terra, T. Legero, H. Schnatz, S. Weyers, B. Altschul, and T. W. Hänsch. “Precision Measurement of the Hydrogen 1S-2S Frequency via a 920-km Fiber Link”. *Phys. Rev. Lett.*, Vol. 110, p. 230801, Jun 2013.

[Mohr16] P. J. Mohr, B. N. Taylor, and D. B. Newell. “CODATA Recommended Values of the Fundamental Physical Constants”. `http://physics.nist.gov/cuu/Constants/index.html`, 2016.

[Mohr98] P. J. Mohr, G. Plunien, and G. Soff. “QED corrections in heavy atoms”. *Physics Reports*, Vol. 293, No. 5-6, pp. 227 – 369, 1998.

[Naka13] Y. Nakano, Y. Takano, T. Ikeda, Y. Kanai, S. Suda, T. Azuma, H. Bräuning, A. Bräuning-Demian, D. Dauvergne, T. Stöhlker, and Y. Yamazaki. “Resonant coherent excitation of the lithiumlike uranium ion: A scheme for heavy-ion spectroscopy”. *Phys. Rev. A*, Vol. 87, p. 060501, Jun 2013.

[Nefi96] A. V. Nefiodov, L. N. Labzowsky, G. Plunien, and G. Soff. “Nuclear polarization effects in spectra of multicharged ions”. *Physics Letters A*, Vol. 222, No. 4, pp. 227 – 232, 1996.

[Nold11] F. Nolden, P. Hülsmann, Y. Litvinov, P. Moritz, C. Peschke, P. Petri, M. Sanjari, M. Steck, H. Weick, J. Wu, Y. Zang, S. Zhang, and T. Zhao. “A fast and sensitive resonant Schottky pick-up for heavy ion storage rings”. *Nuclear Instruments and Methods in Physics Research Section A: Accelerators, Spectrometers, Detectors and Associated Equipment*, Vol. 659, No. 1, pp. 69 – 77, 2011.

[Nrte15] W. Nörtershäuser. “private communication”. 2015.

[Omet06] C. Omet, P. Spiller, J. Stadlmann, and D. H. H. Hoffmann. “Charge change-induced beam losses under dynamic vacuum conditions in ring accelerators”. *New Journal of Physics*, Vol. 8, No. 11, p. 284, 2006.

[Penn61] P. Penning and D. Polder. “Anomalous transmission of x-rays in elastically deformed crystals”. *Philips Res. Repts.*, Vol. 16, pp. 419 – 440, 1961.

[Petr14] N. Petridis. *The Internal Multiphase Target for Storage Ring Experiments*. PhD thesis, Johann Wolfgang Goethe-Universität in Frankfurt am Main, 2014.

[Phil98] W. Phillips. “Nobel Lecture: Laser cooling and trapping of neutral atoms”. *Rev. Mod. Phys.*, Vol. 70, pp. 721–741, Jul 1998.

[Pies12a] C. Pies, S. Schäfer, S. Heuser, S. Kempf, A. Pabinger, J.-P. Porst, P. Ranitsch, N. Foerster, D. Hengstler, A. Kampkötter, T. Wolf, L. Gastaldo,

A. Fleischmann, and C. Enss. “maXs: Microcalorimeter Arrays for High-Resolution X-Ray Spectroscopy at GSI/FAIR”. *Journal of Low Temperature Physics*, Vol. 167, No. 3-4, pp. 269–279, 2012.

[Pies12b] C. Pies. *maXs-200: Entwicklung und Charakterisierung eines Röntgendetektors basierend auf magnetischen Kalorimetern für die hochauflösende Spektroskopie hochgeladener Ionen*. PhD thesis, University of Heidelberg, 2012.

[Plun95] G. Plunien and G. Soff. “Nuclear-polarization contribution to the Lamb shift in actinide nuclei”. *Phys. Rev. A*, Vol. 51, pp. 1119–1131, Feb 1995.

[Prot05] D. Protic, T. Stöhlker, T. Krings, I. Mohos, and U. Spillmann. “Two-dimensional microstrip Germanium detector for the spectroscopy of hard X-ray transitions”. *IEEE Trans. Nucl. Sci.*, Vol. 52, p. 3194, 2005.

[Rei15] P. Reiß, P. Schmidt, C. Ozga, A. Knie, and A. Ehresmann. “Dispersed fluorescence spectrometry from the VIS to VUV spectral range for experiments at heavy-ion storage facilities”. *Physica Scripta*, Vol. 2015, No. T166, p. 014031, 2015.

[Reus06] R. Reuschl, A. Gumberidze, T. Stöhlker, C. Kozhuharov, J. Rzadkiewicz, U. Spillmann, S. Tashenov, S. Fritzsche, and A. Surzhykov. “The Balmer spectrum of H-like uranium produced by radiative recombination at low velocities”. *Radiation Physics and Chemistry*, Vol. 75, No. 11, pp. 1740 – 1743, 2006. Proceedings of the 20th International Conference on X-ray and Inner-Shell Processes4-8 July 2005, Melbourne, AustraliaProceedings of the 20th International Conference on X-ray and Inner-Shell Processes.

[Reus13] R. Reuschl, T. Gassner, U. Spillmann, A. Bräuning-Demian, A. Ananyeva, H. Beyer, K.-H. Blumenhagen, W. Chen, S. Hagmann, M. Hegewald, P. Indelicato, M. Schwemlein, S. Toleikis, M. Trassinelli, S. Trotsenko, D. Winters, N. Winters, and T. Stöhlker. “Lifetime measurement of the $2\,{}^3\mathrm{P}_0$ state in He-like uranium”. *Physica Scripta*, Vol. 2013, No. T156, p. 014024, 2013.

[Rio11] M. Sanchez del Rio and R. J. Dejus. “XOP v2.4: recent developments of the x-ray optics software toolkit”. *Proc. SPIE*, Vol. 8141, pp. 814115–814115–5, 2011.

[Rio15] M. Sanchez del Rio, N. Perez-Bocanegra, X. Shi, V. Honkimäki, and L. Zhang. “Simulation of X-ray diffraction profiles for bent anisotropic crystals”. *Journal of Applied Crystallography*, Vol. 48, No. 2, pp. 477–491, Apr 2015.

[Rio97] M. Sanchez del Rio, C. Ferrero, and V. Mocella. “Computer simulation of bent perfect crystal diffraction profiles”. *Proc. SPIE*, Vol. 3151, pp. 312–323, 1997.

[Roze96] J. Rozet, C. Stéphan, and D. Vernhet. “ETACHA: a program for calculating charge states at GANIL energies”. *Nuclear Instruments and Methods in Physics Research Section B: Beam Interactions with Materials and Atoms*, Vol. 107, No. 1-4, pp. 67 – 70, 1996.

[Sche98] C. Scheidenberger, T. Stöhlker, W. Meyerhof, H. Geissel, P. Mokler, and B. Blank. “Charge states of relativistic heavy ions in matter”. *Nuclear Instruments and Methods in Physics Research B*, Vol. 142, No. 4, pp. 441 – 462, 1998.

[Schr26] E. Schrödinger. “Quantisierung als Eigenwertproblem”. *Annalen der Physik*, Vol. 386, No. 18, pp. 109–139, 1926.

[Spil06] P. Spiller and G. Franchetti. “The FAIR accelerator project at GSI”. *Nuclear Instruments and Methods in Physics Research Section A: Accelerators, Spectrometers, Detectors and Associated Equipment*, Vol. 561, No. 2, pp. 305 – 309, 2006. Proceedings of the Workshop on High Intensity Beam Dynamics COULOMB 2005 Workshop on High Intensity Beam Dynamics.

[Spil09] U. Spillmann. *Charakterisierung und erster experimenteller Einsatz von ortsauflösenden, energiedispersiven Germanium-Detektoren zur Präzisionsspektroskopie an schweren Ionen.* PhD thesis, GSI Darmstadt, Johann Wolfgang Goethe-Universität in Frankfurt am Main, Mar 2009.

[Sthl15a] T. Stöhlker, V. Bagnoud, K. Blaum, A. Blazevic, A. Bräuning-Demian, M. Durante, F. Herfurth, M. Lestinsky, Y. Litvinov, S. Neff, R. Pleskac, R. Schuch, S. Schippers, D. Severin, A. Tauschwitz, C. Trautmann, D. Varentsov, and E. Widmann. “APPA at FAIR: From fundamental to applied research”. *Nuclear Instruments and Methods in Physics Research Section B: Beam Interactions with Materials and Atoms*, Vol. 365, Part B, pp. 680 – 685, 2015. Swift Heavy Ions in Matter, 18 - 21 May, 2015, Darmstadt, Germany.

[Sthl15b] T. Stöhlker, Y. A. Litvinov, and for the SPARC Collaboration. “Atomic physics experiments at the high energy storage ring”. *Physica Scripta*, Vol. 2015, No. T166, p. 014025, 2015.

[Stoh00] T. Stöhlker, P. H. Mokler, F. Bosch, R. W. Dunford, F. Franzke, O. Klepper, C. Kozhuharov, T. Ludziejewski, F. Nolden, H. Reich, P. Rymuza,

Z. Stachura, M. Steck, P. Swiat, and A. Warczak. “1s Lamb Shift in Hydrogenlike Uranium Measured on Cooled, Decelerated Ion Beams”. *Phys. Rev. Lett.*, Vol. 85, pp. 3109–3112, Oct 2000.

[Stoh16] T. Stöhlker. “private communication”. 2016.

[Stoh93] T. Stöhlker, P. H. Mokler, K. Beckert, F. Bosch, H. Eickhoff, B. Franzke, M. Jung, Y. Kandler, O. Klepper, C. Kozhuharov, R. Moshammer, F. Nolden, H. Reich, P. Rymuza, P. Spädtke, and M. Steck. “Ground-state Lamb shift for hydrogenlike uranium measured at the ESR storage ring”. *Phys. Rev. Lett.*, Vol. 71, pp. 2184–2187, Oct 1993.

[Stoh97] T. Stöhlker, F. Bosch, A. Gallus, C. Kozhuharov, G. Menzel, P. H. Mokler, H. T. Prinz, J. Eichler, A. Ichihara, T. Shirai, R. W. Dunford, T. Ludziejewski, P. Rymuza, Z. Stachura, P. Swiat, and A. Warczak. “Strong Alignment Observed for the Time-Reversed Photoionization Process Studied in Relativistic Collisions with Bare Uranium Ions”. *Phys. Rev. Lett.*, Vol. 79, pp. 3270–3273, Oct 1997.

[Stur14] S. Sturm, F. Köhler, J. Zatorski, A. Wagner, Z. Harman, G. Werth, W. Quint, C. Keitel, and K. Blaum. “High-precision measurement of the atomic mass of the electron”. *Nature*, Vol. 506, p. 467, Feb 2014.

[Thoe16] M. Thoennessen. “Discovery of Nuclides Project”. `https://people.nscl.msu.edu/~thoennes/isotopes`, 2016.

[Tras15] M. Trassinelli. “private communication”. 2015.

[Uehl35] E. A. Uehling. “Polarization Effects in the Positron Theory”. *Phys. Rev.*, Vol. 48, pp. 55–63, Jul 1935.

[Uhle26] G. Uhlenbeck and S. Goudsmit. “Spinning Electrons and the Structure of Spectra”. *Nature*, Vol. 117, pp. 264–265, 1926.

[Ullm15] J. Ullmann, Z. Andelkovic, A. Dax, W. Geithner, C. Geppert, C. Gorges, M. Hammen, V. Hannen, S. Kaufmann, K. König, Y. Litvinov, M. Lochmann, B. Maass, J. Meisner, T. Murböck, R. Sánchez, M. Schmidt, S. Schmidt, M. Steck, T. Stöhlker, R. C. Thompson, J. Vollbrecht, C. Weinheimer, and W. Nörtershäuser. “An improved value for the hyperfine splitting of hydrogen-like 209 Bi 82+”. *Journal of Physics B: Atomic, Molecular and Optical Physics*, Vol. 48, No. 14, p. 144022, 2015.

[Waas95] D. Waasmaier and A. Kirfel. “New analytical scattering-factor functions for free atoms and ions”. *Acta Crystallographica Section A*, Vol. 51, No. 3, pp. 416–431, May 1995.

[Wang12] M. Wang, G. Audi, A. Wapstra, F. Kondev, M. MacCormick, X. Xu, and B. Pfeiffer. “The Ame2012 atomic mass evaluation”. *Chinese Physics C*, Vol. 36, No. 12, p. 1603, 2012.

[Wich56] E. H. Wichmann and N. M. Kroll. “Vacuum Polarization in a Strong Coulomb Field”. *Phys. Rev.*, Vol. 101, pp. 843–859, Jan 1956.

[Wint15] D. Winters, T. Beck, G. Birkl, C. Dimopoulou, V. Hannen, T. Kühl, M. Lochmann, M. Loeser, X. Ma, F. Nolden, W. Nörtershäuser, B. Rein, R. Sánchez, U. Schramm, M. Siebold, P. Spiller, M. Steck, T. Stöhlker, J. Ullmann, T. Walther, W. Wen, J. Yang, D. Zhang, and M. Bussmann. “Laser cooling of relativistic heavy-ion beams for FAIR”. *Physica Scripta*, Vol. 2015, No. T166, p. 014048, 2015.

[Yero15] V. A. Yerokhin and V. M. Shabaev. “Lamb Shift of n = 1 and n = 2 States of Hydrogen-like Atoms, $1 \leq Z \leq 110$”. *Journal of Physical and Chemical Reference Data*, Vol. 44, No. 3, p. 033103, 2015.

[Youn02] T. Young. “The Bakerian Lecture: On the Theory of Light and Colours”. *Philosophical Transactions of the Royal Society of London*, Vol. 92, pp. 12–48, 1802.

[Zach67] W. Zachariasen. *Theory of X-ray Diffration in Crystals*. New York: Dover, 1967.

Curriculum Vitæ

Persönliche Angaben

	Tobias Gaßner
Geburtsdatum	**14. Mai 1986 in Bruchsal**

Ausbildung

1992-1996	**Grundschule**, *Grund- und Hauptschule Kronau.*
1996-1999	**Hauptschule**, *Grund- und Hauptschule Kronau.*
1999-2001	**Hauptschule**, *Michael-Ende-Schule Bad Schönborn.*
2001	**Hauptschulabschluss**, *Michael-Ende-Schule Bad Schönborn.*
2001-2003	**Berufsfachschule Fachrichtung Elektrotechnik**, *Balthasar Neumann Schule 1 Bruchsal.*
2003	**Realschulabschluss**, *Balthasar Neumann Schule 1 Bruchsal.*
2003-2006	**Technisches Gymnasium**, *Balthasar Neumann Schule 1 Bruchsal.*
2006	**Abitur**, *Balthasar Neumann Schule 1 Bruchsal.*
09/2006-09/2012	**Physikstudium**, *Schwerpunkt Atomphysik*, Ruprecht-Karls-Universität Heidelberg.
09/2011-09/2012	**Diplomarbeit**, *»Messung der Lebensdauer des* $2\,^3P_0$ *Zustandes in heliumähnlichem Uran«*, GSI Helmholtzzentrum für Schwerionenforschung Darmstadt.
2012	**Diplom**, *Ruprecht-Karls-Universität Heidelberg.*
09/2012-06/2016	**Promotion**, *»High Precision X-Ray Spectroscopy of Highly Charged Heavy Ions«*, Friedrich-Schiller-Universität Jena, Helmholtz-Institut Jena.

Darmstadt, den 23. Juni 2016

Tobias Gaßner

Ehrenwörtliche Erklärung

Ich erkläre hiermit ehrenwörtlich, dass ich die vorliegende Arbeit selbständig, ohne unzulässige Hilfe Dritter und ohne Benutzung anderer als der angegebenen Hilfsmittel und Literatur angefertigt habe. Die aus anderen Quellen direkt oder indirekt übernommenen Daten und Konzepte sind unter Angabe der Quelle gekennzeichnet.

Bei der Auswahl und Auswertung folgenden Materials haben mir die nachstehend aufgeführten Personen in der jeweils beschriebenen Weise entgeltlich/unentgeltlich geholfen:

1. Dr. Heinrich F. Beyer vom GSI Helmholtzzentrum für Schwerionenforschung in Darmstadt ist als Leiter des FOCAL Experiments für dessen Entwicklung zuständig. Die Analyse der Messdaten wurde in Abstimmung mit Herrn Dr. Beyer durchgeführt. Die numerischen Parameter in Tabelle 5.4 wurden von Herrn Dr. Beyer zur Verfügung gestellt. All dies geschah unentgeltlich.

2. Dr. Martino Trassinelli vom Institut des NanoSciences de Paris in Frankreich stellte die Elektroneneinfangquerschnitte, die in Unterkapitel 5.2.5 verwendet wurden, zur Verfügung. Weiterhin berechnete Herr Dr. Trassinelli die Bindungsenergien in Tabelle 2.2 für die Zustände $n = 3$. Es wurden zahlreiche Diskussionen geführt, um eine optimale Strategie zur Datenanalyse zu entwickeln. All dies geschah unentgeltlich.

Weitere Personen waren an der inhaltlich-materiellen Erstellung der vorliegenden Arbeit nicht beteiligt. Insbesondere habe ich hierfür nicht die entgeltliche Hilfe von Vermittlungs- bzw. Beratungsdiensten (Promotionsberater oder andere Personen) in Anspruch genommen. Niemand hat von mir unmittelbar oder mittelbar geldwerte Leistungen für Arbeiten erhalten, die im Zusammenhang mit dem Inhalt der vorgelegten Dissertation stehen.

Die Arbeit wurde bisher weder im In- noch im Ausland in gleicher oder ähnlicher Form einer anderen Prüfungsbehörde vorgelegt.

Die geltende Promotionsordnung der Physikalisch-Astronomischen Fakultät ist mir bekannt.

Ich versichere ehrenwörtlich, dass ich nach bestem Wissen die reine Wahrheit gesagt und nichts verschwiegen habe.

Darmstadt, den 23. Juni 2016

Tobias Gaßner

Danksagung

In den vergangenen Jahren habe ich viel Unterstützung durch meine Kolleginnen, Kollegen und Freunde erfahren. Hiermit möchte ich allen, die mich unterstützt haben, recht herzlich danken.

Als erstes möchte ich meinem Betreuer Prof. Dr. Thomas Stöhlker danken, der mir die Möglichkeit bot, viele interessante Experimente mit den modernsten Detektorsystemen durchzuführen. Durch seine Ermutigung zur Teilnahme an zahlreichen internationalen Konferenzen habe ich viel lernen können. Bei unzähligen Diskussionen konnte er mir wichtige Anregungen geben, die mir zu einem besseren Verständnis der grundlegendsten physikalischen Prozesse verholfen haben.

Dr. Heinrich F. Beyer möchte ich dafür danken, dass er mich am FOCAL Experiment teilnehmen lies und mir wichtige Aufgaben vorbehaltlos anvertraute. Auf seine Expertise konnte ich mich stets verlassen.

Dr. Renate Märtin, Dr. Günter Weber und Prof. Dr. Christian Spielmann möchte ich dafür danken, dass sie mich in der Research School of Advanced Photon Science aufgenommen haben und mich mit der Betreuung des maXs Mikrokalorimeters bedacht haben.

Der Quantensensorengruppe um Prof. Dr. Christian Enss, insbesondere den Herren Dr. Andreas Fleischmann und Dipl. Phys. Daniel Hengstler, möchte ich für die ausgezeichnete Zusammenarbeit während den Strahlzeiten danken.

Dr. Martino Trassinelli möchte ich für die freundschaftlichen Korrespondenzen und seine unermüdlichen Mühen im Zuge der Auswertung der FOCAL Daten danken.

Dr. Gerhard Burau und Dr. Sascha Vogel möchte ich für ihren vorbildlichen Einsatz für die Helmholtz Graduate School for Hadron and Ion Research (HGS-HIRe) danken.

Weiterhin möchte ich Dr. Regina Heß, Dr. Natalya Winters und Dr. Danyal Winters für ihre Freundschaft und für das Korrekturlesen meiner Arbeit danken.

Dr. Uwe Spillmann gehört mein Dank, da er viele Mühen in das FOCAL Experiment investiert hat und auch bei Experimenten außerhalb der GSI vollsten Einsatz gezeigt hat.

Meinen guten Freunden Dipl. Ing. Andre Wagner und Dipl. Phys. Marco Wiesel danke ich für das Korrekturlesen meiner Arbeit, sowie dafür, dass sie stets für mich da sind.

Dr. Manuel Vogel danke ich ebenfalls für das Korrekturlesen der Arbeit und für seine Gesellschaft bei zahlreichen Konferenzen.

Meinen Kolleginnen und Kollegen Nina Bauer, Dipl. Phys. Karl-Heinz Blumenhagen, Prof. Dr. Fritz Bosch, Dr. Carsten Brandau, Wolfgang Enders, Dr. Oliver Forstner, Dr. Alexandre Gumberidze, Prof. Dr. Siegbert Hagmann, Dr. Pierre-Michel Hillenbrand, Dr. Christophor Kozhuharov, Dr. Michael Lestinsky, Dr. Yuri Litvinov, Dr. Tatiana Litvinova, Stefanie Lüttges, Dr. Nikos Petridis, Davide Racano, Msc Daniel Schury, Prof. Dr. Andrey Surzhykov und Dr. Sergiy Trotsenko danke ich für die vielen Gespräche und das angenehme Arbeitsumfeld, das ich an der GSI erfahren durfte.

Mein besonderer Dank gilt meinen Eltern Birgit und Theo, meinem Bruder Steffen, sowie meiner Freundin Sandra, die mich stets unterstützen und in jeder Lebenslage für mich da sind.

Abbildung 7.2: Die Kolleginnen und Kollegen der Abteilung Atomphysik